

# In Situ Scanning Tunneling Microscopy and Microcantilever Investigations of yeast cytochrome c on gold

**Hansen, Allan Glargaard**

*Publication date:*
2003

*Document Version*
Publisher's PDF, also known as Version of record

# *In Situ* Scanning Tunneling Microscopy and Microcantilever Investigations of yeast cytochrome *c* on gold

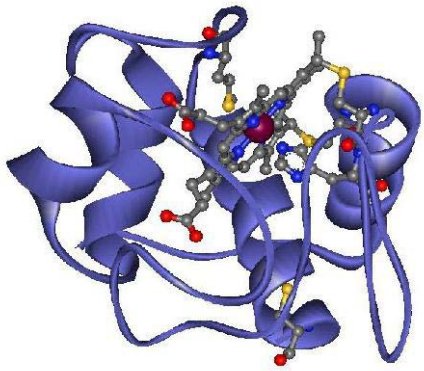

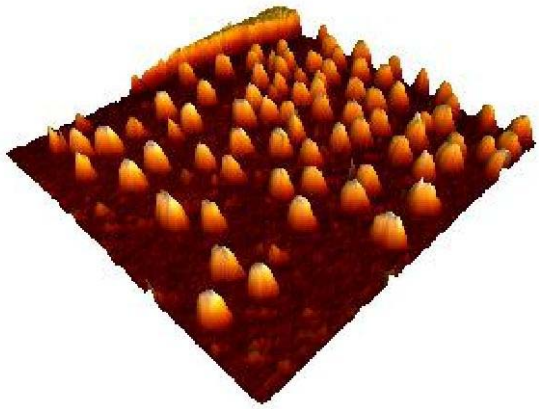

Allan Glargaard Hansen

Department of Chemistry
Technical University of Denmark
2002

# *In Situ* Scanning Tunneling Microscopy and Microcantilever Investigations of yeast cytochrome *c* on gold

In partial fulfilment of the requirements for the degree of Ph.D.

Allan Glargaard Hansen

Ph.D. # 99-0141-323
Department of Chemistry
Technical University of Denmark

The front page picture shows: (Top) the structure of *Saccharomyces Cerevisiae* yeast cytochrome *c* (YCC). (Bottom) *In situ* STM image of YCC molecules on gold. The structure in the background is a gold step.

# Preface

The work described in this report has been carried out at the Technical University of Denmark (DTU) in the Bioinorganic Group at Department of Chemistry under the supervision of Prof. Jens Ulstrup (main supervisor) and in the Bioprobe Group at the Microelectronics Center (MIC), DTU under the supervision of Project Leader Anja Boisen during the period from September 1999 to November 2002. The project has been financed by a grant from Statens Teknisk Videnskabelige Forskningsråd. I would like to thank first my two supervisors, Jens Ulstrup and Anja Boisen for their support, valuable suggestions and inspiring discussions. I am grateful to Anja and the rest of MIC for the introduction into the world of microcantilevers, micro-and nanotechnology, and clean room techniques. I also value highly the opportunity to work with a state-of-the-art STM in the Bioinorganic Group.

I am grateful to Associate Prof. Jingdong Zhang for generously sharing her STM and electrochemistry experience with me. I also acknowledge the help of Assistant Professor Hainer Wackerbarth for many discussions about our favorite molecule: cytochrome *c*. Thanks go to Lab. Technicians Lise-Lotte Jespersen and Agnieszka Ingvorsen for HPLC purification of protein samples and to Associate Prof. Hans-Erik Mølager Christensen for clearing their work schedule to help me, to Ph.D. Jens Ulrik Nielsen for valuable suggestions and clear insight, and to Associate Prof. Jens Andersen for advice regarding STM tip technology.

At MIC I will also thank Ph.D. Jacob Thaysen and Ph.D. student Peter Rasmussen for providing me with 'hardware' (microcantilever chips), Ph.D. Henriette Jensenius for many discussions on experimental issues, M. Sc. Michael Wrang Mortensen for AFM images, and M.Sc. students Loay Mettan, Alicia Johansson, and Peter Rygaard Lassen for microcantilever measurements. I am grateful to all members of Bioinorganic Group and Bioprobe Project for their interest and company during the last three years.

A special thanks goes to Prof. Ib Chorkendorff, Interdisciplinary Research Center for Catalysis (ICAT), DTU for the opportunity to perform XPS measurements and to Engineer Assistant John Larsen at Department of Physics, DTU for his great help with the measurements.

# Abstract

Proteins immobilized at surfaces are a research field of fundamental interest with important applications in bio- and nanotechnology, such as biosensors, biomimetics materials, and supramolecular structures. Knowledge of structure and functionality of protein layers is thus essential. In this report a comprehensive approach is used to assess such properties of *Saccharomyces Cerevisiae* yeast cytochrome *c* (YCC) on gold surfaces, both macroscopically and at the single-molecule level.

The gold-sulfur interaction was used to detect YCC with microcantilevers. YCC contains a near-surface cysteine (Cys102) usable for immobilization to gold. Gas phase adsorption of 1-hexanethiol on gold-coated microcantilevers was first investigated to optimize surface cleaning for applications in liquid. Cleaning by Aqua Regia (AR) and Oxygen Plasma (OP) was tested. AR provided a faster and larger surface stress signal than OP. 0.7 N/m of compressive stress was observed, while OP gave 0.25 N/m compressive stress. The signal for AR cleaned microcantilevers deteriorated, however, with successive cleanings, while the signal from OP cleaned cantilevers was stable. OP cleaning was hence used for detection of YCC by gold-coated microcantilevers in buffer solution. 0.3 N/m of tensile stress evolved upon introduction of YCC into the microcantilever cell. The signal increased to 0.6 N/m when YCC physisorbed on the silicon nitride reference cantilever was flushed off with buffer. The rate of surface stress change increased with increasing concentration of YCC in the range 5-100 μM. A range of other sulfur-containing molecules were investigated to elucidate further adsorption properties of both the gold-coated working cantilever and the reference cantilever. Cysteine gave tensile stress (0.2-0.3 N/m) when introduced to OP cleaned microcantilevers. The stress signal could be returned to zero when the microcantilever cell was flushed, indicating physisorbed cysteine. Compressive stress (0.2-0.4 N/m) evolved, however, when cysteine was adsorbed on microcantilevers cleaned in Argon plasma (AP) and a fresh gold layer (FG) was deposited on the working cantilever before measurement. The cysteine layer was stable towards flushing with buffer, indicating chemisorbed cysteine. Adsorption of 1-octadecanethiol onto AP cleaned microcantilevers with FG from a dilute solution in an ethanol/water mixture provided a tensile stress of –0.16 N/m possibly due to interaction with the reference cantilever or the mixed solvent. Adsorption of 6-mercaptohexanol (MCH) onto AP cleaned microcanilevers with FG caused a fast concentration-independent tensile surface stress signal of –0.7 N/m followed by a

slow compressive signal. The first signal resembled electrostatic binding to the reference cantilever. The second signal presumably adsorption to the gold layer.

YCC was imaged on Au(111) by *in situ* STM with molecular resolution, showing globular structures with average area 13-22 $nm^2$. This is slightly larger than expected from the bulk size of YCC, presumably due to tip convolution. Coverages were up to 18 % or $8 \times 10^{11}$ molecules·$cm^{-2}$. Prolonged adsorption increased the molecular density to $18 \times 10^{11}$ molecules·$cm^{-2}$, but STM contrast was attenuated. The YCC molecular layer was stable in the potential range $-0.4 \rightarrow -0.1$ V vs. SCE. The contrast of YCC did not vary with potential in this range. The layers were, however, unstable towards potential scanning while imaging, with significant desorption within minutes.

Capacitance (CAP) measurements, Linear Sweep (LSV), and Differential Pulse Voltammetry (DPV) were conducted for YCC at Au(111). The capacitance of the YCC coated electrode was 9 $\mu Fcm^{-2}$, confirming that the electrode surface was covered with material (YCC) of low dielectric constant. A reductive desorption signal at app. -0.76 V indicated that YCC is bound to gold via sulfur. The charge transferred was 10 $\mu Ccm^{-2}$. The charge of a full monolayer desorbing via one gold-sulfur bond corresponds to 1.5 $\mu Ccm^{-2}$. The excess charge might result from capacitive currents or binding of YCC via other sulfur residues than Cys102. YCC contains five sulfur atoms. Besides a weak DPV signal at 0.01 V from native YCC, DPV and CAP showed a peak at -0.45 V corresponding to a non-native conformation of YCC where the heme axial ligation to Met80 is lost.

X-ray Photoelectron Spectroscopy (XPS) showed peaks at 162.2 and 163.4 eV for both YCC and Horse heart cytochrome *c* (HHCC), which does not contain cysteine at position 102. Binding energies of 162.2 and 163.3 eV are fingerprints of gold-thiolate bonds. The HHCC spectrum contained a minor peak at 164.8 eV and the spectrum of YCC minor peaks at 161.2 and 164.6 eV. Hence the sulfur peak is broader for YCC than for HHCC. Gold-thiolate peaks for HHCC could be explained by unfolding and exposure of internal sulfur residues induced by the UHV environment. YCC is structurally less stable than HHCC. The broader sulfur peak for YCC could therefore be explained by a more unfolded structure than HHCC. The Au photoelectron signal was lower for YCC, indicating a higher coverage of YCC than HHCC.

Broad characterization of YCC layers on gold with regards to adsorption kinetics, functionality, structure, and binding mode has thus been performed. YCC was found to be bonded to gold via sulfur and to exist partially in a non-native but functionable state.

# Resumé (Abstract in Danish)

Overfladeimmobiliserede proteiner er et vigtigt forskningsområde af fundamental interesse med vigtige anvendelser indenfor bio- og nanoteknologi, som biosensorer, biomimetiske materialer og supramolekylære strukturer. Viden om proteinlags struktur og funktion er derfor essentiel. En flerfoldig indgangsvinkel er benyttet til at evaluere sådanne egenskaber for *Saccharomyces Cerevisiae* gær cytochrom *c* (YCC) på guldoverflader, både makroskopisk og på enkeltmolekyle-niveau.

Affiniteten mellem guld og svovl blev benyttet til detektion af YCC med microcantilevers. YCC har en overfladenær cystein (Cys102) anvendelig for immobilisering på guld, Gasfaseadsorption af 1-hexanthiol på guldfunktionaliserede microcantilevers studeredes først for at optimere overfladebehandlingen mhp. anvendelser i væske. Behandling med Aqua Regia (AR) og Oxygen Plasma (OP) afprøvedes. AR gav et hurtigere og større overfladestresssignal end OP. 0.7 N/m kompressivt stress observeredes for AR mod 0.25 N/m for OP. Signalet for AR forværredes dog ved gentagne behandlinger, mens signalet for OP behandlede cantilevers var stabilt. OP-behandling benyttedes derfor til detektion af YCC med guldfunktionaliserede microcantilevers i buffer-opløsning. Tilsætning af YCC til microcantilevercellen udløste 0.3 N/m tensilt stress. Signalet øgedes til 0.6 N/m, når YCC physisorberet på siliciumnitrid-referencecantileveren skylledes af med buffer. Signalets hastighed øgedes med stigende YCC-koncentration i intervallet 5-100 μM. En række andre molekyler indeholdende svovl undersøgtes for yderligere at opklare adsorptions-mønstrene på både den guldfunktionaliserede målecantilever og referencecantileveren. Cystein udløste tensilt stress (0.2-0.3 N/m) på OP-behandlede microcantilevers. Stresssignalet kunne bringes til 0 ved skylning af cellen, hvilket indikerer at cystein er physisorberet. Cystein adsorberet på Argon plasma-behandlede (AP) microcantilevers med et frisk guldlag (FG) deponeret på målecantileveren gav derimod kompressivt stress (0.2-0.4 N/m). Det chemisorberede cysteinlag kunne ikke skylles af med buffer. Adsorption af 1-octadecanthiol fra en fortyndet opløsning i en alkohol/vand-blanding på AP-behandlede microcantilevers med FG udløste tensilt stress (-0.16 N/m) muligvis pga. adsorption på referencecantileveren eller alkohol/vand-blandingen. Adsorption af 6-mercaptohexanol (MCH) på AP-behandlede microcantilevers med FG gav et hurtigt koncentrations-uafhængigt tensilt overfladestress-signal (-0.7 N/m) efterfulgt af et langsomt kompressivt signal. Det første signal lignede elektrostatisk binding til referencecantileveren. Det andet signal kunne skyldes adsorption på guldlaget.

In situ STM af YCC på Au(111) med molekylær opløsning udviste globulære strukturer med et gennemsnitligt areal på 13-22 $nm^2$. Dette er en anelse større end forventet udfra YCC's struktur i opløsning, sandsynligvis pga. tipkonvolutering. Overfladekoncentrationer var max. 18 % eller $8 \times 10^{11}$ molekyler·$cm^{-2}$. Forlænget adsorption forøgede koncentrationen til $18 \times 10^{11}$ molekyler·$cm^{-2}$, men STM-kontrasten formindskedes. YCC-lagene var stabile i potentialintervallet $-0.4 \rightarrow -0.1$ V (SCE). YCC-kontrasten var uafhængig af potentialet i dette intervallet. Lagene var dog ustabile overfor potentialændringer under skanning med betydelig desorption indenfor minutter.

Kapacitansmålinger, Linear Sweep (LSV) og Differential Pulse Votammetry (DPV) udførtes for YCC på Au(111). En kapacitans på 9 $\mu Fcm^{-2}$ af den YCC-adsorberede Au(111)-elektrode bekræftede, at elektrodeoverfladen var dækket af materiale (YCC) med lav dielektricitetskonstant. Et signal fra reduktiv desorption ved ca. –0.76 V indikerer at YCC er bundet til guld via svovl. Den overførte ladning var 10 $\mu Ccm^{-2}$. Et YCC-monolag bundet med én guld-svovl-binding svarer til 1.5 $\mu Ccm^{-2}$. Den overskydende ladning kunne stamme fra kapacitive strømme eller binding af YCC med andre svovlgrupper end Cys102. YCC har fem svovlatomer. Foruden et svagt DPV-signal ved 0.01 V fra nativt YCC fremviste DPV og CAP et signal ved –0.45 V fra en ikke-nativ konformation af YCC, hvor hæms aksiale ligering til Met80 er brudt.

X-ray Photoelectron Spectroscopy (XPS) udviste signaler ved 162.2 og 163.4 eV for både YCC og hestehjerte cytochrom *c* (HHCC) som ikke har cystein i position 102. Bindingsenergierne 162.2 og 163.3 er karakteristiske for guld-thiolat-bindingen. HHCC-spektret havde et mindre signal ved 164.8 eV og YCC-spektret havde mindre signaler ved 161.2 og 164.6 eV. Svovlsignalet er altså bredere for YCC end for HHCC. HHCC's guld-thiolat-binding kunne forklares med udfoldning og eksponering af interne svovlgrupper fremkaldt af UHV-miljøet. YCC er strukturelt mindre stabil end HHCC. YCC's bredere svovlsignal kunne derfor forklares af en mere udfoldet struktur end HHCC. Fotoelektronsignalet fra Au var lavere for YCC, hvilket antyder en højere overfladekoncentration af YCC end for HHCC.

En omfattende karakterisering af YCC-monolag på guld mht. adsorptionkinetik, funktionalitet, struktur og binding er gennemført. Det blev fundet at YCC bandt til guld via svovl og eksisterede delvist i en ikke-nativ, men funktionel konformation.

# 1 INTRODUCTION

Monolayers of functional biological molecules and macromolecules such as amino acids [Giz,99; Sawaguchi,01], oligonucleotide strands [Service,98; Baskir,01; Chen,02], and proteins [Eggins,02; Nagayama,97; Kasemo,02; Tirrell,02; Gilardi,02; Shipway,01], directly in aqueous biological buffer media are subjects of expanding research areas of surface science. Understanding of the behaviour of immobilised two-dimensional biomolecular assemblies is important in fundamental respects but also holds a range of evolving perspectives in bio- and nanotechnology. Such areas, suitably gathered under the heading of "biological surface science" [Zhang,02; Hianik,02], extend to: (a) New generation biosensors and biochips for screening and diagnostics based on assemblies of proteins or DNA-fragments in well-defined supramolecular surface structures. This is probably the immediately most conspicuous bio- and nanotechnologial perspective. Sensing can apply to enzyme substrates, oligonucleotide hybridisation, or antigen-antibody recognition. Other applied perspectives are in the areas of (b) Support for attached tissue cultures and tissue engineering [Kasemo,02; Telegdi,98A] ("biofilms"); (c) biocompatibility of metallic and nonmetallic implants [Walavaara,98]; (d) surface chemistry of medical devices and blood compatibility [Kasemo,02] (anticoagulation); (e) biologically induced corrosion [Telegdi,98B]; (f) pharmaceutical drug delivery [Lasic,95; Storm,98]; and, (g) biomimetic materials and surface science [Kasemo,02; Tirrell,02].

Interactions between biological molecules or whole cells, and solid surfaces span many orders in lateral extension. Primary interactions are, however, at the single-molecule or -macromolecule level. Surface science approaches to molecular interactions with non-metallic and metallic surfaces have rested on: spectroscopy (reflection spectroscopy and ellipsometry [Brash,95; Avila,00; Gaigalas,97], surface enhanced resonance Raman (SERR) [Dong,95; Oellerich,02], surface plasmon [Green,00], fluorescence [Enderlein,00; Perez-Luna,02], and X-ray photoelectron (XPS) [Chi,00; Facci,02] spectroscopy), piezoelectric techniques (quartz microbalance [Tüdos,95], microcantilever sensor techniques [Fritz,00; Moulin,00; Raiteri,01]), (non-electrochemical) impedance spectroscopy [Kasemo,02], adsorption isotherms [Brash,95], and electrochemical methods [Davis,00A; Armstrong,00; Jeuken,02;

Chi,99; Chi,01] (voltammetry, capacitance measurements, electrochemical impedance spectroscopy). Common to these is that they address molecular surface properties averaged over two-dimensionally macroscopic assemblies. In recent years these approaches have been combined with scanning probe microscopies (SPM), particularly atomic force (AFM) [Radmacher,94; Rief,97; Balashev,01] and scanning tunnelling microscopy (STM) [Andersen,95; Zhang,96A; Andersen,97; Friis,97; Friis,99A; Davis,02] of biological macromolecules directly in the aqueous biological media (*in situ* AFM and STM).

Single-molecule structural and functional *in situ* SPM mapping requires, first that the bio(macro)molecules and the solid substrate are chemically compatible. The proteins should be immobilised in well-defined orientations by adsorption or covalent linking via given surface residues. Linking should, however, be gentle enough that electronic or other function is retained. Few proteins comply naturally with this requirement. Metalloprotein immobilisation could instead be achieved by surface residue engineering into the protein, or by attaching suitable linker groups to the solid surface. The former approach also requires great care to ascertain that the engineering does not significantly perturb the protein function. Surface linking also requires suitable conduct in the choice of linker molecule. Long spacer molecules invoke the smallest perturbation on the molecule but the interfacial electronic communication between the functional protein and the substrate is strongly attenuated and the lateral mobility increased as the length of the spacer increases. Linker groups should therefore be as short as possible but still complying with negligible functional disturbance.

The importance of functional protein immobilisation in well-defined monolayers extend naturally to both non-redox and redox proteins and enzymes. Most conceivable electronic device function is, however, associated with redox proteins and enzymes, particularly those based on functional transition metal sites [Gilardi,01]. Low-lying redox levels are of course the central pre-requisite for facile electron exchange between the redox protein and the metallic electrodes in bioelectrochemistry and bioelectrochemical sensors. Metallic redox sensors also hold perspectives for insertion into more sophisticated configurations such as STM and *in situ* STM, where single-molecule electron exchange with *two* metallic contacts is feasible. This opens perspectives for probing molecular mechanisms of electron tunnelling through the

protein matter and even for the discovery of novel electron transfer *phenomena* [Kuznetsov,92; Kuznetsov,01; Kuznetsov,00]. Coupling of molecular and biomolecular redox centres to two mesoscopic surfaces would also be the basis for asymmetric current-voltage relations with obvious *principal*, although perhaps presently not yet accomplished perspectives for molecular rectification, amplification, and other single-molecule electronics [Kuznetsov,02].

Horse heart cyt *c* (HHCC) immobilised by nonspecific adsorption on gold and by covalent linking to platinum surface oxide layers [Andersen,97], and horse radish peroxidase covalently immobilised on highly oriented pyrolytic graphite (HOPG) [Zhang,96A] were the first metalloproteins to be structurally mapped to molecular resolution by *in situ* STM under electrochemical potential control. Other proteins for which molecular resolution by STM in aqueous buffer has been reported include rubredoxin [Mukhopadhyay,00], metallothionein [Maret,02], and cytochrome P-450 [Djuricic,02], but these data were obtained without electrochemical potential control. *Pseudomonas aeruginosa* azurin on single-crystal Au(111) has been subjected to the most comprehensive *in situ* STM studies of a metalloprotein [Chi,00; Chi,99; Chi,01; Friis,97; Friis,99A]. This protein can be immobilised directly on Au(111) via a protein surface disulfide group, or in the opposite orientation via a hydrophobic surface region on Au(111)-surfaces modified by variable-length alkanethiols. In either case the protein retains ET function as shown by comprehensive electrochemical data. *P. aeruginosa* azurin immobilised covalently on Au via a linker molecule has also been mapped to molecular resolution and shown to display voltammetric activity in this immobilised state.

In this work is investigated the adsorption, interfacial monolayer voltammetry, and *in situ* STM under full potentiostatic control, of another redox metalloprotein, *Saccharomyces cerevisiae* (yeast) iso-1-cytochrome *c* (YCC) on single-crystal Au(111)-electrode surfaces. This molecule was chosen for the presence of a Cys residue close to the protein surface (Cys102) at a moderate distance from the heme group (Fe-S distance 11.2 Å [Louie,90]). The thiol group offers a link to the Au-surface. Surface immobilisation is, however, less stable than for azurin as exposure of the thiol group requires some conformational pre-organisation of the protein. This is reflected particularly in the monolayer voltammetric data.

No previous study of monolayer YCC voltammetry on pure polycrystalline or single-crystalline Au-electrodes has been reported. Reversible diffusion voltammetry of YCC and YCC mutants in phosphate buffer at polycrystalline Au-electrodes modified by 4,4'-dithiobipyridine in the CV and DPV modes has, however, been reported [Komar-Panicucci,94]. The equilibrium reduction potential is 12-50 mV vs. SCE (Standard Calomel Electrode). Dimerisation via the –SH close to the surface is thus a sluggish process. Voltammetry of the unfolded form, where Met80 axial coordination of the heme group is substituted by water or non-native N-donor ligands lowers the reduction potential drastically to values around – 400 mV (SCE). Reduction potentials in this range also emerge when Met80 in HHCC is substituted by exogenous N-donor ligands [Battistuzzi,02]. The reduction potential is thus a useful fingerprint of the degree of denaturation and non-native residue axial coordination of YCC. This will be important in the assessment of the functional state of YCC adsorbed directly on Au(111)-electrodes, cf. below.

Electrochemical methods (linear sweep and differential pulse voltammetry, interfacial capacitance data) and XPS, combined with *in situ* microcantilever sensor techniques and *in situ* STM, both directly in aqueous buffer, have been used to investigate YCC on Au(111). The latter two techniques are novel in the context of redox metalloproteins. Yeast cyt *c* is thus only the second redox metalloprotein (in addition to *P. aeruginosa* azurin) for which *in situ* STM has been combined broadly with single-crystal electrochemistry and other methods in a comprehensive approach to *in situ* redox protein monolayer behaviour. Microcantilever sensor recording of adsorbed metalloproteins in aqueous solution has not been reported before, but the data reported do not qualify for the true notion *in situ* as the gold-coated microcantilevers were not potentiostatically controlled. The data offer a broadly coherent view of yeast cyt *c* adsorption on Au(111). The molecule seems to be adsorbed via thiolate as reflected by a reductive desorption signal. Electron transfer (ET) function of the heme group is retained although only transiently in native axial coordination, and voltammetric signals of partially denatured yeast cyt *c* with other axial ligands than native Met80 can also be detected. The data, however, substantiate that redox metalloproteins can be structurally characterised to molecular resolution with *in situ* STM under conditions where protein ET function is retained. They also show that *in situ* STM holds prospects both for

structural mapping of a wide variety of adsorbed metalloproteins and –enzymes, and also for mapping of their electronic *function*.

# 2 MICROCANTILEVER SENSOR TECHNIQUES AND RESULTS

## 2.1 Introduction to the microcantilever technique

The microcantilever sensor technique (MCS) originates from the Atomic Force Microscope (AFM) [Binnig,86]. In AFM a μm-sized silicon cantilever equipped with a sharp tip at the end is scanned over a surface. The forces between the tip and the surface depend on the distance. At short distances attractive van der Walls forces dominate. When the tip is scanned over a surface a difference in the topography of the surface will cause the cantilever to bend due to the change in force. By keeping the cantilever – which is essentially a spring – at the same interaction force, it is possible to record the trace of the cantilever over the surface. Hence a view of the topography is achieved. The bending of the cantilever is monitored by shining a laser beam at the apex of the cantilever and recording the deflection of the reflected laser beam on a photosensitive diode as shown in Fig. 2.1.

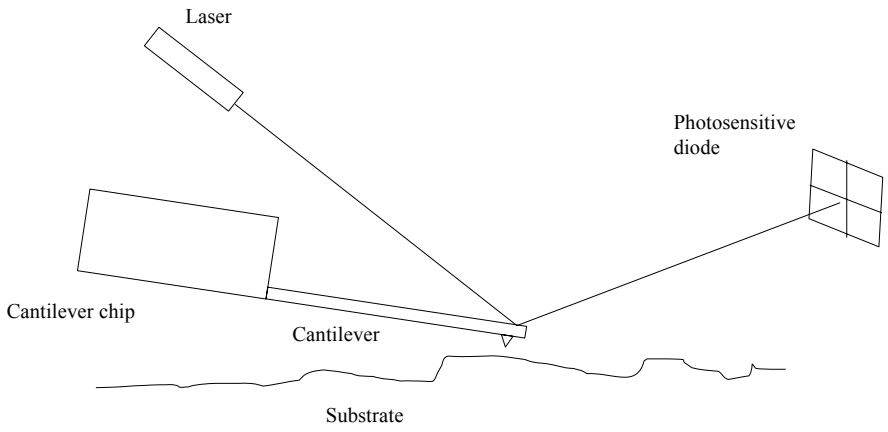


**Figure 2.1**: Sketch of AFM principle.

After the invention of AFM it was discovered that the thin silicon beams used for scanning surfaces can act as excellent probes also without tips [Gimzewski,94;

Thundat,95]. At the µm scale the micrometer-sized silicon beam (or microcantilever) is soft and therefore very sensitive to interactions at this scale. There are in principle three modes of operation (shown schematically in Fig. 2.2):

1) Mass sensing,
2) heat sensing and
3) surface stress sensing.

1) The microcantilever can detect mass changes on the beam by a change in the beam resonance frequency [Berger,97A; Berger,98A; Tamayo,01; Hagleitner,01; Thundat,99]. When molecules adsorb to the microcantilever the resonance frequency will increase due to the increased mass loading. The mass change is calculated from (2.1), where K is the cantilever spring constant and $f_1$ and $f_0$ are the resonance frequencies of the cantilever before and after mass loading

$$\Delta m = \frac{K}{4\pi^2}\left(\frac{1}{f_1^2} - \frac{1}{f_0^2}\right) \qquad (2.1)$$

2) If the cantilever contains two layers with different thermal expansion coefficients, then a change in temperature will cause the layers to expand or contract to a different extent. The temperature change can come from the environment but also from reactions occuring on the cantilevers [Berger,96]. The cantilever will react by bending, until the forces have been balanced.
3) If molecules adsorb selectively on one side of the cantilever, a surface stress can be generated. If the molecules, for instance repel each other, the molecular layer will expand causing the cantilever to deflect [Berger,97B]. The strain in the molecular layer is counterbalanced by the strain in the cantilever.

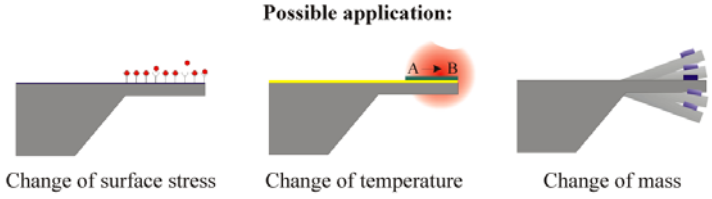


**Figure 2.2**: Three operation modes of a cantilever sensor.

## 2.2 Piezoresistive microcantilevers

In this thesis the microcantilever sensor is applied as a surface stress sensitive tool. The microcantilever sensor originates from the ph.d. project of Anja Boisen [Boisen,97]. The goal was to produce AFM cantilevers with embedded piezoresistors thereby avoiding the need for laser equipment to record the deflection of the cantilever. The project led to the creation of the Bioprobe Project, which focusses on the use of cantilevers as surface stress sensors. The piezoresistor consists of a polycrystalline silicon layer. When the piezoresistor (resistance R) is subjected to strain, the resistance in the piezoresistor will change by $\Delta R$. For small strains the resistance change is proportional to the strain [Chen,93]. The microcantilever chip contains two microcantilevers. One cantilever is the 'working' cantilever that can adsorb molecules when functionalized. The other one placed nearby serves as a reference. The cantilevers will bend not only due to adsorbing molecules but also due to temperature changes, turbulence, or convection. The reference cantilever is equipped with an identical piezoresistor but is not functionalized; in addition two identical piezoresistors are placed on the chip. These piezoresistors will not change resistance either due to molecular adsorption. The four piezoresistors are connected in a Wheatstone bridge (Fig. 2.3).

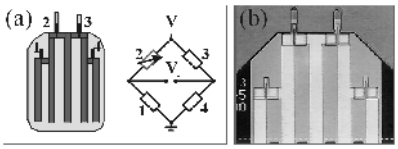


**Figure 2.3**: (a) Schematic drawing of the cantilever chip and the integrated Wheatstone bridge. (b) Optical microscope image of the two cantilevers and the four piezoresistors on the chip. The cantilevers are 200 µm long, 50 µm wide and approximately 2 µm thick.

The change in resistance caused by molecular adsorption is low compared to the resistance of the piezoresistor, hence the output voltage $V_{out}$ is directly proportional to the relative resistance change $\Delta R$ of the working cantilever piezoresistor and the voltage supplied $V_{sup}$ to the Wheatstone bridge [Boisen,00], according to (2.2)

$$V_{out} = \frac{1}{4}\frac{\Delta R}{R} V_{sup} \tag{2.2}$$

The relation between the relative resistance change and surface stress change has been derived by Jacob Thaysen and Ole Hansen [Thaysen,01]. Table 2.1 is comprised from this model. The surface stress sensitivity at a Wheatstone bridge voltage supply of 4 V is denoted $\Delta\sigma_s/\Delta V$.

Three designs of chips have been used: Poly 5, Fagpakke 1, and Fagpakke 2. Poly 5 is an older design, which does not contain metal overlayers. They are evaporated onto the working cantilever afterwards. Poly 5 and Fagpakke designs otherwise contain the same layers and differ only in thickness of the layers (Fig. 2.4). Fagpakke chips were developed later and designed for higher sensitivity. In some experiments a 10 nm gold layer were evaporated onto the gold overlayer of the working cantilever prior to an experiment in order to have a fresh gold layer for adsorption. Hence sensitivies for 70 and 80 nm gold overlayers are also supplied.

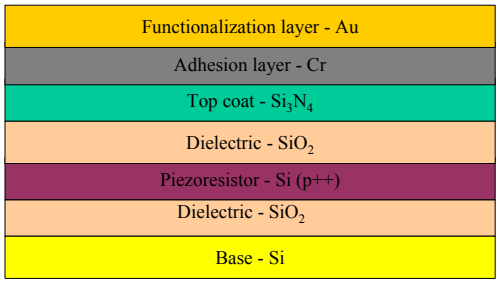


**Figure 2.4**: Sketch of the layers of the working cantilever. A microcantilever contains silicon at the base. On top of the base is the piezoresistor of p++-doped polysilicon sandwiched between two layers of $SiO_2$. An insulating layer of silicon nitride is placed on the $SiO_2$ layer. The working cantilever is functionalized with a layer of Cr and Au. The reference cantilever is is not functionalized.

**Table 2.1**: Layer thicknesses and sensitivies of the two chip designs used. Only the working cantilever contains the metal overlayers. The sensitivity is calculated for a 4 V DC bridge supply and for three thicknesses of the gold layer.
Calculations by P. Rasmussen is gratefully acknowledged.

| | Poly 5 | Fagpakke 1 | | | Fagpakke 2 | | |
|---|---|---|---|---|---|---|---|
| Metal overlayer 2 – Au (nm) | 60 | 60 | 70 | 80 | 60 | 70 | 80 |
| Metal overlayer 1 – Cr (nm) | 15 | 15 | | | 15 | | |
| Top coat – $Si_3N_4$ (nm) | 120 | 80 | | | 80 | | |
| Dielectric – $SiO_2$ (nm) | 100 | 100 | | | 100 | | |
| Resistor – Si (p ++) (nm) | 300 | 176 | | | 176 | | |
| Dielectric – $SiO_2$ (nm) | 1000 | 720 | | | 720 | | |
| Base – Si (nm) | 200 | 230 | | | 230 | | |
| Sensitivity $\Delta\sigma_s/\Delta V$ ((N/m)/V) | 6787 | 2984 | 3009 | 3035 | 3151 | 3177 | 3204 |

## 2.3 Applications

Focus in the following is on stress changes, which are also the basis for the experimental work described in subsequent sections. Cantilever-based sensors hold promise for applications as biodetectors and pollution detectors. Biodetection could be envisaged by binding of antigenes in a sample to cantilevers functionalized with the corresponding antibody. Detection of gene sequences would be by cantilevers functionalized with a complimentary DNA strand. Pollution detectors could be used in the monitoring of for instance heavy metal atoms in waste water or airborne pollutants. An array of cantilevers coated with different chemical compounds sensitive to specific analytes can in principle be applied as an "artificial nose", by monitoring either mass changes or surface stress changes, as the microcantilevers react with different analytes.

GAS PHASE APPLICATIONS

In the beginning microcantilevers were mainly applied as gas detectors, sensing for example alcohols [Lang,99A; Jensenius,00], alkanethiols [Berger,97B], natural flavours

[Lang,99A], ethene [Lang,99B] and water vapour [Lang,99A]. Gas detectors capable of detecting *mixtures* of analytes have recently been reported [Baller,00; Kim,01]. Moreover, microcantilevers acting as mass detectors have been applied to follow the gas-solid interface reaction between dihydrogen and platinum dioxide [Thundat,99]. Microcantilevers have also been applied as thermogravimetric sensors. The enthalpy change of a phase transition of picoliters of an alkane was determined by this method [Berger,96].

## LIQUID PHASE APPLICATIONS

The high sensitivity and rapid response of the microcantilevers make them attractive in studies and detection of biomolecules. The study of biomolecules requires, however, liquid environment in order to retain their physiological structure and function. The step from the gas phase to the 'biocompatible' liquid phase represents a challenge. The introduction of liquid requires operations to take care of the problems associated with it, i.e. protecting electronic circuits from liquid; prevention of leakage, prevention of bubbles in microsystems; mixing liquids. Biomolecules often require certain conditions in order to stay functionable, i.e. correct pH, ionic strength, and surface modifiers. One example of cantilever-based surface stress detection in liquid is the investigation of the adsorption of low-density lipoproteins and plasma proteins [Moulin,00]. Others include adsorption of DNA strands on gold-coated microcantilevers [Marie,02]. Detection of hybridisation of single-stranded DNA to target DNA immobilized on a microcantilever was achieved [Fritz,00; Hansen,01; McKendry,02]. Also detection of prostate-specific antigen by immobilized antibody was accomplished [Wu,01]

## GOLD-SULFUR INTERACTION

The mechanical response of a cantilever is extremely sensitive to the structural and chemical composition of the analyte sensitive layer on the cantilever. Sulfur is known to bind strongly to gold and provides a perspective for detailed studies of the adsorption of a broad variety of sulfur containing molecules on a gold-coated cantilever. Also, the strong sulfur-gold binding can be used to immobilize even complex analyte sensitive layers on the cantilevers. Alkanethiols consist of an alkyl chain with a thiol group (-SH) at the end. Alkanethiols have been extensively studied by other techniques such as AFM

[Xu,98], STM [Hagenström,99; Sawaguchi,00; Delamarche,96; Giz,99], cyclic voltammetry [Diao,99], and surface plasmon resonance spectroscopy [Peterlinz,96]. Alkanethiols can thus be used as well characterised model systems for the study of adsorption of sulfur containing molecules on gold by a variety of techniques including microcantilever technique. Alkanethiol adsorption on gold from the gas phase has previously been studied by cantilever techniques by Berger et al [Berger,97B]. They found that the surface stress change increases linearly with increasing chain length of the alkanethiol [Berger,97B]. The adsorption kinetics were explained by simple Langmuir isotherms [Berger,98B]. Moreover, detection of hybridisation of thiol modified oligonucleotides immobilized on gold-coated cantilevers in aqueous buffer by differential stress effects has been reported [Fritz,00].

The adsorption of sulfur containing molecules on gold also depends strongly on the quality of the gold surface [Xu,98]. The ability of a gold surface to adsorb sulfur molecules decreases rapidly as the gold is exposed to ambient air. Freshly deposited or freshly cleaned gold surfaces are normally used in adsorption experiments. The gold cleaning methods include temperature annealing [Xu,98; Eberhardt,98], ozone [Fujihira,00] or oxygen plasma treatment [Walczak,95] and piranha (hydrogen peroxide+sulfuric acid) etch [Peterlinz,96; Diao,99], i.e., mostly by oxidation processes.

## 2.4 Microcantilevers in gas phase

In this section experimental work on the microcantilever used as a gas sensor is described. The response of a gold-coated microcantilever to vapours of the alkanethiol $CH_3$-$(CH_2)_5$-SH (hexanethiol) is investigated after cleaning of the gold surface by different methods. Two oxidative cleaning methods are used: Oxygen plasma and aqua regia (hydrochloric acid + nitric acid) treatment. In addition the effect of the time of exposure of as-deposited gold surfaces to ambient air is examined. One goal was to be able to reproduce adsorption experiments with the same cantilever. Another goal was to understand the kinetics of adsorption of thiol compounds on gold surfaces subjected to different pre-treatments. These issues are important, if the chips are to be reused and if signals from different cantilevers are to be compared. Finally, for sensor application it is

of interest to find a cantilever surface, which adsorbs a large amount of molecules, inducing a high surface stress signal. To our knowledge investigations, which focus on pre-treatment methods and re-use of the same gold surface, have not been reported for the gold-microcantilever system before.

### 2.4.1 Experimental

The Poly 5 chips were used for these experiments. As produced these chips did not contain a metallic overlayer, thus layers of 10 nm of chromium and 60 nm of gold were evaporated onto the working cantilever. Before each alkanethiol adsorption experiment the chip was treated in one of three ways:

1. CLEANING BY AQUA REGIA (AR)

The cantilevers were immersed in a dilute solution (33% by volume) of aqua regia in de-ionized (DI) water for 60 seconds. Aqua Regia is a mixture of one part concentrated nitric acid (65 %) and three parts concentrated hydrochloric acid (37 %). Afterwards the cantilevers were washed thoroughly in DI-water.

2. CLEANING BY OXYGEN PLASMA (OP)

The cantilever chip was cleaned in an oxygen-/nitrogen plasma for five minutes. The flow rates of oxygen and nitrogen were 200 and 22 sccm/min. The addition of 10 % nitrogen serves to stabilise the plasma. The plasma is supplied with a radio frequency (r.f.) power of 100 W.

Dioxygen is split into to oxygen atoms when it is subjected to a radio frequency (rf) potential at reduced pressures. The oxygen atoms are more reactive than dioxygen. Hence combustion processes can take place at room temperature instead of at elevated temperatures. The gentle combustion process allows selective cleaning of organic impurities at surfaces, i.e. the cantilever. The process is controlled by the r.f. power and the flow rate of the gasses used. Commonly used gasses for plasma etching are $O_2$, $N_2$, Ar and $CF_4$. Dinitrogen and argon are separated into positive ions and electrons. The positive ions are able to sputter the surfaces, which also cleans the surface. Therefore the cantilever surfaces are cleaned both by combustion and sputtering.

3. NO CLEANING

The cantilevers were used without any pre-treatment.

The cantilever chip was next transferred to a measurement chamber consisting of a closed 15 ml polypropylene tube with electrical feed-throughs for data acquisition. 6 µl liquid hexanethiol was injected into the chamber app. 5 cm from the cantilevers. The chamber was then sealed, and the liquid allowed to evaporate. The adsorption experiments were conducted at ambient temperature (20-24 ºC) and pressure. The cantilever cleaning and hexanethiol adsorption are shown schematically in Fig. 2.5.

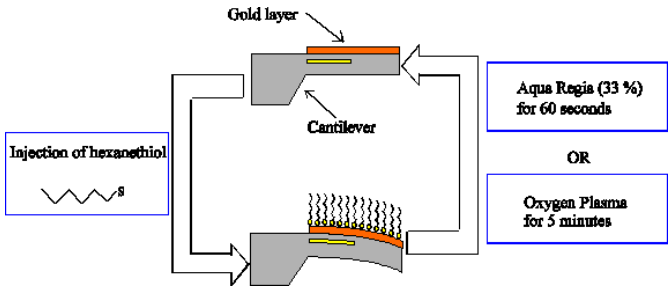


**Figure 2.5**: Procedure of gold pre-treatment and injection of hexanethiol. The liquid is injected approximately 5 cm from the cantilevers.

Hexanethiol adsorption depends on the time elapsed between surface preparation (gold deposition or cleaning of the gold surface) and injection of hexanethiol. Fouling of the gold surface by adventitious carbon is believed to hamper the adsorption process. The time interval between surface preparation and hexanethiol adsorption was therefore kept below 300 minutes in all experiments unless otherwise stated.

AFM Measurements

Tapping mode [Zhong,93] AFM measurements on AR etched gold surfaces were performed on a silicon sample with a thin top layer of silicon oxide and silicon nitride, onto which 15 nm of chromium and 60 nm of gold had been evaporated by e-beam.

This sample is similar to the surface of the measurement cantilever. The freshly evaporated gold surface was first imaged. The sample was then etched for 60 seconds in 33% AR and AFM recorded. The cleaning procedure and the subsequent AFM imaging were repeated three times. A roughness calculation for the sample surface was performed based on AFM images at several sites on the sample. The size of each site was 3 μm × 3 μm. The topography of the site is represented by the height parameter, z. The roughness parameter, $S_q$ is the standard deviation of all z-points (the relative height of each point) from the overall average of z-points[1].

AFM images depend on the sharpness and shape of the tip. The same AFM probe was therefore used throughout the AFM measurements to ease the comparison of the measured roughnesses. Moreover, tapping mode was applied in order to reduce the tip wear during the experiments.

### 2.4.2 Adsorption Model

The adsorption of hexanethiol on the gold surface can be represented by a Langmuir isotherm [Xu,98]. The conditions for using a Langmuir isotherm are that every adsorption site is equivalent, that the concentration of gaseous adsorbant is constant, and that there is no lateral interaction between the adsorbed molecules. It is assume that these conditions are valid, particularly that the concentration of hexanethiol vapour is so high that it can be considered constant during the adsorption. The boiling point of hexanethiol is 151°C [Weast,89]. The vapour pressure at room temperature (20-25°C) is 4 - 6 mbar. The calculation is based on an Antoine equation, which relates vapour pressure with temperature through a set of experimentally determined parameters. The parameters used for hexanethiol have been determined in the temperature range 81-194°C [Osborn,66]. Extrapolation of the values to room temperature introduces therefore some uncertainty in the calculated vapour pressure. Hexanethiol is injected 15 times in excess of what is needed to fill the measurement chamber at the equilibrium pressure. It is therefore believed that adsorption on the gold surface and other surfaces

[1] $S_q = \frac{1}{n}\sqrt{\Sigma(z-\bar{z})^2}$ , where n is the number of data points and $\bar{z}$ is average value of z.

will not consume appreciable amounts of reagent. If the surface stress change is directly proportional to the amount of adsorbed hexanethiol, the surface stress change can then be described by a Langmuir isotherm

$$\Delta\sigma = \sigma_{ML}(1- \exp(-k_{obs}\times t)), \tag{2.3}$$

where $\sigma_{ML}$ is the surface stress change caused by adsorption of a monolayer of hexanethiol, t is the time, and $k_{obs}$ is the observed adsorption rate constant ($s^{-1}$),

$$k_{obs} = k_{ads} \times c + k_{des} \tag{2.4}$$

where $k_{ads}$ is the adsorption rate constant, $k_{des}$ the desorption rate constant and c the concentration of hexanethiol. Desorption of species already present on the surface can be accounted for by a second Langmuir isotherm [Berger,98B].

### 2.4.3 Adsorption of 1-hexanethiol on gold-coated microcantilevers

Fig. 2.6 shows the measured surface stress change as a function of time, for different surface pre-treatments after injection of 6 µl hexanethiol. The positive surface stress change in all curves indicates that the cantilever is bending away from the gold surface as shown schematically in Fig. 2.5. That is, the gold surface is subjected to compressive stress following injection. Compressive stress implies that the hexanethiol molecules repel each other. The interaction between the aliphatic hydrocarbon chains is attractive van der Walls forces and would suggest tensile stress. Alkanethiols constitute, however, dipols [Evans,90], which are able to repel each other electrostatically. Compressive stress formation during alkanethiol adsorption has previously been observed and discussed [Berger,97B]. The data for the non-cleaned and AR cleaned surfaces are obtained by the same cantilever, which has been cleaned between each adsorption experiment. The OP stress curves have also been obtained using a single cantilever which was cleaned in OP before each adsorption experiment.

The surface stress changes are noted to be considerably larger for the AR cleaned cantilevers than for non-cleaned and OP cleaned cantilevers. The maximum surface

stress change for an AR cleaned cantilever is approximately 0.8 N/m, while it is a factor of four less for non-cleaned and OP cleaned cantilevers. However, it has to be noted that the non-cleaned gold surface has been stored in ambient air for ten days.

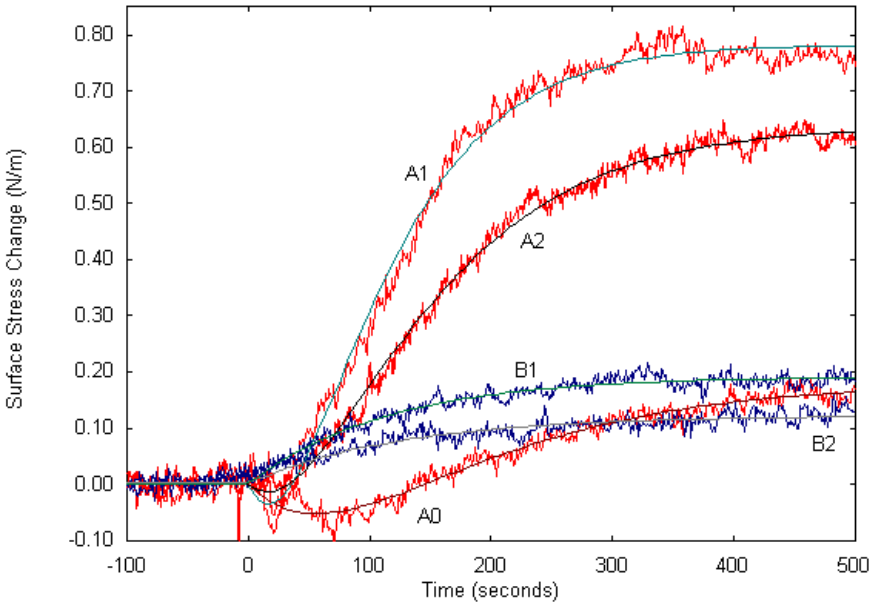


**Figure 2.6**: Surface stress change as a function of time after injection of 6 µl hexanethiol. The data are presented for an as-deposited gold surface (A0) and for the same surface cleaned once (A1) and twice (A2) in AR. Traces B1 and B2 represent a gold surface cleaned for 5 minutes in OP. The adsorption curves are fitted by one (B1 , B2) or two (A0 , A1 , A2) Langmuir isotherms (smooth lines).

The stress curves in Fig. 2.6 are all well described by one or two Langmuir isotherms over the first 500 seconds. Thus, it is concluded that the surface stress developed is proportional to the number of adsorbed molecules. The data for non-cleaned and AR cleaned surfaces contain an initial decrease in surface stress and are therefore fitted by a sum of two Langmuir isotherms. One isotherm represents the build-up of compressive stress, while the other isotherm might represent initial desorption of impurities [Berger,98B]. The rate constants are given in table 2.2.

**Table 2.2**: Adsorption rate constants obtained by fitting Langmuir isotherms, equation (1), to the adsorption data in Fig. 2.6. $k_{ads}$ is calculated by assuming $k_{des,c}$ = 0 and c = 0.19 M derived from the equilibrium pressure of hexanethiol at 22°C.

| Trace | $k_{des,t}$ ($s^{-1}$) (Tensile term) | $k_{obs,c}$ ($s^{-1}$) (Compressive term) | $k_{ads,c}$($s^{-1}M^{-1}$) (Compressive term) |
|---|---|---|---|
| A0 | 0.0114 | 0.0089 | 0.047 |
| A1 | 0.0179 | 0.0165 | 0.087 |
| A2 | 0.0140 | 0.0118 | 0.062 |
| B1 | - | 0.0079 | 0.042 |
| B2 | - | 0.0088 | 0.047 |

From the limited amount of data it can be concluded that AR cleaned surfaces give adsorption rate constants, $k_{ads}$, above 0.05 $s^{-1}M^{-1}$, while the non-cleaned and the OP cleaned surfaces yield rate constants, $k_{ads}$, of 0.04-0.05 $s^{-1}M^{-1}$. Berger et al. have previously measured a substantially higher observed adsorption rate constant, $k_{obs}$, (0.19 $s^{-1}$) for the more volatile but comparable compound, butanethiol [Berger,98B]. Given the equilibrium vapour pressure of butanethiol at 22°: 52 mbar, this would correspond to a $k_{ads}$, of 0.09 $s^{-1}M^{-1}$. Hence $k_{ads}$, is smaller than the reported value for butanethiol by a factor of 1-2. Rate constants for adsorption of alkanethiols in solution on gold decrease with increasing chain length of the alkanethiol [Dannenberger,99]. Alkanethiols with 4 to 22 carbons were investigated. The lower $k_{ads}$ could also be due to the condition of the non-fresh gold surfaces. The rate constant and the maximum surface stress change are similar for the non-cleaned and the OP cleaned gold surfaces. Thus, it seems that an OP cleaning can create a gold surface with the same adsorption properties (and thereby same surface stress signal) as the as-deposited gold surface, which was stored in air for ten days prior to measurement. In contrast to AR cleaned and non-cleaned surfaces the OP cleaned surfaces do not exhibit an initial decrease in the surface stress when hexanethiol is adsorbed. This suggests that initial desorption on OP treated surface does not occur (absence of impurities) or occurs very slowly (on the same time scale as the adsorption of hexanethiol). In the latter case a slower increase in surface stress is observed instead of an initial decrease in surface stress.

AR cleaning provides gold surfaces which can adsorb a large amount of hexanethiol. However, the stress curves obtained are highly unstable and show oscillating signals over longer times. Fig. 2.7 shows on a longer time scale than Fig. 2.6 the surface stress evolution of AR cleaned surfaces subjected to hexanethiol. The stress curves are obtained by the same cantilever, which has been repeatedly cleaned in AR. For all curves the maximum surface stress change is observed 300-400 seconds after injection of hexanethiol. The signal then decreases and reaches a minimum at 1000-2000 seconds after injection followed again by an increase at 2000-3000 seconds after injection. For gold surfaces cleaned once the decrease in surface stress is only about 10 % of the maximum surface stress change. With increasing number of cleanings the surface stress even returns to the level before injection. The curve of the as-deposited surface in Fig. 2.7 shows that the signal has not yet reached a stable plateau. According to a Langmuir adsorption process this plateau corresponds to nearly 100 % adsorption. It is assumed that the maximum stress signal is reached after 1000 seconds, whereafter the signal is dominated by drift, probably caused by temperature changes.

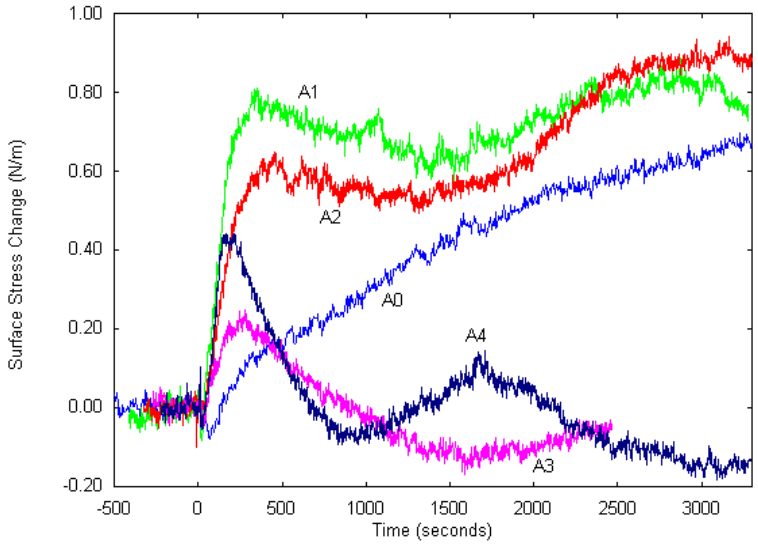


.

**Figure 2.7**: Measured surface stress change as a function of time for injection of 6 µl of hexanethiol. The data are presented for an as-deposited gold surface (A0) and for the same surface after 1st (A1), 2nd (A2), 3rd (A3), and 4th (A4) cleaning for 60 seconds in 33 % AR.

The surface stress change for OP cleaned surfaces and non-cleaned surfaces is slower and the stress signal is lower, but the stress change is permanent and not destroyed by repeated cleanings (not shown).

AFM measurements on AR etched gold surfaces were performed in order to measure the roughness of the etched gold surface, and in order to approach an understanding of the magnitude and behaviour of the oscillatory stress signals (Fig. 2.8). The measured roughness, $S_q$, as a function of etch time is shown in Fig. 2.9. Before the first AR cleaning the surface roughness is approximately 1 nm, and the surface seems featureless (Fig. 2.8a). The freshly evaporated gold surface is imaged. The surface roughness will presumably not change significantly when being left in ambient air. After one cleaning step the surface roughness is approximately 14 nm, which is large compared to the gold layer thickness (60 nm). An AFM image of the surface is shown in Fig. 2.8b. Channels, which are up to 74 nm deep have been etched in the gold layer. After four cleaning steps the surface roughness corresponds to the roughness of the gold surface before cleaning (Fig. 2.8c). The height of the few remaining gold islands is up to 71 nm (Fig. 2.8b+c), which is more than the thickness of the gold layer, indicating that gold as well as parts of the Cr layer have been removed. The colour of the sample after etching indicates, however, that Cr still covers the underlying Si layer completely. Based on this AFM investigation and visual inspection it can be concluded that the 60 nm thick gold layer is almost completely removed after 4 × 60 seconds etch in AR. If the measured stress curves are compared to the AFM images of the gold surface, it seems that the large, metastable stress signals (Fig. 2.7, A1+A2) are only obtained when the surface roughness has not yet decreased. It is therefore proposed that the increased rate constant and stress signal are related to an increased amount of adsorption sites on the gold surface. The use of rough gold surfaces has been shown to induce a larger surface stress signal [Lavrik,01].

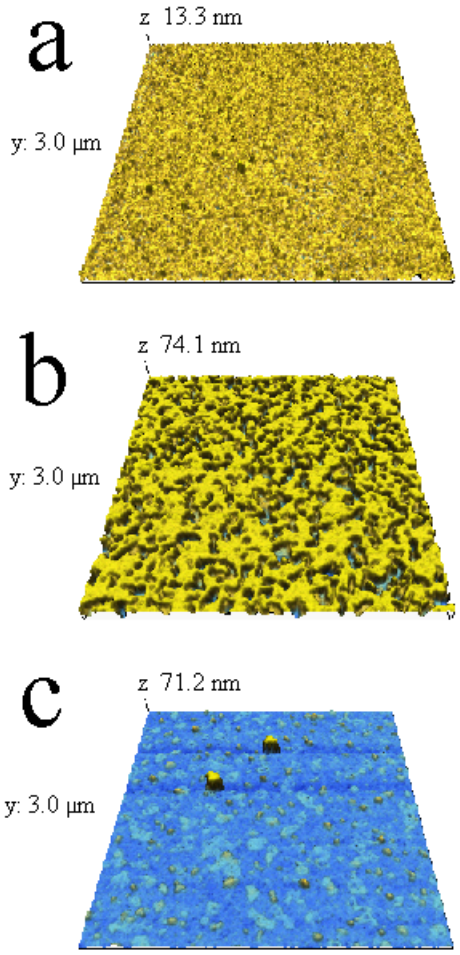


**Figure 2.8**: Tapping mode AFM images of a freshly deposited gold surface (a), the same surface etched for 60 s in 33 % aqua regia (b) and the surface etched for 4 × 60 seconds in 33 % aqua regia (c).

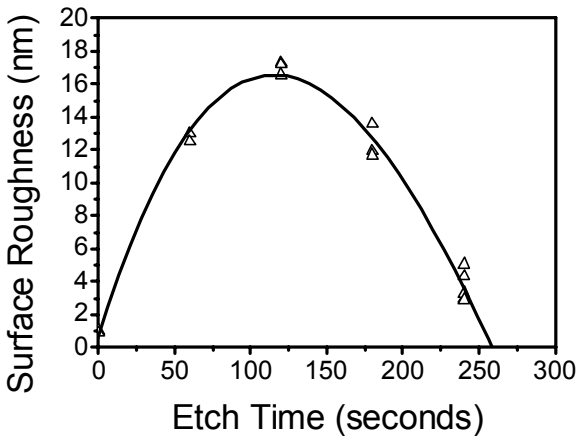


**Figure 2.9**: Roughness parameter, $S_q$, for the gold surface in Fig. 2.8 as a function of etch time in aqua regia. Each measurement point is calculated from a 3 µm × 3 µm surface area.

As the number of AR cleanings increases and the roughness starts to decrease again, the interpretation of the data becomes less straightforward. The gold layer starts to become discontinous and the formation of monolayers of aligned hexanethiol molecules is less feasible. Under these circumstances the transmission of surface stress through the cantilever layers to the piezoresistor may not reflect that of a flat monolayer of hexanethiol molecules. The gold surface does, however, retain high reactivity towards hexanethiol in the initial adsorption phase. High adsorption rates are obtained even after four cleanings, where most of the gold is assumed to be removed. Observation by light microscope indicates that the gold surface on the cantilevers is highly corroded but still present. It may be that the molecules are now being adsorbed on residual gold or on the underlying chromium. Clot et al. have previously reported adsorption of a ferrocene modified alkanethiol on chromium(0). In their experiment the electroactive ferrocene group was attached to undecanethiol. The adsorption depended on the purity of the chromium surface. Prolonged exposure of the surface to oxygen would prevent adsorption of alkanethiol by creating a layer of chromium oxide [Clot,99]. The AR cleaned gold/chromium layer is certainly oxidized.

We speculate that the lack of stability in the stress curves is caused by relaxation of the etched gold layer or rearrangement of the thiol layer, perhaps in combination with the proposed change of the transmission of surface stress to the piezoresistor. Multiple phases in the adsorption process could explain some of the oscillatory character of the surface stress curves. *In situ* AFM [Xu,98] and surface plasmon resonance spectroscopy [Peterlinz,96] suggest that adsorbed alkanethiol monolayers on gold rearrange slowly to create more and more homogeneous monolayers. However, such variations should in principle be visible on all the differently pre-treated gold surfaces. Finally, the existence of binding sites of different energy can obscure the Langmuir kinetics. Electrochemical and STM investigations on strongly terraced Au(111) [Walczak,95] and polycrystalline gold surfaces [Dannenberger,99] indicate that alkanethiols can adsorb at different sites. Walczak et al. measured differences of up to 24 kJ/mol in binding energy for thiols adsorbed at terrace steps and on terraces, respectively. It is certainly possible that the ratio of terraces to terrace steps is changed by AR etching.

Using freshly deposited gold surfaces in the adsorption experiment yields adsorption rates and surface stress changes almost as high as for surfaces cleaned once in AR. Fig.

2.10 shows three experiments with gold surfaces, which were not cleaned prior to alkanethiol injection. One gold surface was used within hours after evaporation, while the others were used after days. The surface stress change is clearly larger for the surface which has been exposed to air only for hours. The surface stress change for the fresh gold surface is about 0.50 N/m after 500 seconds. For a gold surface cleaned once in AR the corresponding value is approximately 0.8 N/m. The data for the gold surfaces stored in air for 10 and 19 days are very similar and the surface stress change after 500 seconds is only approximately 0.25 N/m. Thus, it is clear that the adsorption properties of the gold surface depend on the time the gold has been exposed to ambient air.

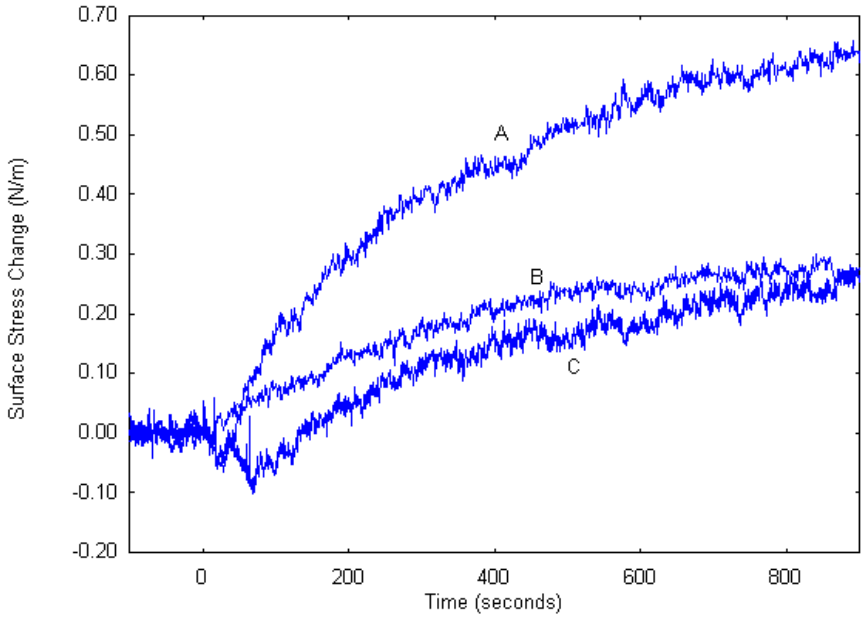


**Figure 2.10**: Surface stress change as a function of time after injection of 6 µl hexanethiol. Data for an as-deposited gold surface for different time intervals between evaporation of gold onto the cantilever and injection of hexanethiol: (A) 100 minutes, (B) 10 days and (C) 19 days.

The measured stress change for the freshly deposited gold is 5 times larger than previously reported by Berger et al. for hexanethiol [Berger,97B]. The different stress signals are very likely related to differences in the deposited gold layers. Moreover, Berger et al. used saturated alkanethiol vapours instead of injection of the liquid form. This might influence the observed kinetics.

### 2.4.4 Conclusion

The kinetics of adsorption of gaseous hexanethiol on gold-coated microcantilevers has been investigated. Two methods of pre-treatment of the gold surface were studied: Immersion in dilute AR (33%) and cleaning in OP. Adsorption of hexanethiol on gold induces compressive stress on the gold surface. The surface stress signals agree well with Langmuir kinetics. The data from non-cleaned and AR cleaned surfaces are better fitted by two Langmuir isotherms, indicating initial desorption of impurities or perhaps more complicated kinetics. Data for OP surfaces are adequately fitted by a single Langmuir isotherm, suggesting a less contaminated surface. The highest adsorption rates and the largest surface stress signals are obtained with AR cleaned gold surfaces. Stress signals are a factor of 4 larger than for OP cleaned and as-deposited surfaces and observed adsorption rates are above 0.010 $s^{-1}$. An additional advantage of the AR cleaning is that it can be performed as an integrated part of adsorption experiments in liquid. In this way, the gold surface of the cantilever will never be exposed to ambient air after the cleaning step. However, the stress curves obtained on AR cleaned surfaces are unstable upon repeated cleanings, and the instability is probably related to the increased roughness of the gold surface. Due to this instability, repeated AR cleaning cannot be used to obtain reproducible adsorption experiments on the same cantilever. However, the method is desirable for obtaining fast adsorption of a large amount of molecules.

The surface stress measurements on OP treated surfaces are more reproducible in the sense that they show Langmuir kinetics with repeated OP treatments. However, the adsorption rate and surface stress change on these surfaces are significantly lower than for AR cleaned and freshly deposited gold surfaces. OP treated surfaces therefore result in a lower and slower surface stress signal.

### 2.4.5 Adsorption of 6-mercaptohexanol on gold-coated microcantilevers

6-mercaptohexanol (MCH) resembles 1-hexanethiol but contains a hydroxy group opposite to the thiol group. MCS adsorption experiments on MCH were conducted in order to see if they could support the results obtained in section 2.4.3.

The acquisition of an ozone cleaner (UV-ozone Photoreactor™ PR-100, Ultra-Violet Products) for cleaning chips was also a motivation for conducting these experiments. In the ozone cleaner a mercury grid lamp emits UV light in two lines: 185 and 254 nm. The two lines induce the reactions:

$$O_2 + h\nu \rightarrow O_3 \text{ (185 nm)}$$

and

$$O_3 + h\nu \rightarrow \text{Free radicals (O•) (254 nm)}$$

The oxygen radicals are considerably more reactive than dioxygen and allows combustion of organic impurities on gold surfaces at ambient temperatures. Hence the method is similar to oxygen plasma cleaning and the main advantage is that the equipment is not shared, which means easier access to the equipment and less risk of contamination from experiments of previous users. The method has been shown to be efficient for gold surfaces [Fujihira,00]. Organic monolayer impurities are removed after 10 minutes of ozone cleaning [UVP manual].

Two kinds of experiments were performed. Chips with gold surfaces that were formerly etched by dilute AR was cleaned 30 minutes in the ozone cleaner. Chips with un-used gold surfaces were also cleaned for 30 minutes in the ozone cleaner. In section 2.4.3 it was suggested that the faster adsorption reaction of hexanethiol on AR cleaned surfaces was due to the larger area of etched gold surfaces. Here the surface pre-treatment differs only by the surface roughness and not by the purity of the gold surface.

Trace A in Fig. 2.11 represents the surface stress change of a cantilever with roughened gold, ozone-cleaned for 30 minutes prior to injection of MCH. The adsorbed MCH layer is subjected to compressive stress. The signal reaches saturation in app. 200

s, where the surface stress change is 0.7 N/m. Trace B represents surface stress change for an un-used cantilever with a smooth gold surface cleaned for 30 minutes in the ozone cleaner prior to injection. The compressive build-up is slower, saturation is reached in 400-500 seconds, but the total surface stress change is also 0.7 N/m.

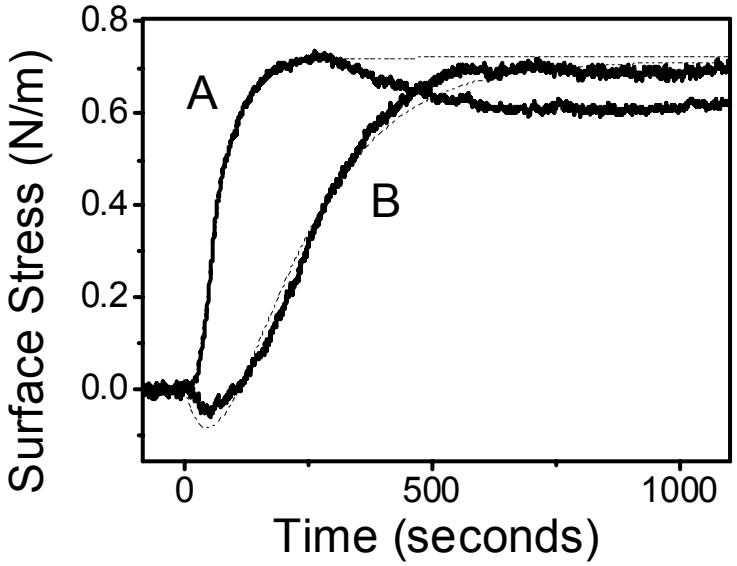


**Figure 2.11**: MCS stress evolution upon injection of 6 µl 6-mercaptohexanol. Trace A is for a rough gold surface (AR etched and ozone cleaned). Trace B is for a smooth gold surface (ozone cleaned).

Experimental values for the vapour pressure of MCH is not available, hence the adsorption rate, $k_{ads}$, can not be calculated. The boiling point of MCH of 225°C is 75°C higher than the boiling point of hexanethiol, which would suggest considerably lower vapour pressure of MCH. Observed adsorption rates obtained from fitting the curves to two Langmuir isotherm are given in Table 2.3. There are however clear similarities with the hexanethiol experiments. Use of a rough gold surface induces a fast adsorption, while smooth surfaces give a slow adsorption. In contrast to the hexanethiol experiments the rough gold surface does not give a larger surface stress signal. The total surface stress change of 0.7 N/m is similar to the results obtained for AR cleaned gold and fresh gold in section 2.4.3. It suggests that the difference in surface stress change

observed in section 2.4.3 is not due to the increased area of AR cleaned surfaces, but rather to the OP cleaning, which is less efficient in cleaning of the gold.

**Table 2.3**: Observed adsorption constants obtained from fitting the curves in Fig. 2.11 to two Langmuir isoterms.

| Trace | $k_{obs,t}$ ($s^{-1}$) (Tensile term) | $k_{obs,c}$ ($s^{-1}$) (Compressive term) |
|---|---|---|
| A | 0.0962 | 0.0222 |
| B | 0.0104 | 0.0074 |

## 2.5 Microcantilevers in liquid phase

In this section we describe attemps to further develop the microcantilever sensor to function in liquid. The functionalization of the cantilever surface is based on the gold-sulfur interaction. Yeast cytochrome *c* (YCC) is an electron transfer protein which takes part in oxidative phosphorylation. YCC is interesting for microcantilever sensing because it contains a cysteine residue near the surface (Fig. 2.12). Cysteine contains a thiol group as hexanethiol and is perceived as a linker group able to attach to the microcantilever gold surface. Furthermore YCC is highly charged (+9 unit charges at neutral pH for the oxidized state) [Armstrong,88] and adsorbed YCC molecules are thus expected to interact electrostatically thereby creating a significant change in surface stress. Secondly YCC is a well characterised protein, which has been studied by a range of techniques including electrochemistry [Feinberg,98], Raman spectroscopy [Wackerbarth,99; Zheng,02], ex situ STM [Zhang,96B], and UV-VIS spectroscopy [Rosell,98].

YCC will be compared with several small sulfur-containing molecules: Cysteine, 6-mercaptohexanol (MCH) and 1-octadecanethiol (ODT). Cysteine is chosen because it is the amino acid through which YCC is believed bind to gold. MCH and ODT are used as references to reveal the effect of the different functionalities: MCH contains an alkohol group opposite of the thiol group. The alcohol group can be envisaged to interact with the hydroxylated silicon nitride reference surface, as can cysteine and YCC. In contrast ODT only contains the thiol functionality and hence should have a less complicated

adsorption pattern, i.e. ODT should only interact with the gold surface. Adsorption of ODT is performed from a mixture of de-ionized water (DIW) and ethanol due to the low solubility of ODT in water.

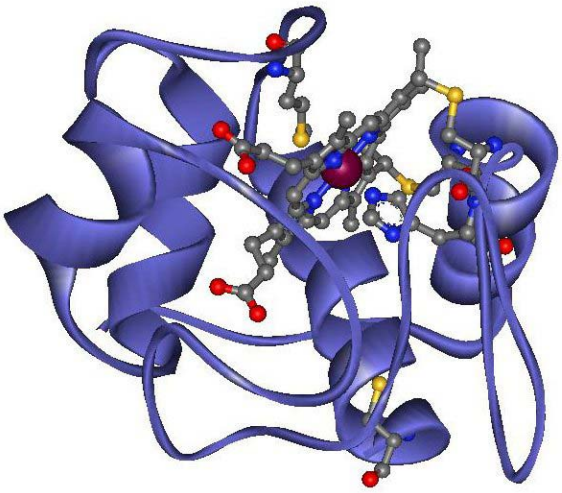

**Figure 2.12**: Crystal structure of YCC showing the heme group and the Cysteine102. Sulfur atoms are shown in yellow [Louie,90].

### 2.5.1 Experimental

SETUP

The microcantilever chip was mounted in an open cell for liquid handling (Fig. 2.13). The cell is made of PEEK (Polyetheretherketone) with inner dimensions 4 × 10 mm. Liquid enters and leaves the cell through teflon tubings of 0.25 mm inner diameter. The inlet and outlet are positioned so that the flow is in the same direction as a line between the cantilevers. In this way the flow will disturb the cantilevers least. Three Hamilton syringe pumps are used for pumping liquids to and from the liquid cell. The Hamilton pumps were chosen because of their ability to control accurately low-level flows.

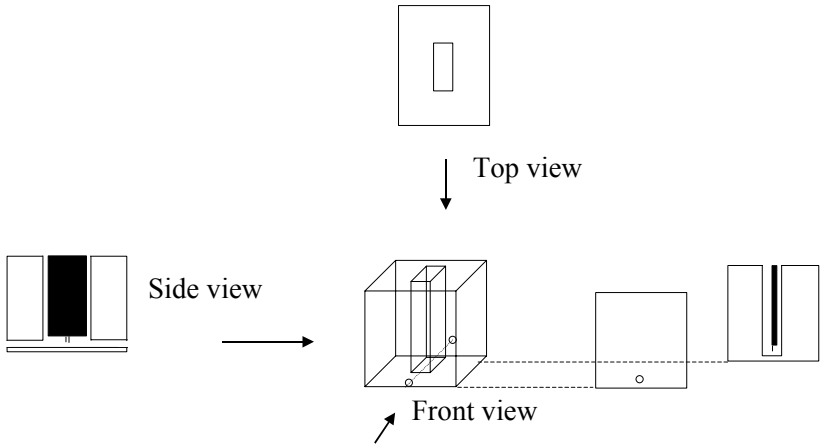


**Figure 2.13**: Schemativ view of the PEEK liquid cell shown from different angles.

Two pumps control the in-flow (Fig. 2.14). A valve directs the in-flows to either the liquid cell or waste. The third pump controls the out-flow from the liquid cell. Glass syringes from Hamilton are used. One syringe contains buffer, one contains buffer with analyte.

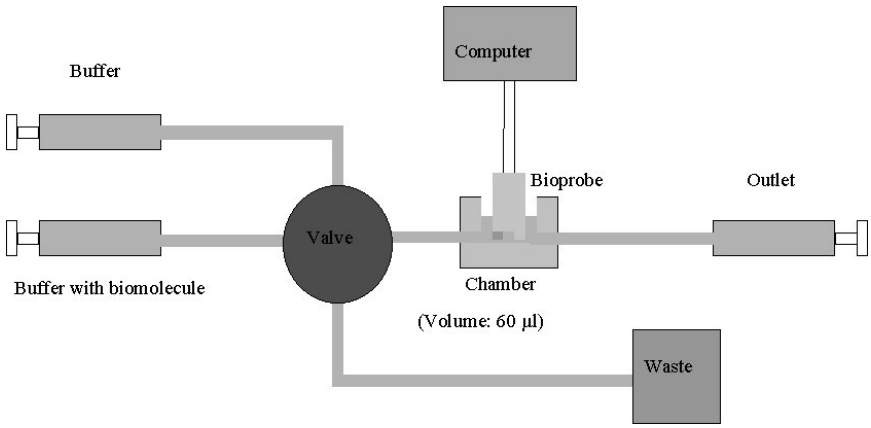


**Figure 2.14**: Sketch of the setup used in liquid phase experiments.

## COATING OF CANTILEVERS

The circuits on cantilever chips to be used for experiments in liquid have to be insulated. A coating of biocompatible Apiezon wax [Chen,93] is applied on top of the chip leaving the cantilever surfaces free.

## CLEANING PROCEDURE

The syringes are cleaned by washing first with DIW, then ethanol and finally with DIW. The liquid cell and tubings are cleaned by flowing 8 ml of 10 % $H_2O_2$ and then 8 ml of DIW through.

Two cleaning procedures for the cantilever chips were used. In most experiments the cantilevers were cleaned in an oxygen plasma under the same conditions as in section 2.4.3. The r.f. power was, however, decreased to 35 W. The use of higher powers could heat the wax to above its melting point (ca. 85°C) and lead the wax to flow out on the cantilevers.

In a few experiments argon plasma was used to clean the cantilever chip. This cleaning was performed in the metal evaporator in connection with evaporation of fresh gold layers (10 nm) onto the working cantilever. The applied r.f. power was 100 W. The wax coating was not damaged in this process.

The cantilever chips were placed in DIW immediately after cleaning and kept there until used.

## MEASUREMENT PROCEDURE

YCC was added to the liquid cell from a 10 mM potassium phosphate solution, pH 7.6. The reference molecules cysteine and MCH were added from aqueous solution, while ODT was added from an ethanol/water mixture (1:2 by volume). Measurements were started by pumping 60 µl of solvent into the liquid cell. A steady flow of solvent (20 µl/minute) was maintained until the readout signal was stable. A flow of analyte to waste was then started. When the solution had filled the tubing, the valve was shifted and the flow of analyte was directed to the liquid cell. The distance from the valve to the

inlet is 20 cm, which corresponds to a transfer time of thirty seconds at a flow rate of 20 µl/minute. The average linear flow velocity is 7 mm/sec. The liquid cell can be flushed by shifting the valve back.

### 2.5.2 Adsorption of yeast cytochrome *c* on gold-coated microcantilevers

Yeast cytochrome *c*

It is important to realize that both the gold and the silicon nitride surface contribute to the output signal. A negative surface stress signal can be interpreted as a situation where both cantilevers exhibit tensile stress, but where the tensile stress on the working cantilever is larger than the tensile stress on the reference cantilever. It might also be, however, that both gold and silicon nitride is subjected to compressive stress, but that the compressive stress on the working cantilever (gold) is smaller than the compressive stress on the reference cantilever. This situation would also result in a negative surface stress signal. It should also be recognized that any deflection of the working and reference cantilever is influenced by adsorption on the silicon surface on the other side of cantilever. The silicon surface is however similar on both cantilevers and will cancel out. In interpretation of the surface stress signals it is in fact easier to image the working and reference cantilever as one cantilever with a gold surface on top and a silicon nitride surface at the bottom.

YCC exhibits tensile stress when introduced into the liquid cell (Fig. 2.15). At time 0 the flow is shifted from phosphate buffer to YCC solution. The readout signal is stable for the first 100 seconds, which is the time it takes the YCC solution to reach the cell and build up a sufficiently high concentration. From 100 to 300 seconds there is a fast change in the surface stress. The stress change is approximately –0.2 N/m. From 300 seconds to 2000 seconds there is a slower change in surface stress (-0.1 N/m). This phase is possibly overlaid with the drift observed before time 0. At 2350 seconds the flow is shifted back to pure buffer. The surface stress signal reacts to the flow change after 2580 seconds with a decrease of 0.3 N/m.

In the first phase from 100 to 300 seconds adsorption of YCC to both cantilever surfaces (gold and silicon nitride) is believed to take place. Physisorption of YCC to

silicon nitride is not unlikely as this surface is highly hydroxylated in aqueous solution [Bousse,92]. The time until 2000 seconds represents a rearrangement phase, where the adsorbed molecules on the gold surface form a more ordered layer. In the third phase physisorbed YCC on silicon nitride is believed to be flushed off. Almost all YCC is flushed off in the first 200 seconds.

The evolution of tensile stress is counterintuitive since the positive charges on YCC are believed to electrostatically repel each other thereby causing compressive stress. The net positive charge is however due to areas of both negative and positive charges. The observation of 50 nm clusters of cyt *c* by *in situ* STM indicates that cyt *c* molecules do not repel each other at a gold surface [Andersen,95].

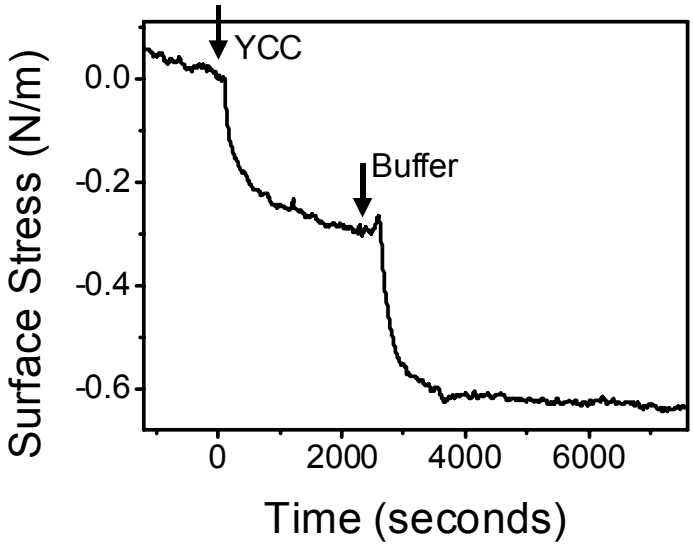


**Figure 2.15**: Time evolution of tensile MCS response. The first arrow shows the time for injection of 95 μM YCC in 10 mM phosphate buffer, pH 7.6. The second arrow shows the response after subsequent flushing with pure buffer. Au-surface pre-treated with OP but not otherwise purified.

Fig. 2.16 shows the MCS response after introduction of YCC solution in different concentrations. The curve for 25 μM YCC contains an initial fast adsorption phase similar to the curve in Fig. 2.15. For 15 and 5 μM the fast phase is less pronounced. The response is faster for higher concentrations but the final stress change is approximately the same. The time when the surface stress signal changes initially also depends on the concentration: For the high concentration, 95 μM, the signal starts to change after 95 s,

for the intermediate concentrations, 15 and 25 μM, it starts after around 150 s, and for the lowest concentration after 180 s. According to the model for Langmuir isotherms the signal should start to change at the same time but with different slopes. The delay for lower concentrations is thought to originate from the geometry of the liquid cell and the inlet tube. The diameter of the inlet tube is 0.25 mm and the width of the liquid cell 4 mm (Fig. 2.13). The cantilevers are located approximately 5 mm from the inlet and are positioned on a line connecting the inlet and outlet points. When YCC is introduced to the liquid cell the concentration is maximal in a 0.25 mm cylinder surrounding the central line. The parameters of the flow in the tube indicate that the flow is laminar. Flow going from a tube of low diameter to a tube of high diameter will however experience some turbulence [McCabe,85]. By diffusion and possibly turbulence the concentration of YCC outside the central cylinder will increase in time. This means that the YCC concentration actually depends on the distance of the cantilevers to the central flow cylinder and on time. The delayed response is thus thought to represent the time it takes to build up a sufficiently high concentration of YCC at the cantilevers.

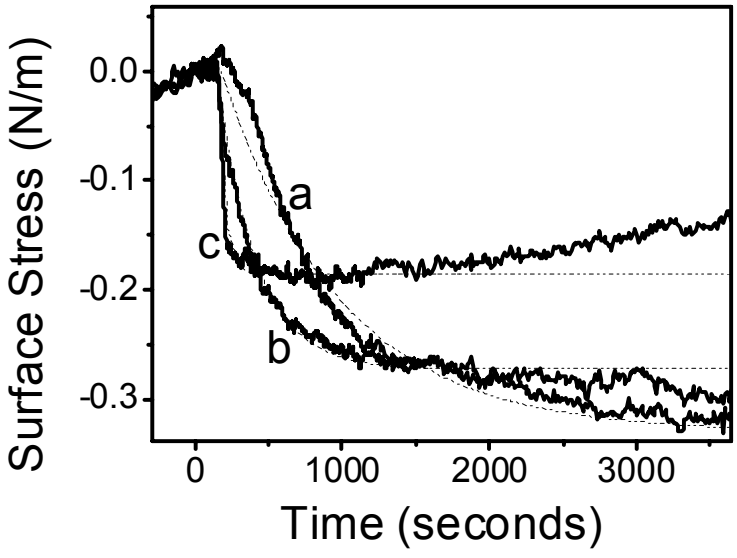


**Figure 2.16**: MCS response after injection of different concentrations of YCC in 10 mM phosphate buffer, pH 7.6. a: 5 μM YCC. b: 15 μM YCC. c: 25 μM YCC. Au-surface was pre-treated by OP.

The curves have been fitted to Langmuir isotherms. The observed adsorption rate constant are shown in table 2.4 and are seen to increase with increasing concentration. The dependance is not linear, however, as predicted by Langmuir kinetics.

**Table 2.4**: Observed adsorption rate constants, $k_{obs}$, and calculated adsorption rate constants, $k_{ads}$ obtained by fitting the curves in Fig. 2.16 to a Langmuir isotherm. The standard fit error of $k_{obs}$ is also shown.

| YCC concentration (μM) | $1/k_{obs}$ (s) | $k_{ads}$ ($s^{-1}M^{-1}$) | Onset of change (s) |
|---|---|---|---|
| 5 | 804 ± 10 | $2.5\times10^{1}$ | 178 |
| 15 | 264 ± 1 | $2.5\times10^{1}$ | 147 |
| 25 | 47 ± 0.6 | $8.5\times10^{1}$ | 153 |
| 95 | 183 ± 4 | $5.7\times10^{1}$ | 96 |

### 2.5.3 Adsorption of reference molecules on gold-coated microcantilevers

L-cysteine

Tensile stress is evolved upon introduction of L-cysteine to an OP cleaned cantilever chip (Fig 2.17). A fast phase of 40-60 seconds was observed 130-170 seconds after cysteine-introduction. The decrease in surface stress is 0.15 N/m. This phase is believed to represent non-specific adsorption. It is followed by a phase lasting for app. 200 seconds in which the surface stress decreases with 0.03 - 0.07 N/m.

When the cell is flushed with DIW the surface stress signal can be brought back to the original within 300 seconds (Fig. 2.18). Hence, the non-specifically adsorbed molecules can be removed. Cysteine is known to adsorb strongly on gold [Zhang,00]. The lack of stable adsorption indicates that the duration of the adsorption process (2000-2500 seconds ) is too short to enable chemisorption of cysteine.

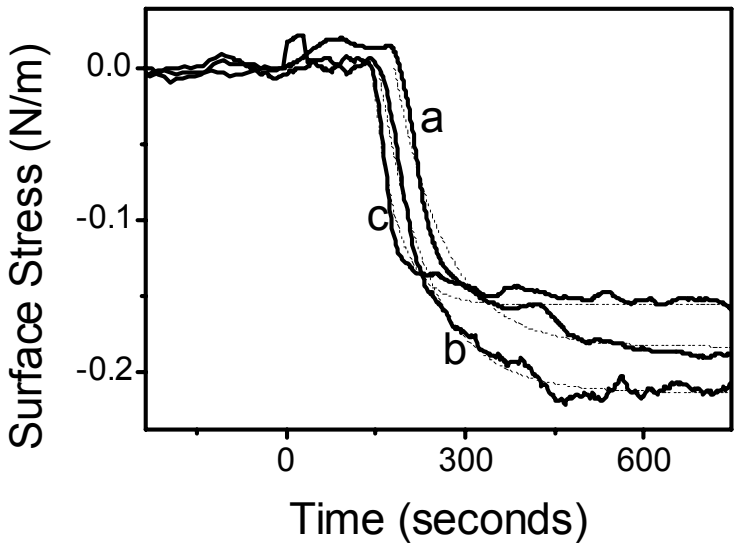


**Figure 2.17**: Tensile MCS stress evolution after introduction of: a: 0.18 mM, b: 0.42 mM, and c: 2.3 mM cysteine in 10 mM phosphate buffer, pH 7.6. The Au-coated MCS pre-treated by OP. Dashed lines represent fits of the curves by a Langmuir isotherm.

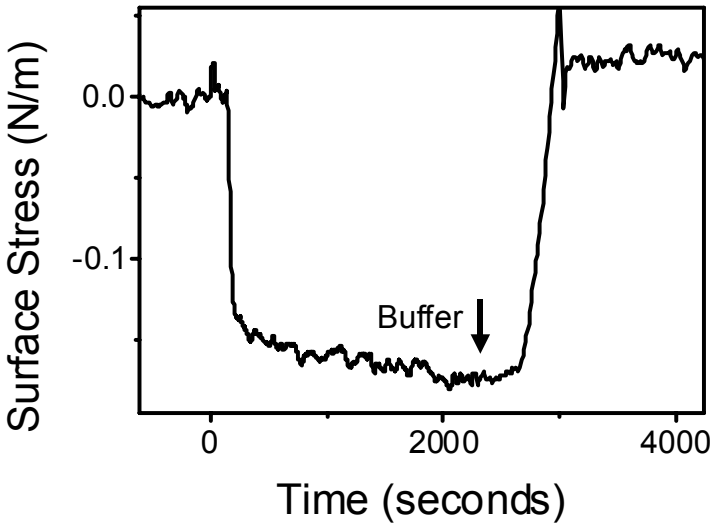


**Figure 2.18**: Continuation of curve c in Fig. 2.17 after flushing the cell with buffer.

The curves in Fig. 2.17 have been fitted by a Langmuir isotherm. The resulting adsorption rate constants, $k_{obs}$ and $k_{ads}$, are shown in Table 2.5.

**Table 2.5**: Adsorption rate constants, $k_{obs}$ and $k_{ads}$, for cysteine on OP cleaned cantilever chips. The standard fit error of $k_{obs}$ is also shown.

| Concentration of cysteine (mM) | $1/k_{obs}$ (s) | $k_{ads}$ ($s^{-1}M^{-1}$) |
|---|---|---|
| 0.18 | 84 ± 1 | 66 |
| 0.42 | 82 ± 1 | 29 |
| 2.3 | 39 ± 1 | 11 |

Compressive stress is evolved after introduction of cysteine to the argon plasma cleaned cantilever chip (Fig. 2.19). The working cantilever contains a freshly evaporated 10 nm gold layer. The total compressive stress change has the same magnitude as for oxygen plasma cleaned chips but with opposite sign. The surface stress change is also slower as reflected by table 2.5. The process is believed to represent chemisorption of L-cysteine on the gold surface.

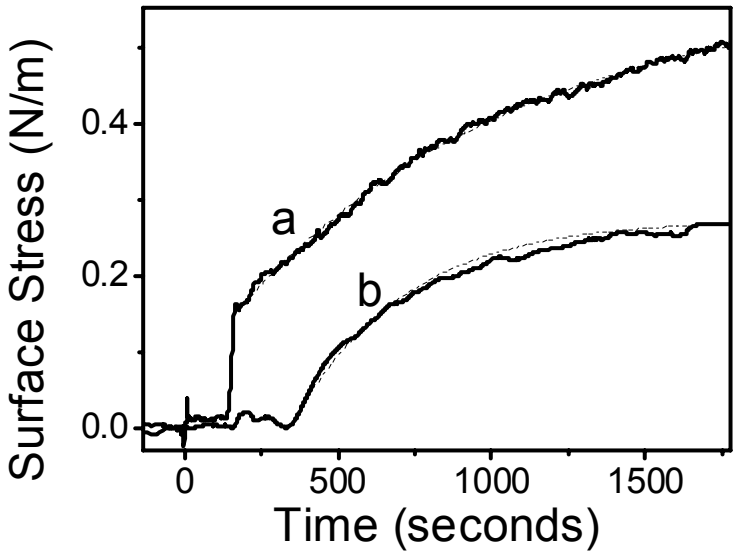


**Figure 2.19**: Compressive MCS stress signal observed when the Au-coated MCS had been purified in argon plasma and a new Au-layer subsequently evaporated. a: 0.43 mM, and b: 0.70 mM cysteine in 10 mM phosphate buffer, pH 7.6. Dashed lines represent fits of the curves to a Langmuir isotherm.

When the cell is flushed with buffer the surface stress signal can be brought back to original in app. 20000 seconds or 100 times as long as for oxygen plasma cleaned chips, strongly suggesting that the signal originates from chemisorption (Fig. 2.20).

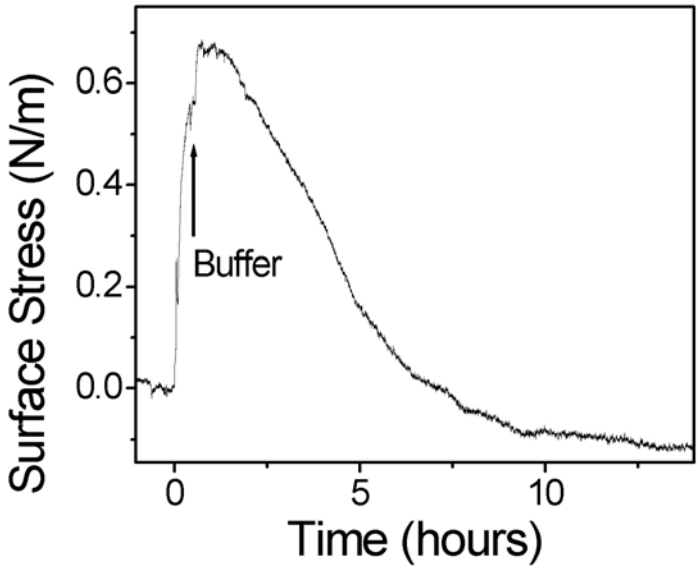


**Figure 2.20**: Continuation of curve a in Fig. 2.19 after flushing the cell with buffer.

Fitting the curves in Fig. 2.19 to a Langmuir isotherm yields the adsorption rate constant shown in Table 2.6.

**Table 2.6**: Adsorption rate constants, $k_{obs}$ and $k_{ads}$, for cysteine on argon plasma cleaned cantilever chips. The standard fit error of $k_{obs}$ is also shown.

| Concentration of cysteine (mM) | $1/k_{obs}$ (s) | $k_{ads}$ ($s^{-1}M^{-1}$) |
|---|---|---|
| 0.43 | 916 ± 6 | 2.5 |
| 0.70 | 366 ± 1 | 3.9 |

6-Mercaptohexanol

0.6 - 0.7 N/m of tensile stress is evolved app. 120-130 seconds after introduction of MCH to an argon plasma cleaned cantilever chip with a freshly deposited gold layer on the working cantilever. The surface stress relaxes, however, after 250-280 seconds and reverts to a more positive surface stress value in a slower process than the initial adsorption (Fig. 2.21). The surface stress change in this second phase is larger for higher concentrations. This biphasic signal undoubtedly reflects the interaction of MCH with both cantilever surfaces: gold and silicon nitride. The reference cantilever material silicon nitride is known to contain a high amount of hydroxygroups in aqueous solution [Bousse,92]. The hydroxygroups might interact electrostatically with MCH thereby causing a surface stress response from the reference cantilever.The first rapid phase bears the characteristics of fast electrostatic adsorption and is most likely adsorption of MCH on the hydroxylated nitride surface. The rate of surface stress change in this first phase is independent of MCH concentration but the onset is sligthy shifted with concentration in accordance with the observations for YCC and cysteine. The second phase does, however, depend on the concentration of MCH. The Langmuir model for adsorption presented in sec. 2.4.2 with two isotherms was used to fit the surface stress response. The two isotherms denote adsorption on the two cantilever surfaces. The observed adsorption rate constant is 3.5 times higher for 1.0 mM MCH than for 0.2 mM MCH (table 2.7). This second phase is ascribed to chemisorption of MCH to the gold surface.

The permanent stress change is different for the two concentrations, which would imply that the coverage on at least one of the surfaces depends on the concentration of MCH in an equilibrium process. This is more likely to happen on the silicon nitride surface where MCH is electrostatically attracted.

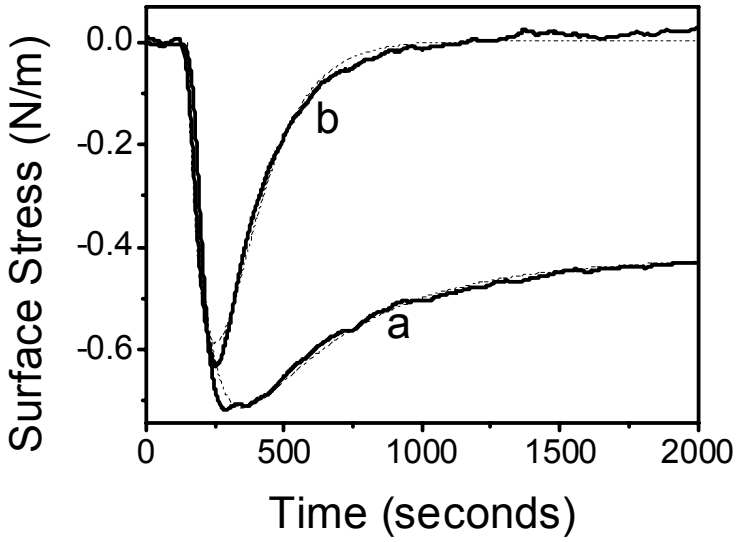


**Figure 2.21**: Surface stress evolution after introduction of 0.2 mM (a) and 1.0 (b) mM MCH to argon plasma cleaned chips with a fresh 10 nm gold layer on the working cantilever.

**Table 2.7**: Adsorption rate constants, $k_{obs}$ and $k_{ads}$, for MCH on Ar plasma cleaned cantilever chips.

| MCH Concentration (mM) | $1/k_{obs}$, tensile term (s) | $1/k_{obs}$, compressive term (s) | $k_{ads}$, compressive term ($s^{-1}M^{-1}$) |
|---|---|---|---|
| 0.2 | 70 | 437 | 11 |
| 1.0 | 87 | 126 | 8 |

1-Octadecanethiol

1-octadecanethiol (ODT) was adsorbed onto microcantilevers from a 1.0 µM solution in a mixture of 1 part ethanol and 2 parts DIW (by volume). Ethanol is necessary in order to solve ODT. A too high concentration of ethanol will solve the wax protecting the chip circuitry, however. Injection of 1.0 µM 1-octadecanethiol causes compressive stress for a microcantilever chip that has been cleaned by Argon plasma and where 10 nm of gold has been evaporated onto the working cantilever immediately

before use (Fig. 2.22). A small fast compressive stress signal evolves app. 120 seconds after introduction of ODT. The compressive signal peaks at 190 seconds at the value 0.03 N/m. The surface stress is then shifted negatively (tensile stress) in a slower process. The surface stress signal stabilises after app. 2000 seconds at the value –0.16 N/m.

Adsorption of alkanethiols on gold-coated microcantilevers from the gas phase produced compressive stress [Berger,97B]. Also adsorption of dodecanethiol on gold from ethanol solution gave rise to 0.5 N/m compressive stress [Moulin,98]. One might therefore also expect compressive stress for adsorption of ODT from the ethanol/water mixture. Two important differences may, however, influence the surface stress response. As mentioned for MCH the reference cantilever material silicon nitride is known to contain a high amount of hydroxygroups in aqueous solution [Bousse,92]. The hydroxygroups might interact electrostatically with ODT thereby causing a surface stress response from the reference cantilever. The adsorption process might also proceed differently in an ethanol/water mixture compared to adsorption from pure ethanol.

The Langmuir model for adsorption presented in sec. 2.4.2 with two isotherms was also used for ODT to fit the surface stress response. The two isotherms denote adsorption on the two cantilever surfaces. The fast compressive phase might represent adsorption on silicon nitride. It might also represent release of surface stress as mentioned for gas phase hexanethiol adsorption (sec. 2.4.3). The second tensile phase could represent adsorption of ODT to gold. The adsorption rate constant for the tensile phase, $k_{ads}$, is $3.7\times10^3$ $s^{-1}M^{-1}$ (Table 2.8). The rate constant for ODT adsorption on gold from a pure ethanoic solution is expected to be $2.4\times10^3$ $s^{-1}M^{-1}$ [Dannenberger,99], which is close to the measured $k_{ads}$.

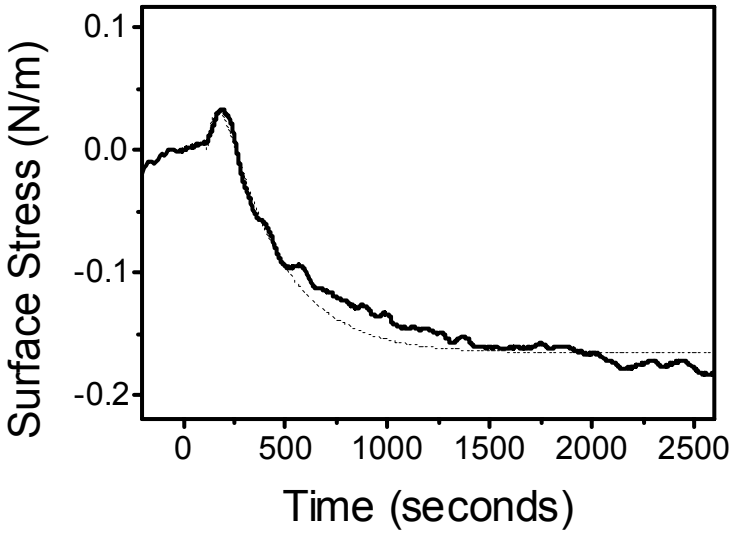


**Figure 2.22**: Surface stress evolution after introduction of 1.0 μM ODT to argon plasma cleaned chips with a fresh 10 nm gold layer on the working cantilever.

**Table 2.8**: Adsorption rate constants for ODT on Ar plasma cleaned cantilever chips. The standard fit error of $k_{obs}$ is also shown.

| ODT Concentration (μM) | $1/k_{obs}$, compressive term (s) | $1/k_{obs}$, tensile term (s) | $k_{ads}$, compressive term ($s^{-1}M^{-1}$) | $k_{ads}$, tensile term ($s^{-1}M^{-1}$) |
|---|---|---|---|---|
| 1.0 | 47 ± 1 | 267 ± 5 | $2.1\times 10^{4}$ | $3.7\times 10^{3}$ |

### 2.5.4 Conclusion

Adsorption of YCC and the small sulfur containing reference molecules cysteine, MCH and ODT on gold-coated microcantilevers was performed. YCC gave a tensile stress signal when injected to a oxygen plasma cleaned microcantilever chip. YCC adsorbed on both the gold-coated microcantilever and the silicon nitride cantilever. Flushing of the liquid cell with buffer removed physisorbed YCC on the reference cantilever, whereby the differential surface stress signal (surface stress on the working cantilever minus surface stress on the reference cantilever) increased to –0.6 N/m

(tensile). The rate of surface stress change depended on the concentration of YCC and followed Langmuir kinetics. For higher concentrations (>25 μM) the rate of surface stress change was largely independent of concentration.

Tensile stress was also observed for adsorption of cysteine on oxygen plasma cleaned cantilevers. The stress signal originated most probably from physisorption of cysteine to both cantilever surfaces. The surface stress signal could be returned to original by flushing the cell with water. Compressive stress was observed for adsorption of cysteine on argon plasma cleaned cantilever with a freshly evaporated gold layer on the working cantilever. The surface stress signal could be returned to original by flushing for app. 10 hours, hence cysteine was believed to be chemisorbed to the gold-coated cantilever.

A fast tensile stress signal (-0.7 N/m, $k_{obs}$=0.01 $s^{-1}$) was observed for MCH adsorption on an Argon plasma cleaned chip followed by a concentration dependent compressive stress signal. The first signal originated from adsorption to the silicon nitride cantilever, while the second signal represented adsorption to gold.

A small compressive signal (0.03 N/m) was followed by a large tensile signal (-0.16 N/m) for adsorption of ODT on an Argon Plasma cleaned chip. The first signal could represent either desorption of impurities or adsorption on the reference cantilever. The second signal could be linked to adsorption to the gold surface. The adsorption rate constant $3.7\times10^3$ $s^{-1}M^{-1}$ was close to the reported value for adsorption of ODT on polycrystalline from ethanol solution [Dannenberger,99].

# 3 STM

## 3.1 Introduction to STM

Scanning Tunnelling Microscopy (STM) was invented in 1982 by Binnig and Rohrer [Binnig,82]. The technique is able to provide topographical data of a conducting surface with atomic resolution.

The technique is based on scanning a sharp tip across a surface thereby providing topographical information. STM relies on three main conditions to ensure its unprecedented resolution: The sharpness of the tip, the quantum mechanical tunnel effect and piezoelectricity.

TUNNELLING

When the conducting tip is sufficiently close to the conducting surface – but not in physical contact – and when a bias voltage is applied between tip and surface, a tunnelling current can flow. The term tunnelling current is used because electrons in the tip (or the surface) do not have sufficient energy to overcome the barrier for conduction. Due to the quantum-mechanical tunnelling effect the electrons do, however, have a finite probability to be transferred. The tunnelling current depends exponentially on the distance, a, between the tip and the substrate and the barrier height $V_0$. The Gamov formula states the probability $\Gamma$ that an electron can pass the barrier

$$\Gamma = \exp(-\frac{2}{\hbar} a\sqrt{2mV_0} \tag{3.1}$$

where ħ is Planck's constant divided by $2\pi$, and m is the mass of the electron. The strong exponential dependence means that almost all current is carried by the outermost atoms of the tip. Hence small changes in tip-substrate distance will cause relative large changes in tunnelling current. This feature can be used to create a detailed topographical image of a substrate with atomic resolution. The barrier height depends on the work function of the substrate, i.e. the minimum energy needed to move an electron from the bulk of substrate to the vacuum level. For metals work functions are in the range 4-5 eV, which amounts to a 9-10-fold decrease of the tunnelling probability and hence the

tunnelling current per Å [Chen,93]. Tunnelling currents are in the nA range, while typical bias voltage are in the 100 mV range. The tip-substrate distance is 5 Å with a tunnelling current of 2 nA at 50 mV bias voltage according to tunnel theory calculations [Friis,99B].

MOVING THE TIP

Nanometer precision is essential in the movement of the tip scanning the surface. The high precision is achieved by the use of piezocrystals. Piezoelectricity was discovered in 1880 by Pierre and Jacques Curie [Chen,93]. It was found that single-crystal quartz, strained in one direction exhibited a voltage difference in the same direction. The dimensional change was linear with the voltage. Later it was found that application of a voltage difference to single-crystal quartz caused compression or expansion of the crystal. The sensitivity of the piezoelectric effect means that movements by nanometers can be controlled by voltages of millivolts. The preferred material for STM piezotubes is lead zirconate titanate (PZT) ceramics, which have sensitivites of 50 Å/V [Chen,93]. PZT ceramics are not naturally piezoelectric. The piezoelectricity is induced by poling the ceramic with application of high electric fields for a prolonged time (60 kV/cm for 1 h). The treatment provides the ceramic with a strong but not permanent piezoelectricity [Chen,93]. Over large time scales the piezoelectricity decays according to a logarithmic law. Scanner heads hence need to be calibrated every couple of months. The background of the calibration procedure used for PicoSPM is described in appendix B.

SHARPNESS OF THE TIP

Tips need to be sharp in order to image a surface with molecular or atomic resolution. The preferred materials for tips are tungsten (W) and platinum/iridium (80:20) (PtIr). Tips are typically etched electrochemically, which will result in tips with radius of curvature in the range 10-100 nm.

Tips do not need to be atomically sharp, however. Cut Pt/Ir wire can produce images with atomic resolution even if the tip looks unsharp in Scanning Electron Micrographs. The distance-dependent tunnelling effect ensures that the current is mostly carried by the outermost atoms of the tip.

SCANNING THE TIP

When the tip is brought within tunnelling distance of the substrate, the tip is scanned across the surface. The x- and y-directions of the scanner span the surface, while the z-direction is the height. The tip is scanned from one corner of a square along the x-direction. STM can be operated in constant-height or constant-current mode. In the former mode the tip is moved across the substrate while the current is recorded, i.e. the tip is only moved in the x- and y-directions. In the latter mode the tip traverses the substrate while a constant current is maintained. The tip is retracted when it scans across a protrusion, i.e. an increase in tunnelling current, while it is brought closer to the substrate, when it encounters a valley, i.e. a decrease in tunnelling current. The z-value – the height – is recorded during scanning and a topograph is directly obtained.

Topographs can also be obtained in constant-height mode. The tunneling current – and not the z-value - is recorded and it depends as mentioned exponentially on the tip-substrate distance. If the distance-current relation is known the z-value can be calculated. The advantage of constant-height mode is that the the tip is not moved in the z-direction, which reduces feedback noise. Hence the lateral resolution is improved. The drawback is that constant height mode does not retract the tip from the substrate should the tip touch the substrate, hence constant height mode is only applied to very flat (atomically) substrates and small areas. Another disadvantage is that the topography of the substrate can be obtained only if the current-distance is known.

FEEDBACK

The constant current in constant current mode is maintained via a feedback loop in the STM electronics. The actual tunnelling current will deviate from the set tunnelling current. The difference is denoted the error-signal. The speed by which the scanner reacts to changes in the surface conductivity (or topography) is determined by three kinds of feedback functions.

1. proportional: the feedback signal is proportional to the error-signal
2. integral: the feedback signal is proportional to the integral (in time) of the error-signal

3. differential: the feedback signal is proportional to the differential of the error-signal

The voltage $V_z$ applied to the piezoscanner to control the tip height is corrected according to a function of the form

$$V_{z,1} = V_{z,0} + P \times \mathrm{err} + I \times \int \mathrm{err} \cdot dt + D \times \frac{d}{dt}\mathrm{err} \qquad (3.2)$$

where err is the difference between the setpoint current and the measured current, t is time, and P, I, and D are the proportional, integral, and differential gain factors, respectively. Too high gain parameters can cause unwanted noise in the image, while too low gain parameters prohibit the observation of details, i.e. the image will appear blurred. Observation of individual atoms requires a fast response, which can be achieved by a high differential gain factor. The integral gain is used to correct for large scale deviations.

APPARENT HEIGHT

One thing to bear in mind when analysing STM images is that STM does not measure topography but conductivity. An STM image of for instance a clean gold surface will directly show the topography of the surface. If molecular adsorbates are present on the surface, however, the conductivity above the adsorbates will be different from the conductivity of the gold. Consequently the tip-adsorbate distance will be different from the tip-gold distance in order to obtain the same tunnelling current, hence the trace of the tip will not reflect the topography accurately.

INSULATION

Because of the nanosized movement of tip and substrate STM is very sensitive to sound and vibrations. Hence STM scanners are suspended from elastic wires and housed in sound-insulated boxes to avoid noise. In addition scanners are designed to have high resonance frequencies, while the other mechanical parts in the STM have low resonance frequencies in order to avoid interference.

DRIFT

Drift in images are observed in the beginning of STM experiments. The drift is due to thermal gradients and different thermal expansions of tip, scanner and substrate. The differences will cause the position of the tip to drift relative to the image center. Due to the relatively long acquisition time and the small structures observed the drift will distort the structures observed and the center of the image will also drift. Use of a high scan speed will reduce the acquisition time and the observed distortion. It will, however, also increase the feedback noise. Images of large areas are less sensitive to drift since the drift becomes relatively smaller.

*Ex situ* STM

The term *ex situ* STM means STM performed at the gas-solid interface, i.e. in the 'dry' state as shown in Fig. 3.1. The first STMs were operated in UHV and limited STM investigations to the study of clean substrates [Tromp,85]. The introduction of STM working in gaseous environment enabled the study of surface dynamics such as catalytic reactions [Hösler,86].

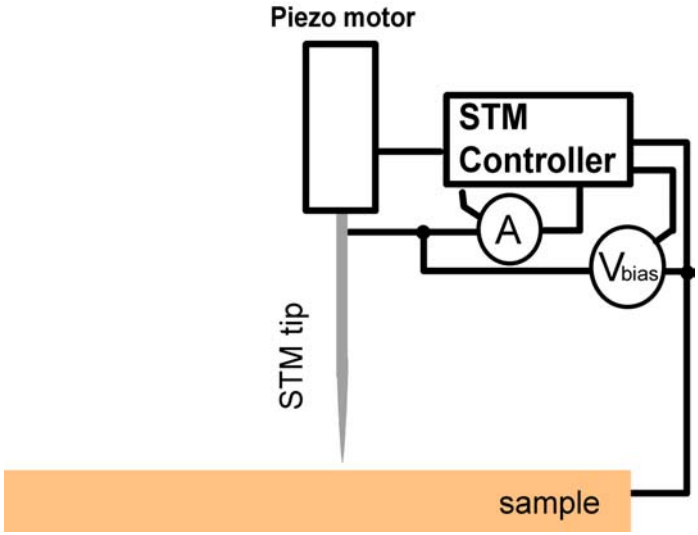


**Figure 3.1**: STM configuration for *ex situ* STM

*In situ* STM

A major improvement of STM was the introduction of *in situ* STM, i.e. scanning at the liquid-solid interface [Sonnenfeld,86]. This development meant new perspectives within chemistry and biology. 'Wet' chemical and biochemical reactions and structures could now be observed. Another improvement was the introduction of individual potentiostatic control of the substrate (Fig. 3.2). Potential dependent conductivity changes could now be investigated. The bond strength of adsorbates usually depend on the surface electrode potential, and hence successful imaging, which relies on the strong attachment of adsorbates, also depends on the electrode potential. Finally the study of biomolecules is greatly enhanced as the biomolecules are observed in their natural aqueous medium. The potentiostatic control requires that the liquid contains electrolytes. The electrolytes would normally cause Faradaic or capacitive currents at the tip and thereby introduce noise in the measurements. Suppresion of Faradaic processes is essential. It is accomplished both by the double potentiostatic control and by coating the tip with non-conducting polymers (wax, nail polish, electro paint). Only the outermost area near the end of the tip is left uncoated. The area should be less than 1 $\mu m^2$ giving a Faradaic tip current of 0.1 nA [Danilov,95].

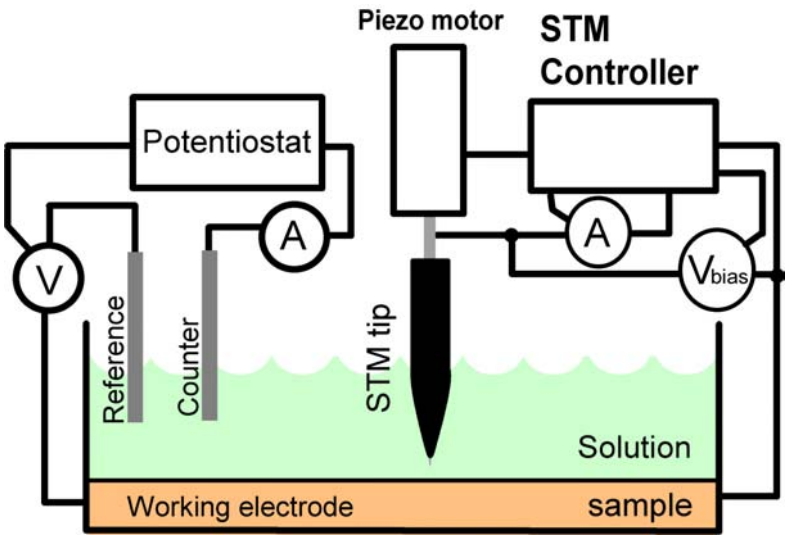


**Figure 3.2**: STM configuration for *in situ* STM

IMAGE FILTRATION

It is virtually impossible to level the substrate 100 % relative to the x-y-direction of the scanner. Unfiltered images of unlevelled substrates would therefore appear strongly tilted, thus conceiling details about molecular adsorbates and terrace steps. All images are thus per default levelled relative to the plane that best fits the data. This means, however, that in an image containing several terraces (atomically planar areas) the terraces will appear tilted. This filtration process is shown schematically in Fig. 3.3A+B for lines. The expansion to two-dimensional planes should be straight-forward. Another option is to level the data manually by selecting an area (a terrace) as reference (Fig. 3.3C). Images filtered after the scheme in Fig. 3.3B and Fig. 3.3C are also shown.

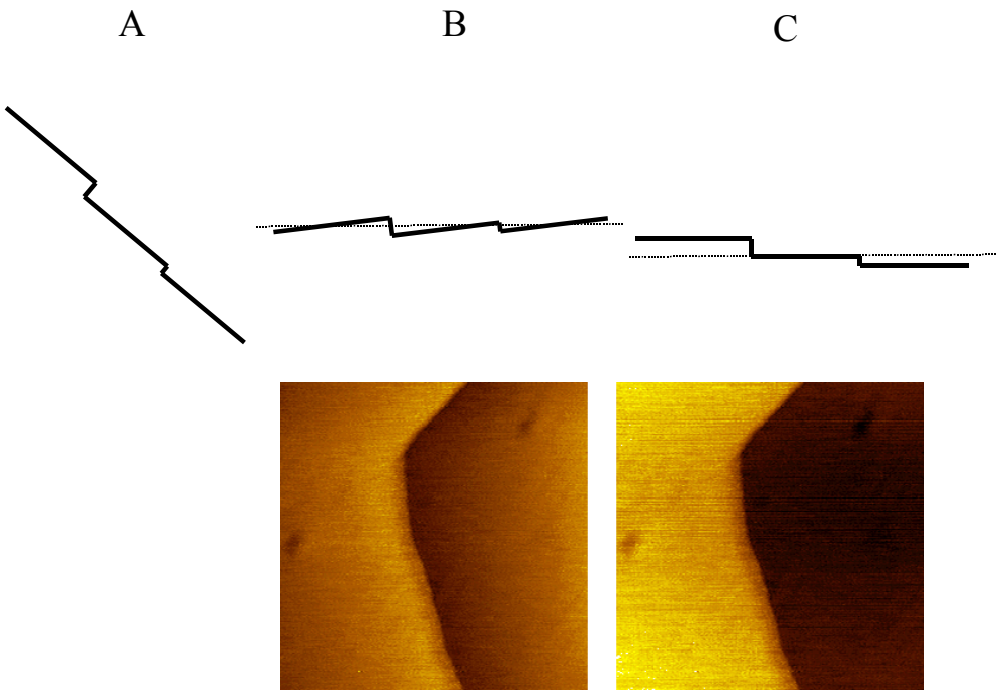


**Figure 3.3**: A) Unlevelled image, B) image levelled relative to the tilt of the entire image, C) image levelled relative to a terrace. Below B and C are *in situ* STM images filtered correspondingly

IMAGE ANALYSIS

The images and spots in images representing adsorbates were analysed with the programme SPIP (Scanning Probe Image Processor, Image Metrology ApS). The 'Grain Analysis' function of the programme calculates the number and dimensions of spots in images. Spots are recognised by being brighter than the background, i.e. by having a higher apparent height. A noisy image will cause problems to distinguish clearly between background and spots. Two main parameters are used in the detection of spots: Detection Level is the apparent height that each pixel in a spot needs to have before being counted as part of a spot. The detection level used in this work is 0.05 nm. The second important parameter is the Minimum Width, which allows you to deselect spots that protrude above the value set by Detection Level but are too small to be proteins. The Minimum Width used in this work is 1.0 nm, which should be sufficiently for detection of individual cytochrome c molecules given its average diameter of 3.5 nm [Louie,90].

## 3.2 Introduction to STM of metalloproteins

### 3.2.1 STM of cytochromes

STM studies of cytochrome *c* have relied on a number of strategies to immobilize cytochrome *c* (cyt *c*) on substrates. The immobilization strategies will be reviewed for both the *ex situ* and *in situ* mode.

*Ex situ* STM of cyt *c*

Highly Oriented Pyrolytic Graphite (HOPG) is a substrate that is often used for STM because it is atomically flat and easy to prepare. The basal plane of HOPG can be lifted off by Scotch Tape revealing a fresh surface. Electro-oxidation of the basal plane HOPG creates functionalities at the carbon atoms such as –OH and –COOH groups [Regisser,96]. The surface thus changes from hydrophobic to hydrofilic.

Horse heart cyt *c* (HHCC) has been immobilized at electro-oxidized HOPG by placing droplets of HHCC solution at HOPG, allowing HHCC to adsorb, wash with

water, and dry [Zhang,96B]. The adsorption most probably occurs via the amide function of the many lysine residues in HHCC, that can bind covalently to the carboxylic functionalities on the electro-oxidized HOPG. Adsorbing highly concentrated HHCC solutions (0.5 mg/ml) produced molecular aggregates of 15-80 nm in diameter and less frequently single molecules (structures of 2.8-4.5 nm in diameter). The ratio of single molecules to molecular aggregates could be increased by using lower concentrations (0.1 mg/ml). The drying time also affected the shape of the molecules. Short drying time retained the globular structures of HHCC, while prolonged drying period (days) caused elipsoidal and even horseshoe-shaped structures. While the lateral extension agreed reasonably with the expected values, the apparent height is only 1.1 nm which is much less than the physical extension due to the low conductivity of HHCC (and proteins in general).

HHCC has also been immobilized on HOPG using the Langmuir-Blodgett technique. HHCC was solubilized in water bubbles in a microemulsion of surfactant molecules in hexane. The protein/surfactant layer was transferred to HOPG at a surface pressure of 20 mN/m. Individual molecules of diameter 3.5 nm could be observed at 0.2 nA tunnel current and moderate bias 0.2 V [Khomutov,02]. The aim of the experiment was to study the current in a double barrier tunnel junction. Peaks in the I-V curves revealed the existence of single-electron transfer in the two junctions (graphite-HHCC and HHCC-STM tip). The peaks were, however, variable in widths and heights and were dependant on the position of the tip above HHCC. Interplay between Coulomb charging effects, the discreteness of the electronic spectrum of HHCC, and electron path effects was believed to cause the peaks.

Mixed monolayers of SAMs have been applied to create preferential adsorption of cyt *c*. HHCC is highly charged (+9) and has a hydrophilic surface. HHCC therefore adsorbs preferentially on hydrophilic SAMs. Mixed monolayers of 3-mercaptopropionic acid (MPA) and 1-hexadecanethiol (HDT) on Au(111) created a monolayer consisting of ’adsorption pits’ of MPA that were 0.5 nm lower in apparent height than HDT domains [Hobara,02]. Adsorption of HHCC onto the MPA domains produced spots of 5.3 nm in diameter and an apparent height of 1.6 nm versus the MPA domain. The redox potential of HHCC at these monolayers was 31 mV vs. SCE strongly indicative of fully functionable protein. The coverage of HHCC increased with increasing ratio of

MPA to HDT. The coverage of HHCC did not increase, however, when the monolayers contained more than 80 % MPA and actually decreased at 100 % MPA. The maximum HHCC coverage obtained at 80 % MPA was $1\times10^{-11}$ mol $cm^{-2}$ or app. 60 % of a monolayer.

Mixed monolayers with functionalized domains protruding from hydrophobic domains were also used to bind HHCC. The terminal groups of the functionalized domains were imidazole, pyridine, nitrile, and carboxylate. In a mixed monolayer of 1-(12-mercaptododecyl)-pyridine (MDDP) and 1-undecanethiol (UDT) on Au(111) the apparent height of the MDDP domains was 1.1 nm relative to UDT domains. Adsorption of HHCC onto the layers gave structures with an area of app. 15 $nm^2$ and an apparent height of 0.8 nm. relative to UDT. The low apparent height is partly due to the adsorption mode of HHCC, which was believed to be binding the pyridine moiety by the heme group. The adsorption pattern was confirmed by measurements of the reduction potential. Functionalized domains with nitrogen ligands such as pyridine, imidazole and nitrile resulted in a significant negative (-300 to –400 mV) shift in reduction potential, indicative of axial nitrogen binding to heme [Wei,02]. Binding to carboxylate functionalized domains did not change the reduction potential of adsorbed HHCC.

*In situ* STM of cytochrome *c*

HHCC was imaged at glassy carbon and polycrystalline gold electrodes with HHCC in solution in millimolar concentrations. Structures resembling individual HHCC molecules were visible between 50 nm structures, which were presumably molecular aggregates [Andersen,95].

*In situ* STM imaging of covalently immobilized HHCC was achieved [Andersen,97]. HHCC was immobilized on polycrystalline Pt by silanisation of the Pt surface and linking of HHCC to a terminal aldehyde group. Clusters of app. 10 nm and even single molecules were observed. Immobilization of HHCC to Au(111) was achieved by a multistep procedure. The first step was adsorption of N-acetylcystein to Au(111). A carbodiimide was subsequently added to the N-acetylcystein layer. Addition of HHCC caused the protein to bind to one of the imide moieties.

Molecular engineering has been used to introduce surface residues into proteins thereby enabling binding of the protein to a substrate [Davis,00B; Djuricic,02]. The experiments were conducted, however, without potentiostatic control of the substrate. Five surface cysteines were removed and one surface cysteine was introduced into cyt $P450_{cam}$. Submolecular features of cyt P450cam were observed on Au(111). In addition the complex of cyt P450cam and the complex with its electron transfer co-factor protein putidaredoxin could be clearly discerned [Djuricic,02].

### 3.2.2 *In situ* STM of other metalloproteins

The small electron transfer protein azurin (type 1 Cu) from *Pseudomonas aeruginosa* was studied by *in situ* STM. Azurin was immobilized in either of two immobilization schemes 1) via a disulfide bridge anchoring directly on a Au(111) substrate [Chi,00] or 2) via hydrophobic interaction of the residues surrounding the redoxactive Cu ion with a Self-Assembled Monolayer of alkylthiolates [Chi,01]. As the disulfide bridge and the Cu ion are located in each end of azurin electron transfer through azurin could be observed in opposite directions. Interestingly immobilization scheme 1) provided molecular resolution of fully functionable azurin with a high coverage of 70% [Chi,00]. Immobilization scheme 2) also provided molecular resolution showing areas of both well-ordered alkylthiolate layers and azurin adlayers. Scheme 2 was investigated for different chain length of alkyl thiolates. Constant electrochemical electron transfer rates were observed for alkylthiols shorter than ten methylene units. The ET rate decayed exponentially for longer alkylthiolate layer. In a later study recombinant azurin was shown to exhibit identical electrochemical behaviour [Fristrup,01].

## 3.3 Experimental procedure

STM INSTRUMENT

A PicoSPM instrument (Molecular Imaging Co., USA) was used for *in situ* STM. A 1 μM scanner was used and images were recorded in constant current mode.

TIPS

Tungsten tips were used in all images shown in this thesis. Tungsten tips are well suited for STM because the fabrication of sharp tips is easy. The tips are electrochemically etched from 20 mm pieces of tungsten (wire diameter 0.25 mm, Dansk-Hollandsk Ædelmetal A/S). The tungsten wire is suspended above a 1 M solution of KOH in millipore water and connected to a voltage supply. Approximately 1 mm of the wire is immersed in the solution. A coiled platinum wire serves as a counter electrode. A 10 V AC voltage is applied. Tungsten is oxidized to tungstate ions at the air-liquid interface. Gas evolution is observed at both electrodes. Bubbles of gas are ejected from the tungsten wire. The velocity of these bubbles depends on the KOH concentration and the AC voltage. The capillary forces of the aqueous etching solution will force the solution to form a ’meniscus’ around the tip. The height of this ’meniscus’ decreases as the diameter of the wire is decreased, thus the air-liquid interface is moved slowly down the tip during etching, leading to increasingly smaller diameters along the tip. Finally when the radius is very small, the solution ’meniscus’ will loose contact to the tip and a sharp tip is produced. The tip is washed in plenty of millipore water.

An often encountered problem is $CO_2$ that dissolves in the etching solution. This will make the bubbles considerably larger and disturb the air-liquid interface. Due to the disturbance the solution will fall from the tip when the tip radius is still large resulting in a blunt tip.

The tips are coated with Apiezon wax to insulate them and prevent Faradaic currents during scanning. The tip is placed in a metal cup containing heated liquid Apiezon wax. The cup is heated electrically. The blunt end of the tip is put through a hole in the bottom of the cup and fixed vertically on a vertically translatable support (Fig. 3.4). The wire is moved down so that the tip is just immersed in the wax. The heating is stopped and the wax allowed to cool. The tip is emersed from the wax when the wax has solidified sufficiently. The tip coating is observed through a magnifying lens. After coating excess wax is scraped off with a scalpel. Only the outermost 5 mm is left in order for the tip to fit in the scanner head.

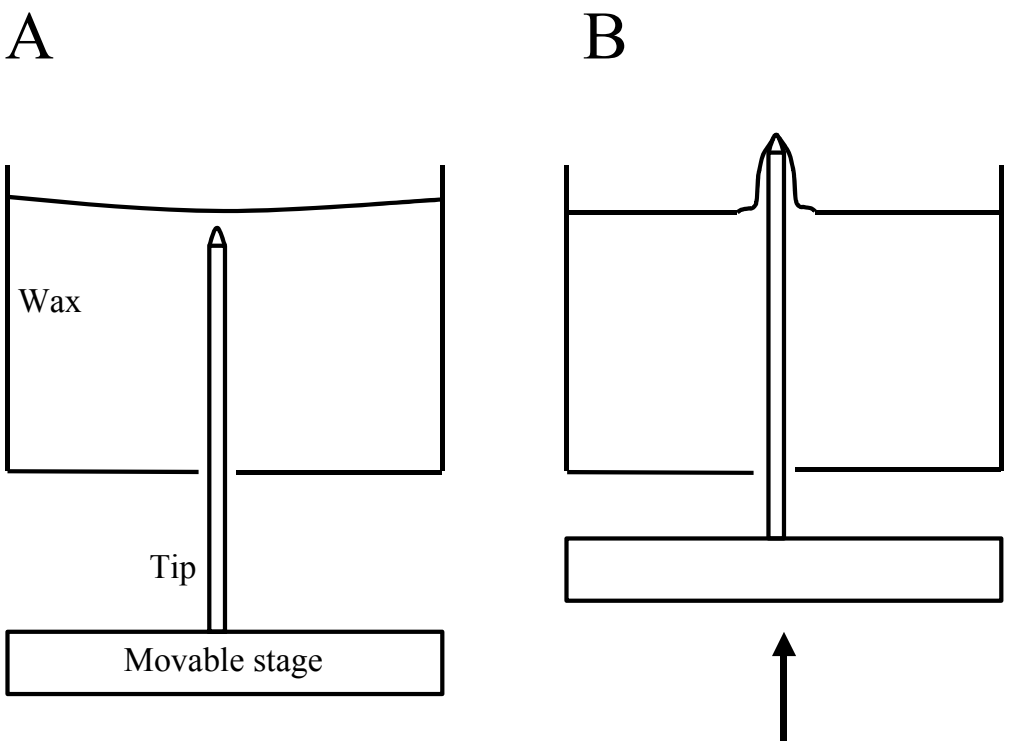


**Figure 3.4**: Schematical view of the tip coating set up. A) The tip is immersed in the Apiezon wax when the wax is liquid. B) The tip is slowly emersed when the wax starts to harden (≈85°C).

ULTRAPURE CONDITIONS

In order to obtain high quality STM images everything in contact with the sample should be clean. Hence not only the sample but also the electrolyte solution and everything in contact with it. Metallic substances such as gold substrates are cleaned by flame annealing. Glassware and plastic materials (Teflon/KEL-F) are cleaned by boiling in 15 % nitric acid and cleaned by copious amounts of millipore water.

SAMPLE

The samples used are single-crystal Au(111) disk electrodes, diameter 10 mm, thickness 1 mm (MaTeck GmbH, Surface Preparation Laboratory). The alignment of the disk electrode is within 0.1° of the (111)-direction.

## SAMPLE PREPARATION

The Au(111) disk electrode is electropolished before each experiment. The electrode is immersed as anode in a 0.05 M solution of $H_2SO_4$ (pro analysi). A flame annealed platinum wire acts as cathode. 10 V DC is supplied for 1-2 minutes. The resulting red oxide is removed by immersing the working electrode in a 1 M solution of hydrochloric acid (pro analysi). The electrode is subsequently washed in MilliQ water and annealed in an oven for 4-10 hours at 850°C. The heating treatment induces large terraces on the sample, i.e. atomically planar over several hundred nm. The disk electrode is flame annealed for 2-5 minutes before soaking to remove any dirt particles, then allowed to cool for approximately one minute before being immersed in a YCC solution. Soaking times between one hour and three days at room temperatures have been used. Three hours was, however, the standard.

## PROTEIN PURIFICATION

YCC and HHCC (96% pure from Sigma) were purified by High Performance Liquid Chromatography using a 16/10 Sepharose High Performance Gel. YCC was eluted at a conductivity of 49 $mScm^{-1}$ using a NaCl gradient in 5 mM MES (2-(N-morpholino)ethanesulfonic acid, Sigma) buffer, pH 6.0. The protein solution was transferred to 10 mM phosphate buffer, pH 7 by ultrafiltration and small portions stored at -18°C. Solutions used for soaking gold substrates were kept at 4°C and re-used but only for 14 days. HHCC was not used for STM but for XPS measurements (chapter 5).

The concentrations used were 25 and 50 μM and pH was 7.0-7.5. The concentration was determined spectrophotometrically by using the absorptivities at 550 nm: $\varepsilon_{550}$ = 0.029 $cm^{-1}M^{-1}$ [Sherman,65] for YCC and $\varepsilon_{550}$ = 0.0277 $cm^{-1}M^{-1}$ [Margoliash,59] for HHCC.

## LIQUID CELL

The sample and the electrolyte solution is housed in an liquid cell made from KEL-F, which is partly defluorinated teflon (PTFE). A Teflon-capped O-ring is interfaced between the disk electrode and the KEL-F cell (Fig. 3.5). The liquid is equipped with two Pt wires, which act as reference and counter electrode, respectively.

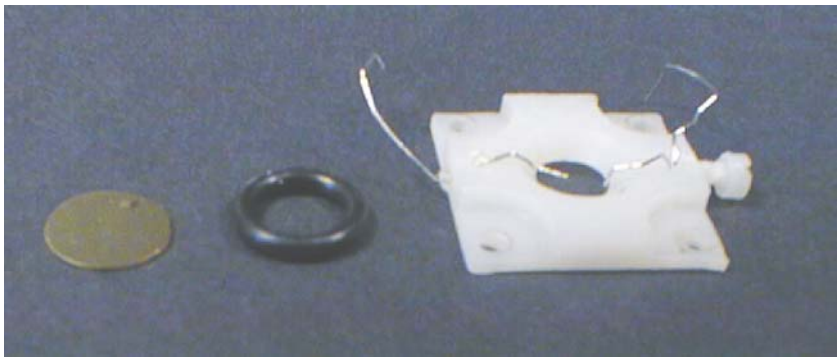

**Figure 3.5**: The gold single-crystal together with the O-ring and STM cell used in the experiments. The gold crystal is placed on a base, the O-ring on the crystal and on the top, the cell. The cell is attached to the base via four screws. The metallic wires attached to the cell are Pt wires used as counter and reference electrodes.

POTENTIOSTATIC CONTROL DURING ASSEMBLY

The sample is kept under potentiostastic control during the introduction of electrolyte solution to avoid lifting the gold reconstruction, which would damage any adsorbed layer.

## 3.4 STM of yeast cytochrome *c*

YCC was chosen as a target of this STM study because it is a small redox protein, which has not been studied by STM before. Redox molecules have the perspective that resonance tunnelling can occur around the redox potential and give rise to changes in the apparent height above the redox active part. Other small redox proteins to have been studied by *in situ* STM, are azurin [Chi,00] and HHCC [Andersen,95; Andersen,97].

As noted YCC contains a Cys102 near the surface, which is likely to adsorb to gold. Immobilization of target molecules is essential in all STM investigations. For this reason YCC was thought to be well suited for STM study. Secondly it is a goal of this STM investigation to study the potential stability range.

Fig. 3.6 shows a representative STM image of YCC adsorbed on Au(111). The image is obtained at a substrate potential of –0.16 V vs. SCE, bias voltage –0.2 V, tunneling current 0.5 nA.

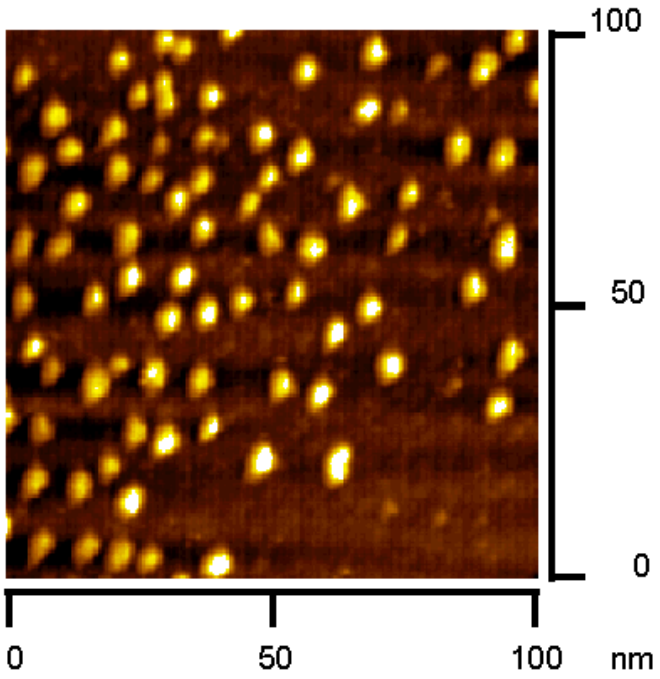


**Figure 3.6**: STM image of YCC at Au(111). Substrate potential –0.16 V (SCE). Bias voltage –0.2 V. Tip current 1.0 nA. Electrolyte: 10 mM $KH_2PO_4/K_2HPO_4$, pH 7.5. Soaked in 25 µM YCC, 10 mM $KH_2PO_4/K_2HPO_4$, pH 7.5 for 6 hours at room temperature.

The image was analyzed by SPIP (Table 3.1). The analysis shows that the spots have an average area 20-22 $nm^2$ diameter (mean area) and 2.4 Å apparent height (mean maximum height). The area accord well with the crystallographic size of YCC [Louie,90], whereas the height differs considerably. This is understandable, however, since the contrast (tunneling current) depends on the media between the tip and substrate. STM would only yield the true physical height if the conductivity of YCC was equal to the conductivity of the surrounding aqueous phosphate buffer solution. The low conductivity of YCC is reflected by a low apparent height one tenth of its bulk value. The analysis data for a series of STM images obtained under the same conditions are also given in table 3.1. Average height of one spot is the average z-value of each

pixel belonging to that spot. Mean average height is the mean of the average height of all spots in one image. The average height can be used as a quantitative measure for the shape of a spot. For instance the average height of a perfect sphere would be one sixth of the maximum height.

**Table 3.1**: SPIP Analysis of a series of images including Fig. 3.6 of the same area. The row time is a relative time scale showing when the images were recorded. Coverage indicates the percentage of the image, that is more than 0.05 nm in apparent height relative to the gold surface. Only structures larger than 1 nm are counted.

| Time (min.) | 0 | 2 | 5 | 7 | 9 | 11 |
|---|---|---|---|---|---|---|
| Coverage (%) | 18 | 17 | 17 | 17 | 17 | 17 |
| Grains pr. $\mu m^2$ | 8700 | 7800 | 8000 | 8000 | 7800 | 7900 |
| Mean area ($nm^2$) | 20 | 21 | 21 | 21 | 22 | 21 |
| Mean average height (nm) | 0.11 | 0.12 | 0.12 | 0.12 | 0.13 | 0.11 |
| Mean maximum height (nm) | 0.24 | 0.25 | 0.24 | 0.23 | 0.25 | 0.22 |

The crystallographic diameter of YCC is 3.5-4.0 nm [Louie,90], which would correspond to an area of 10-13 $nm^2$. The discrepancy is most likely due to tip convolution. The low apparent height is due to the low conductivity of YCC (and other biomolecules). The tip has to move closer to the substrate in order to obtain the same current. The proximity of the tip to the adsorbate might also cause deformation of the adsorbate, thereby further decreasing the height as observed for the C60 molecule [Sautet,97]. The coverage is approximately 18 %, which might seem low in the light of the strong sulfur-gold interaction. Cys102 is, however, somewhat buried in the protein structure and adsorption needs some conformational pre-organisation. Increased adsorption time might also increase the coverage. The image in Fig. 3.7 is obtained after the electrode was soaked for 65 hours in YCC solution at room temperature.

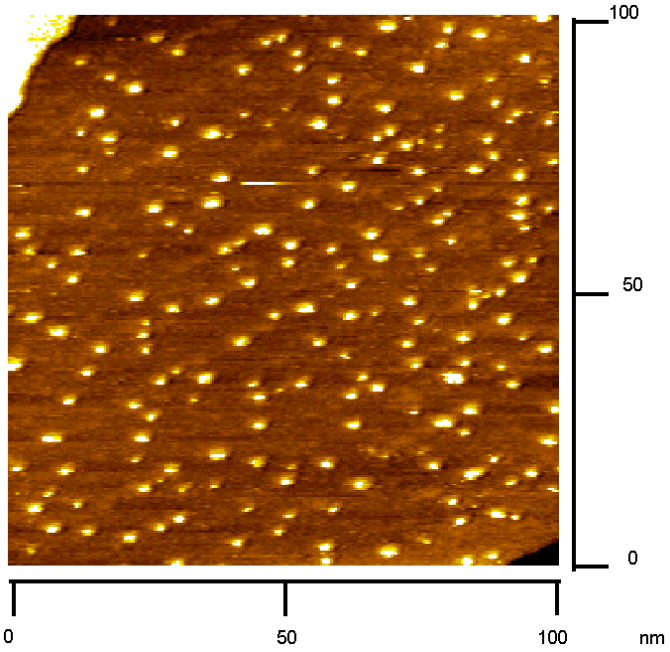


**Figure 3.7**: STM image of YCC at Au(111). Substrate potential –0.44 V (SCE). Bias voltage –0.1 V. Tip current 0.5 nA. Electrolyte: 10 mM $KH_2PO_4/K_2HPO_4$, pH 7.0. Soaked in 50 µM YCC, 10 mM $KH_2PO_4/K_2HPO_4$, pH 7.5 for 65 hours at room temperature.

A SPIP analysis of the spots in Fig. 3.7 is given in Table 3.2.

**Table 3.2**: SPIP Analysis of a series of images including Fig. 3.7 of the same area.

| | |
|---|---|
| Coverage (%) | 10 |
| Grains pr. $\mu m^2$ | 18000 |
| Mean area ($nm^2$) | 5.4 |
| Mean average height (nm) | 0.07 |
| Mean maximum height (nm) | 0.20 |

The analysis shows that the coverage, interpreted as the number of spots, has increased from 8000 to 18000 molecules pr. $\mu m^2$. The mean area has, however,

decreased to only 5.4 $nm^2$. In addition the mean average apparent height has decreased to 60 % of the value for short adsorption times. There is less change in the mean maximum height: from 0.24 to 0.20 nm. This means that more contrast is lost near the edges of the protein and less at the centre. Cytochrome *c* is considered a stable protein, but these features could be a result of unfolding caused by the long adsorption time.

Soaking was tried at a lower temperature (+4°C) to avoid denaturation of YCC, but even soaking times of three days provided no structures on Au(111), as observed by *in situ* STM. The elevated temperature, i.e. room temperature, is obviously a prerequisite for adsorption of YCC on Au in order to rearrange the protein to expose Cys102 to the gold surface.

Soaking was also tried at 35-40°C, i.e. below the temperature where YCC unfolds, to promote the rearrangement process. These experimental conditions did not provide images with molecular resolution, however.

The contrast of YCC as a function of substrate potential was also investigated. To study electron transfer phenomena of adsorbed molecules it is - from a theoretical point of view - most desirable to keep the bias potential constant, while changing the substrate potential. Hence the tip potential must be changed along with the substrate. In practice a change in the potential of the tungsten tip introduces noise in the image[1]. It is therefore easier to keep the tip potential constant and vary the bias potential but the information is then less clearcut. This was done in the experiment in Fig. 3.8. The sample potential in the first image is –0.36 V (SCE) and the bias voltage –0.05 V. The sample potential was changed in steps of +0.1 V. Two images were recorded at each potential. The coverage is clearly seen to decrease. The question is if the desorption is caused by the potential change, by tip interaction or by using too high bias voltages. From Fig. 3.6 it is learnt that the molecules are stable at the surface at –0.16 V. Likewise a tip current of 1.0 nA will not move the tip too close to the molecule, causing desorption. Tip currents of up to 10 nA could be used without significant desorption of YCC. In the experiment in Fig. 3.8 the bias voltage is increased, which will actually increase the distance between tip and substrate. Hence the interaction should decrease in time. The most likely

[1] The noise is presumably due to oxidation of tungsten thereby causing Faradaic currents. Pt/Ir tips are in this respect a better material since they have a higher oxidation potential.

explanation is that the potential change destabilises the protein layer and makes it more vulnerable to scanning.

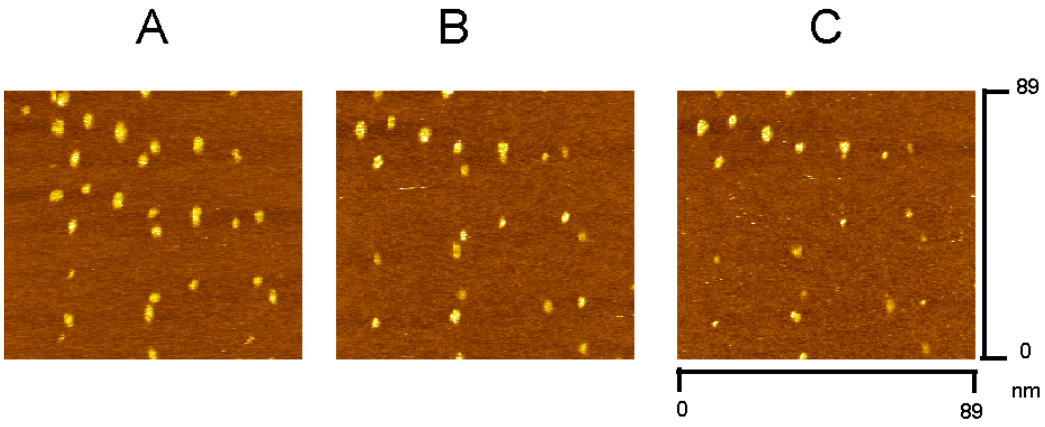


**Figure 3.8**: STM images of YCC at Au(111). Substrate potential A: -0.36 V, B: -0.16 V, C: 0.04 V (SCE). Bias voltage A: -0.05 V, B: -0.25 V, C: –0.45 V. Tip current 1.0 nA. Electrolyte: 10 mM $KH_2PO_4/K_2HPO_4$, pH 7.5. Soaked in 50 µM YCC, 10 mM $KH_2PO_4/K_2HPO_4$, pH 7.5 for 5 hours at room temperature. Image B and C recorded 2.4 and 4.9 minutes after image A.

Table 3.3 contains an analysis of the data in Fig. 3.8. It shows that the contrast of the molecules is the same as in table 3.1. Apart from the lower coverage, it also differs in the average area of the molecules. The area is, however, within what is expected from the crystallographically determined size.

**Table 3.3**: SPIP Analysis of a series of images including Fig. 3.8 of the same area.

| Time (min.) | 0 | 2.4 | 4.9 |
|---|---|---|---|
| Sample potential (V vs. SCE) | -0.36 | -0.16 | 0.04 |
| Coverage (%) | 4.9 | 3.5 | 2.5 |
| Grains pr. $\mu m^2$ | 3400 | 2700 | 2400 |
| Mean area ($nm^2$) | 13 | 12 | 9 |
| Mean average height (nm) | 0.10 | 0.11 | 0.1 |
| Mean maximum height (nm) | 0.23 | 0.25 | 0.25 |

## 3.5 Conclusion

Molecular resolution of YCC on Au(111) by STM was achieved. The immobilization is believed to take place via the free thiol group Cys102 near the surface of YCC. The adsorbed layer was stable towards imaging at tunneling currents up to 10 nA at potentials negative of the redox potential of YCC. The potential stability range was –0.4 $\rightarrow$ -0.1 V (SCE). YCC was however unstable towards potential scanning. Desorption of YCC was observed when the sample potential was changed. The adsorbed YCC layer showed coverages of up to 20 % or $8\times10^{11}$ molecules pr. $cm^2$ when the Au(111) electrode was soaked in a YCC solution for less than six hours at room temperature. Prolonged adsorption time (65 hours at room temperature) could increase the coverage to $18 \times 10^{11}$ molecules pr. $cm^2$. The contrast of YCC decreased considerably, however. For short adsorption times the area of YCC molecules was found to be 13-22 $nm^2$. The discrepancy from the expected value 10-13 $nm^2$ could be explained by tip convolution. For long adsorption times the area was only 5 $nm^2$, presumably due to denaturation of YCC.

# 4 Electrochemistry

## 4.1 Introduction to electrochemical methods

### 4.1.1 Experimental set-up

The electrochemical set-up consists of an Autolab Pgstat 10 potentiostat (EcoChemie) and a home-made electrochemical glass cell (Fig. 4.1). The glass cell is placed in a Faraday cage (Cypress systems) to reduce electronic noise. The glass cell houses three electrodes. The working electrode is a Au(111) bead electrode. The counter electrode is a platinum coil. The reference electrode is either a standard calomel electrode (SCE) or a reversible hydrogen electrode (RHE). The working electrode is operated in the meniscus mode. Hence, only the Au(111) facet is in contact with the solution.

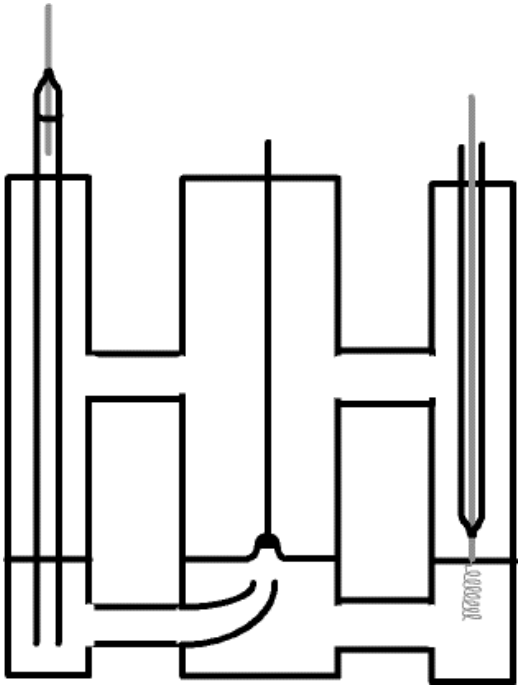

**Figure 4.1**: Sketch of the electrochemical cell showing (left) the Reversible Hydrogen Electrode (RHE), (middle) the working electrode, and (right) the counter electrode.

### 4.1.2 Manufacture of electrodes

Au(111) electrodes

PURIFICATION OF GOLD

Single-crystal Au(111)-electrodes were made from 1.0 mm diameter 99.95% pure gold wire. The gold wire is held by a ceramic tweezer and suspended vertically above a microburner (Micro torch, type 191C, Tanaka Engineering Works, Ltd.), whose nozzle is only 0.5 mm and hence able to supply a narrow, focused flame. The microburner is supplied with hydrogen (99.999 %) and oxygen (99.999%). A bead of gold is formed by melting the lowest part of the gold wire. Preferably the bead should be as large as possible to increase the electrode area. If the bead becomes too large, however, it will fall from the gold wire. The usual maximum diameter of beads is 3 mm.

At this point the bead still contains impurities, which are removed from the bead by repeated cycles of melting and solidifying (Fig. 4.2). The melting is performed by using an approximately 5 mm long flame of hydrogen and oxygen. The hydrogen flame itself is hot enough to melt gold. The flame is, however, not sharply focused. Addition of oxygen will focus the flame, but if too much oxygen is added, the flame will be so hot that the bead melting is uncontrolled. When the bead is heated the impurities appear lighter than the gold. The interface between melted and solid gold – the melt line – is continously moved up and down in the bead by lowering and raising the temperature of the flame, which is controlled by changing the flow of hydrogen. If this operation is performed slowly the impurities will be collected at and transported by the melt line. It is thereby possible to move the impurites up to the base of the bead. The bead is melted 10-15 times. The impurities are further collected on the surface of the bead and can be removed by scraping them off with a clean scalpel after cooling of the bead. They can also be removed by electropolishing (sec. 4.1.3). The melting and scraping procedure is repeated 5 to 8 times, until the amount of impurities is low. The bead should now be a single-crystal of gold. The eight (111) facets are the clearest and largest. The (111) facets are oriented as indicated in Fig. 4.3. It is usually only possible to observe up to seven (111) facets due to the connection between the bead and the wire.

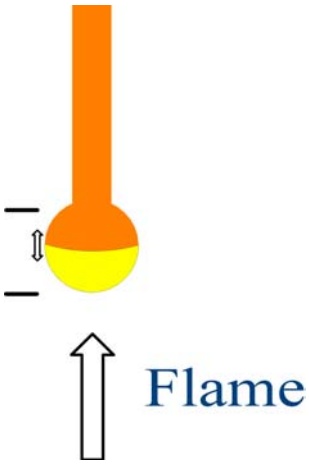


**Figure 4.2**: Sketch of the melting of the bead. Impurities are moved with the melt line to the base of the bead.

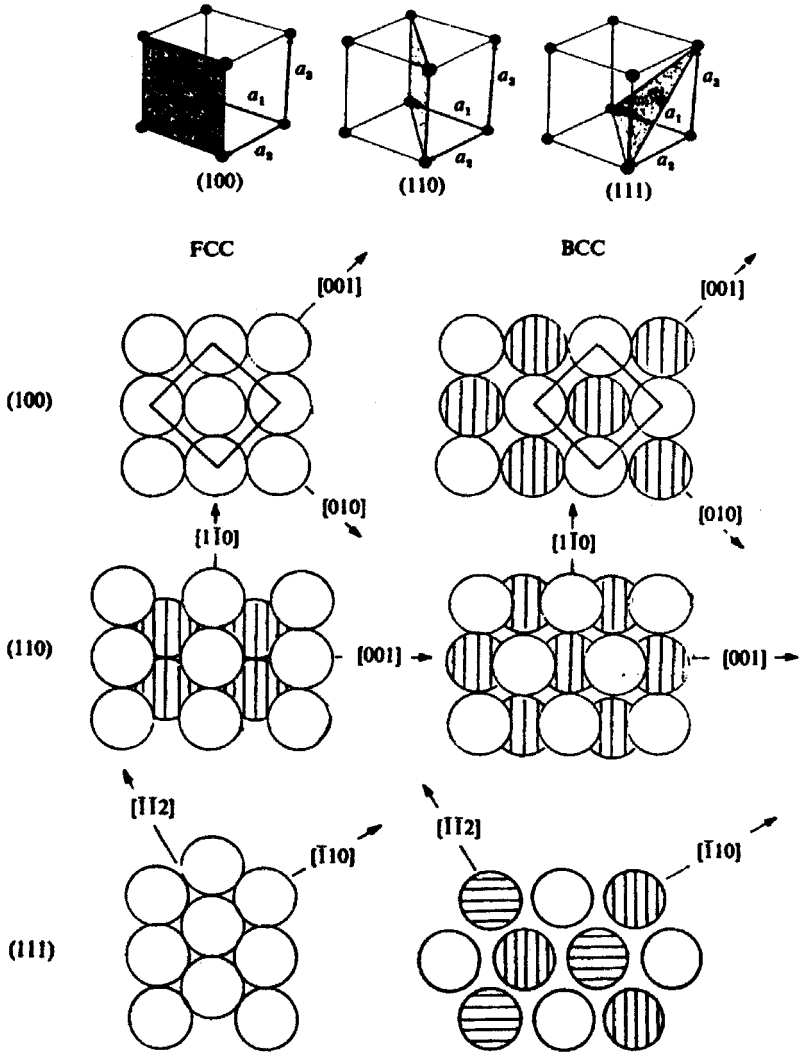


**Figure 4.3**: Schematics of a gold single-crystal showing the crystallographic planes.

ORIENTATION OF THE FACETS

The wire is glued onto the inner of two concentric steel cylinders as shown in Fig. 4.4. Once a (111) facet has been identified it is oriented horizontally by bending the wire. A facet as far away from the base as possible should be chosen, as the bead will be polished down to increase the (111) facet area. The final orientation is achieved as shown in Fig. 4.5. A laser beam is directed to a mirror. The beam is reflected to the facet and back to the mirror and from there to a screen. The distance between the mirror and the screen is approximately 4 m. Rotation of the inner cylinder will cause the laser spot on the screen to move in a circle, if the facet is not oriented completely horizontally. The facet is adjusted until the spot on the screen no longer describes a circle but a point.

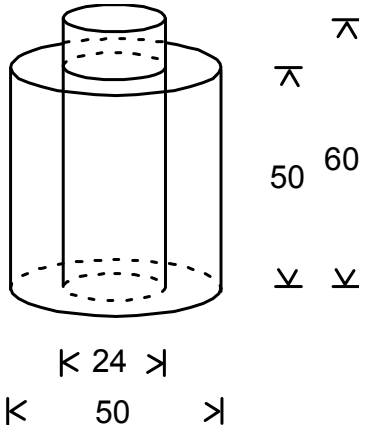


**Figure 4.4**: Two concentric stainless steel cylinders ensure that the facet can be rotated horizontally and in one point.

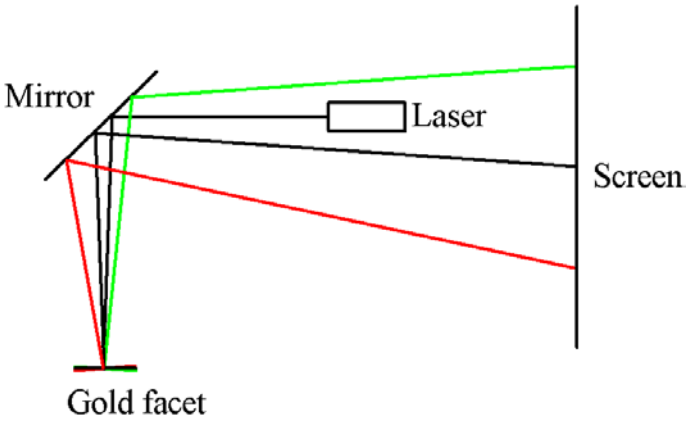


**Figure 4.5**: Sketch of the set-up to orient a Au(111) facet horizontally. The red and green lines describe the reflection from a non-horizontal gold facet.

IMMOBILIZATION OF THE BEAD

The bead is cast in a polymer consisting of

5.2 g nonenylsuccinic anhydride
2.0 g 4-vinylcyclohexenedioxide
1.2 g epoxyresin, diglycidylether of polypropyleneglycol (D.E.R. 736)
0.08 g 2-dimethylaminoethanol

The inner surface of the outer cylinder is coated with vacuum grease and is pulled up so that it covers the bead (Fig. 4.6). The polymer ingredients are mixed and poured over the bead. The mixture is heated at 80 °C in an oven for ten hours.

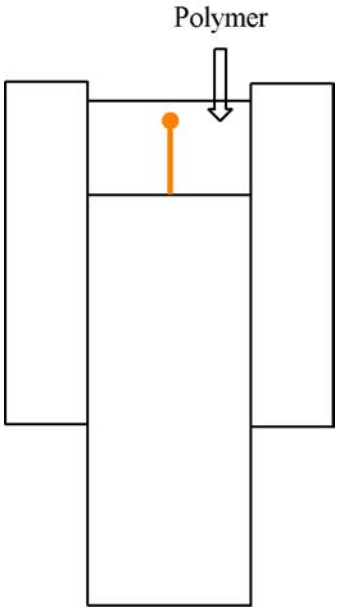


**Figure 4.6**: Schematic view of pouring the polymer mixture on the gold wire.

POLISHING OF THE FACET

The grease is removed by washing with plenty of sulfo and water. Polishing is conducted on a polishing machine as shown in Fig. 4.7. The inner cylinder is rotated inside the outer cylinder in order to get an even polishing in all directions. The bead is first polished by SiC papers of decreasing particle size (7 steps), then by a slurry of $Al_2O_3$. The $Al_2O_3$ particle sizes used are 1.0, 0.1, and 0.05 μm. Care should be taken in the first polishing steps, so that the final polishing steps are performed when the bead has been polished down to maximum area, i.e. halfway through the bead.

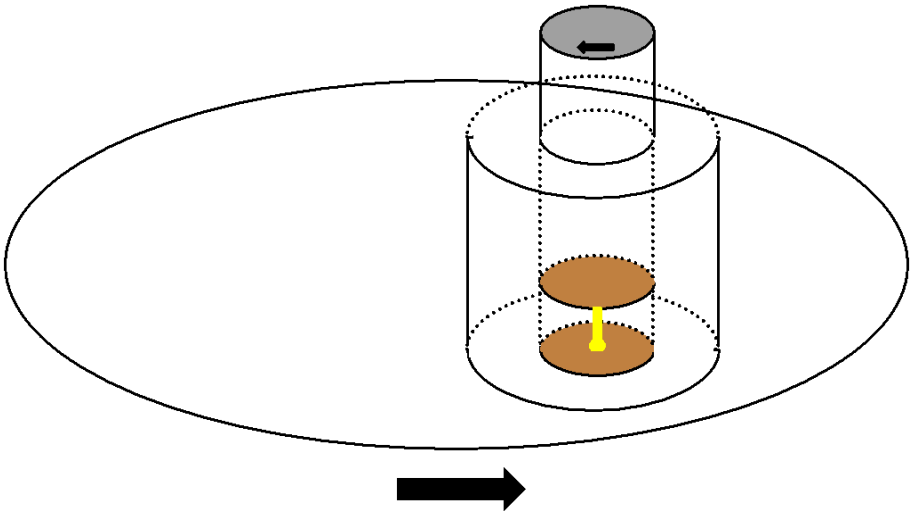

**Figure 4.7**: Schematic view of polishing the facet.

DISSOLUTION OF THE POLYMER

The bead electrode is released by dissolving the polymer and the glue in chloroform. The dissolution takes 2-3 days and it is necessary to change the solution 1-2 times.

Reversible Hydrogen Electrodes (RHE)

Reversible Hydrogen Electrodes (RHE) are made according to the principle shown in Fig. 4.8. A 1.0 mm diameter flame annealed platinum wire is inserted in a clean 10 cm pyrex glass tube and the tube is melted onto the Pt wire by heating it in a hydrogen flame for 5-10 seconds. The heating is performed from several directions to make the tube fit the wire closely. Electrolyte is added to the tube from a cleaned glass pipette, once the tube has cooled down. A stream of hydrogen is bubbled through a solution of electrolyte. The tube is immersed in the solution and hydrogen bubbles are allowed to enter the tube. The hydrogen gas should cover approximately half the Pt wire inside the tube. The potential follows the equation: $E = -59.3\ mV \times pH$ at 25°C.

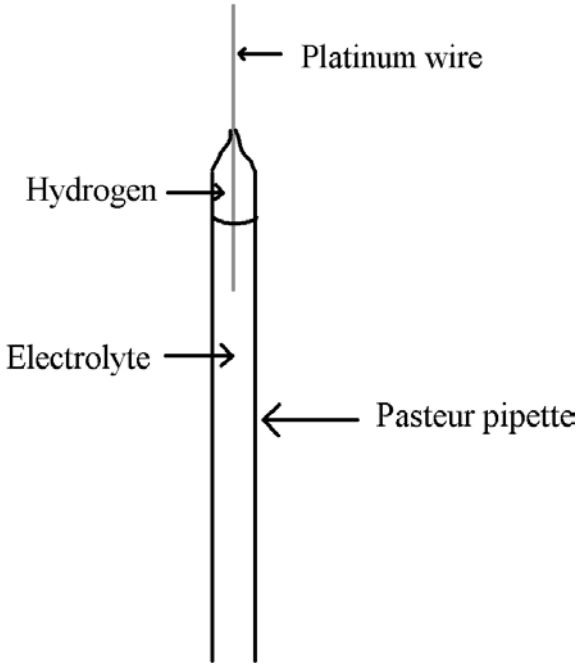


**Figure 4.8**: Schematic view of the Reversible Hydrogen Electrode.

### 4.1.3 Ultrapure conditions

The experiments were conducted under ultrapure conditions. Glassware is cleaned by boiling in 15% nitric acid (pro analysi) and rinsing with MilliQ water. The platinum wire for the counter electrode was annealed in a hydrogen flame and then rinsed in MilliQ water. Chemicals of ultrapure grade are used. The Au(111) working electrode was electropolished before each experiment as described for Au(111) disk electrodes in sec. 3.3. The heating treatment induces large terraces on the sample, i.e. atomically planar over several hundred nm.

### 4.1.4 Removal of oxygen

Oxygen constitutes a major problem in all electrochemical experiments, mainly because it is reduced to water at low potentials. Dioxygen reduction is suppressed by flowing a stream of wetted highly pure (99.999%) argon through the electrolyte solution for at least 30 minutes before the measurement. An overpressure of argon is maintained

above the electrolyte solution during measurement. The argon is guaranteed to contain less than 2 ppm of oxygen. The argon gas is further cleaned by passing through a Chrompack-Gas Clean filter system (Varian). The oxygen concentration at the outlet of this filter is guaranteed 0.05 ppm.

### 4.1.5 Reductive desorption

Recording of reductive desorption (RD) voltammetry is a method often used both as a fingerprint for functionalized alkanethiols and to determine the packing and coverage of sulfur-containing molecules at gold electrodes [Zhang,00; Chi,00]. Alkanethiols and sulfides form Self-Assembled Monolayers (SAMs) on gold and other soft metals via gold-thiolate bond formation. The nature of the gold-thiolate bond has been extensively investigated. Some investigations suggest that the bond is purely ionic with one positive charge on gold and one negative charge on sulfur. Surface IR and Raman spectra have shown that S is not bonded to H when adsorbed on gold [Finklea,96]. Also XPS has shown that equivalent alkanethiols and disulfides yield the same chemical species upon adsorption suggesting that a thiolate is formed after adsorption.

Other investigations suggest that the gold-sulfur bond is polar. Contact potential differences with alkanethiol SAMs of different chain lengths implied that about one sixth of an electronic charge is located on sulfur [Finklea,96]. Ab initio calculations of the bond between S-H or S-$CH_3$ and gold showed that 40-70% of an electronic charge is located on sulfur [Finklea,96].

SAMs of long chain alkanethiols are highly organised presumably due to van der Waals interaction between the alkane chains [Walczak,95; Berger,97A]. Each molecule occupy a $(\sqrt{3}\times\sqrt{3})R30°$ unit cell on Au(111) where the chains are tilted 30° relative to the surface normal [Dannenberger,99]. SAMs of short chain thiols tend to be more disorganised and less stable [Finklea,96].

According to reaction scheme (4.1)

$$Au|SC_nX + e^- + M^+ \rightarrow Au^0 + XC_nS^- + M^+ \qquad (4.1)$$

the adsorbed sulfur molecule is desorbed by reduction to a thiolate and liberation of the thiol into the solution. $M^+$ denotes a cation as the peak potential depends on the nature of the cation [Finklea,96]. RD is mostly conducted in alkaline solutions to avoid interference from electrochemical dihydrogen evolution. Dihydrogen evolution is shifted to a lower potential at high pH and hence does not interfere with the desorption of the sulfur molecule [Yang,96].

The RD potential is in the range –0.7 to –1.4 vs. Ag/AgCl [Finklea,96]. In accord with the greater stability of long chain thiol SAMs the RD potential decreases with increasing chain length [Widrig,91].

The RD potential is also sensitive to pH. The peak potential for mercaptononane is thus shifted positively at pH<5.9 [Yang,96] but is nearly constant above pH 5.9. The shape of the peak is changed, however. The peak width is reduced at increased pH, reflecting a faster reduction reaction. Despite the change in peak shape and potential the RD peak contains the same amount of charge (90 $\mu Ccm^{-2}$). Thus RD can be used to determine the coverage above pH 5.9, if the peak is not hidden by $H_2$ evolution.

The RD potential of alkanethiols SAMs can be changed by functionalizing the alkanethiol. Carboxylic acid terminated alkanethiol SAMs exhibit a RD potential 110 mV more positive than for non-functionalized SAMs [Imabayashi,97]. The positive shift of carboxylic acid terminated SAMs is ascribed to electrostatic interaction between the charged groups. The introduction of a charged group in the SAMs also increases the solubility of the desorption product. Charged species generally have a higher solubility in aqueous solution than neutral species.

A special case of functionalized thiols are the amino acids cysteine and methionine, which are also interesting in the context of protein monolayers on gold. Cysteine shows a desorption/adsorption signal at –0.4 V vs. SCE at pH 3 [Dakkouri,96]. The peak is shifted to –0.7 V in alkaline solutions (pH 13) [Zhang,00]. The peak area is also lower than for alkanethiols due to the presence of bulky functional side groups (-$NH_2$ and -COOH). At the same time the highly polar nature of these groups induce an entirely different order of the surface layer, due to extensive lateral electrostatic and hydrogen bond networks. Zhang et al. have reported a $(3\sqrt{3}\times6)R30°$ network of clusters with six cysteine molecules on Au(111) in ammonium acetate buffer, pH 4.6, while Dakkouri et al. reported a $(\sqrt{3}\times\sqrt{3})R30°$ structure on Au(111) in 0.1 M $KClO_4$, pH 3. While STM is

able to provide molecular or near-molecular resolution of adsorbed molecular layers the final elucidation of adsorption pattern should be supported by electrochemical determination of the coverage. For instance the cysteine clusters in [Zhang,00] could not readily be identified as six cysteine molecules without support from electrochemistry. The adsorption dynamics of cysteine is referred to in section 2.5 in the context of the microcantilever approach to adsorption of –SH-containing biomolecules and -macromolecules.

### 4.1.6 Differential Pulse Voltammetry

An inherent problem in protein electrochemistry is the low electrode surface coverage of protein compared to smaller molecules. Low coverage means low currents. Normal linear sweep voltammetry is often too insensitive to measure these small electrochemical signals. Differential Pulse Voltammetry (DPV) is a more sensitive method which exploits the differential signal after imposing a small potential pulse in an otherwise linear potential scan. The DPV scheme is shown in Fig. 4.9.

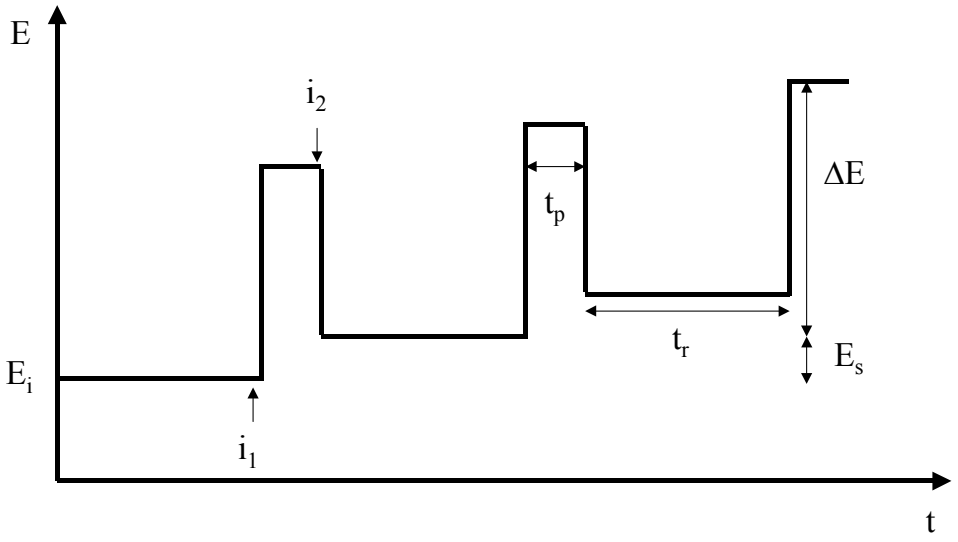


**Figure 4.9**: Applied potential as a function of time in DPV.

The potential is swept linearly with time but interrupted with pulses of a given size $\Delta E$. The current is measured immediately before the beginning of each pulse ($i_1$) and immediately before the end of each pulse ($i_2$). The output is the difference between these two currents, i.e. the differential signal. The pulse height $\Delta E$ is typically up to 25 mV, the duration of the pulse, $t_p$, typically 7 ms, while the time between the pulses, $t_r$, is 0.4 s, i.e. a ratio of 50-60. The step potential is $E_s$. During the pulse the driving force of an electrochemical reaction is increased, which leads to a higher current than in linear sweep methods. Because of the short duration of the pulse an adsorbed adlayer is relatively unaffected by the pulse. The pulse method therefore suppresses capacitive currents leaving pure Faradaic currents [Bard,80]. When the current peak is no longer convoluted with a capacitive current, the properties of the peak (peak potential, current, width) emerge more clearly, hence the method is more precise.

DPV has the disadvantage that integration of a current peak does not directly reflect the charge transferred in the peak. DPV is used mainly for detection of analytes in solution, i.e. diffusion mode [Saterlay,99]. Several theoretical models exist for diffusion mode DPV [Aoki,84; Melville,01] but none deals with the special case of monolayer DPV. Appendix C provides a model for monolayer DPV, which is valid for $t_p >> t_r$ and $\Delta E$ sufficiently low. The current integrated with respect to potential, I, will then be given by

$$I = Q \cdot \pi \frac{k_0 \Delta E}{v} \tag{4.2}$$

where Q is the charge transferred, $k_0$ the electron transfer rate constant, $\Delta E$ the pulse height, and v the scan rate. As electron transfer rate constant often are in the range 0.01-100 $s^{-1}$ the proportionality factor between I and Q can be unity. Under the conditions used in this work ($\Delta E$=25 mV, v=10mV$s^{-1}$) an electron transfer rate constant of 0.13 $s^{-1}$ would make I and Q equal.

Capacitance

The interface between an electrode and an electrolyte resembles a parallel-plate capacitor. Electrochemical capacitors do not, however, function as ideal capacitors, as known from electronics. A capacitor is able to accumulate charge when a potential is applied. The ratio between the accumulated charge, q, and the potential, E, is defined as the capacitance, C. Ideal capacitors have the same capacitance at all potentials, but the capacitance of electrodes depends highly on the material present at the interface.

Electrodes in aqueous solutions often behave as ideal capacitors in a certain potential range, named the double layer potential region. In this region a layer of electrostatically aligned water molecules constitutes an inner capacitor. This layer is termed the inner Helmholtz layer. The second layer – the outer Helmholtz layer - is occupied by hydrated electrolyte ions. Thirdly a diffuse layer of increasingly more bulklike hydrated ions is present. It has been shown that the diffuse layer capacitance at small concentrations is independent of the nature of the ions. In this model the capacitance pr. area, C, can be calculated as [Bockris,70]

$$\frac{1}{C} = \frac{4\pi 2r_W}{\varepsilon_L} + \frac{4\pi}{\varepsilon_H}\sqrt{3}r_W + \frac{4\pi}{\varepsilon_H}r_i + \frac{4\pi}{\varepsilon_s}\kappa \qquad (4.3)$$

where $r_W$ and $r_i$ denote the radii of the water molecules and the hydrated ions, respectively. $\varepsilon_{L \text{ and}}$ $\varepsilon_H$ denote the dielectric constant for the inner and outer layer, respectively. The value of $\varepsilon_L$ in the layer of aligned water molecules is $\cong$ 6. The dielectric constant of the less aligned water molecules surrounding the ions in the outer layer, $\varepsilon_{H,}$ resembles more that of bulk water, hence around 40 [Bockris,70]. The fourth term accounts for the contribution to the capacitance from the diffuse layer, where $\kappa$ denotes the Debye-Hückel screening radius and $\varepsilon_s$ is the static dielectric constant in the diffuse layer. The first term containing $\varepsilon_L$ in the denominator is relatively large. The third term, which contains a high value for $\varepsilon_H$ in the denominator, is relatively small. Thus, the third term containing the radius of the hydrated ions becomes relatively unimportant. The high value of $\varepsilon_s$ (approaching the bulk value of 78) makes the fourth term small, thus the capacitance in the double layer region is mainly governed by the capacitance of the inner Helmholtz layer. For a wide range of ions including phosphate

ions the capacitance is 16-17 $\mu Fcm^{-2}$ in the double layer region. For most ions the double layer capacitance is in the range 15-30 $\mu Fcm^{-2}$. The double layer structure is destroyed when ions adsorb directly on the electrode, i.e. contact-adsorption. This happens at sufficiently positive potentials for anions. The double layer will in fact turn into a triple layer. The contact-adsorbed ions will undoubtedly change the ability of the electrode interface to accumulate charge and hence the capacity. An expression for the capacitance in the case of contact adsorbed ions is

$$\frac{1}{C} = \frac{1}{K_{M\rightarrow OHP}} - \left(\frac{1}{K_{M\rightarrow OHP}} - \frac{1}{K_{M\rightarrow OHP}}\right)\frac{dq_{ca}}{dq_M} \tag{4.4}$$

where K denotes the integral capacitances, $q_{ca}$ is charge density of contact-adsorbed ions and $q_M$ is the charge density of electrode charge. The equation reduces into constant capacitance when the amount of contact-adsorbed ions is zero, e.g. constant. An increase in $q_{ca}$ will result in an increase of C. The increase will not continue, however, with increasing $q_M$, as the contact-adsorbed ions will start to repel each other limiting the increase of $q_{ca}$ with $q_M$. The adsorption will thus result in a peak in the capacitance, known as the 'capacitance-hump' [Bockris,70].

Organic material is characterised by a low dielectric constant. Adsorption of organic molecules such as proteins will result in a lowered capacitance according to (4.3). A low capacitance constitutes a fingerprint of adsorption of large organic molecules.

Capacitance measurements explore the changes in capacitance due to adsorption and desorption of molecules at the interface, and redox-driven changes in adsorbed molecular layers.

## 4.2 Introduction to the Electrochemistry of Redox Metalloproteins

"Dynamic" electrochemistry, i.e. voltammetry as opposed to potentiometry, of redox metalloproteins has developed since about 1980 [Eddowes,79; Yeh,77]. With some exceptions (such as the voltammetry of some blue copper proteins on glassy carbon electrodes and on basal plane pyrolytic graphite [Sakurai,90; Farver,01]) proteins in aqueous solution adsorb irreversibly on most solid surfaces in contact with the solution. Adsorption leads to conformational changes [Brash,95] and loss or attenuation of redox

activity. Most efforts in the 1980's were towards electrode preparation in hydrophobic or hydrophilic states, or with positive or negative excess surface charge. This would ascertain that redox active proteins are drawn close to the electrode surface in configurations favourable for diffusion controlled electron exchange, and at the same time prevent that electrode surface interactions expose internal residues and lead to significant conformational changes. Gentle interactions between protein and electrode surface are commonly achieved by the use of molecules of the general composition X-Y. The X-component, say a thiolate group, adsorbs on the electrode surface, while the Y-component interacts favourably with the protein, by hydrogen bonding or in other ways. The X-Y promoters have no voltammetry of their own. Their primary functions are instead to prevent the protein from irreversible adsorption and collapse, and to orient the protein transiently in favourable electron exchange configurations.

Promoters in diffusion controlled voltammetry of small redox metalloproteins have been broadly mapped and used to achieve reversible voltammetry of cytochromes, blue copper proteins, and iron-sulfur proteins. A second phase in protein voltammetry began in the early 1990's and represents redox metallo*enzymes* [Eddowes,79; Armstrong,97; Brash,95; Davis,00A]. Voltammetry of these larger and more fragile molecules is demanding because of their composite structure and electron transfer mechanisms, which frequently involves more than a single redox centre. In return immobilized metalloenzyme film voltammetry offers new dimensions in electro*catalytic* modes. Whilst from a early stage aimed at analytical perspectives [Burestedt,96; Yaropolov,94] protein film voltammetry has come to offer wider perspectives of molecular *mechanisms* of enzyme function. *Two* issues are particularly apparent. One is the detection of reactive intermediates, say in the peroxidase cycles [Mondal,98], and protonation states of immobilized ferredoxins [Hirst,98]. The other perspective is aimed at electron transport routes in multi-centre redox enzymes between the solvent exposed catalytic site and site(s), which exchange electrons with the electrode. Cases include [Armstrong,97; Armstrong,00] fumarate reductase [Sucheta,93; Heering,97; Leger,01], DMSO reductase [Heffron,01], Ni-Fe hydrogenase [Pershad,99], and nitrate reductase [Anderson,01].

Redox metalloprotein electrochemistry has evolved along two new lines over the last few years. These could be said to constitute "third generation" bioelectrochemistry,

understood as interfacial electrochemical electron transfer of redox metalloproteins and metalloenzymes. Ultimately these two lines can be expected to merge into an overarching approach towards new nanoscale and single-molecule bioelectrochemistry.

Focus in the first new line is on protein and electrode surface "engineering", with a view of creating better-defined redox metalloprotein monolayers where the proteins assume uniform supramolecular monolayer orientations. These efforts have been combined with combinatorial synthetic chemistry in new areas of rationally designed synthetic redox proteins where the class of four-α-helix bundle proteins [Willner,00; Brask,02] is one of the most important. Supramolecular organization has rested on site-directed mutagenesis and chemical marking where specific residues such as cysteines and histidine tags have been engineered into the protein. These groups can link the proteins to the electrode surface, directly or via chemical electrode surface modification. Cys-modified cyt P450 and azurins are such examples [Djuricic,02]. Other examples are reviewed in ref. [Gilardi,01]. The most important efforts in parallel electrode surface engineering have been the systematic use of self-assembled monolayers (SAM's) of functionalized alkylthiolates [Zhang,02]. By suitable choice of functional group redox proteins can be adsorbed onto such layers in multifarious patterns involving hydrophobic, hydrophilic, electrostatic, or hydrogen bond interactions.

The second line of third generation bioelectrochemistry involves the introduction of single-crystal electrode surfaces and *in situ* scanning probe microscopies, particularly atomic force (AFM) and scanning tunnelling microscopy (STM). These notions are established in physical electrochemistry but *novel* in bioelectrochemistry, with only a few reports of state-of-the-art physical electrochemistry combined with functional redox protein monolayers. Most data refer to *Pseudomonas aeruginosa* azurin. This protein can, for example, be brought to immobilization in opposite orientations on bare and alkylthiolate-modified Au(111)-electrode surfaces, respectively. Functional protein integrity has been ascertained, and details of interfacial tunnelling disclosed [Chi,00; Chi,01]. Other metalloproteins with comparable detail emerging are *Pyrococcus furiosus* ferredoxin [Zhang,03] and *Saccharomyces cerevisiae* cytochrome *c*, cf. below. These studies have mapped electrochemistry of redox proteins on single-crystal electrode surfaces and disclosed structural and functional protein features at the *single-molecule* level. This novel bioelectrochemical research, combined with protein

engineering holds new promise for pure and applied bioelectrochemistry, biosensor technology etc., towards real nanoscale and single-molecule levels.

## 4.3 Results

### 4.3.1 Linear Sweep Voltammetry of YCC and L-cysteine

Fig. 4.10 shows linear sweep voltammetry (LSV) of the reductive desorption of L-cysteine and YCC adsorbed at Au(111)-electrodes in 0.1 M NaOH. Peaks at –0.742 V vs. SCE for YCC[1] and –0.745 V for L-cysteine, strongly indicate reductive desorption.

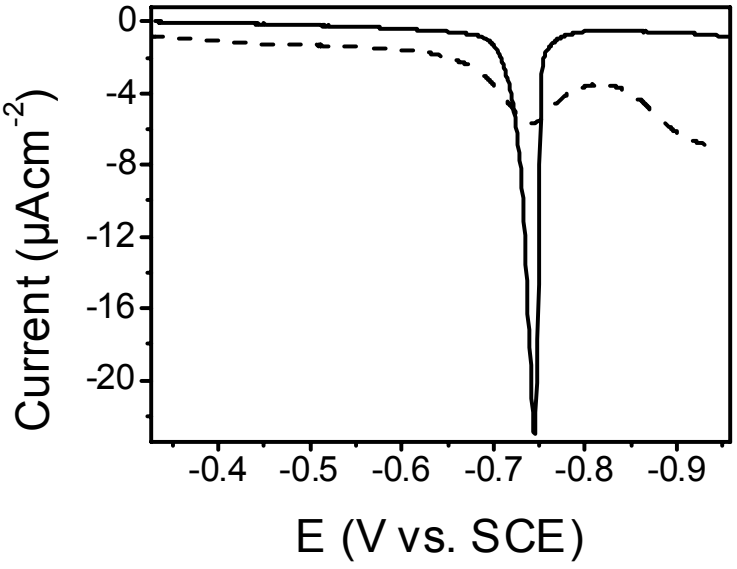


**Figure 4.10**: LSV of L-cysteine (fully drawn) and YCC (dashed) adsorbed at Au(111)-electrodes in 0.1 M NaOH. Scan rate 10 mV/s. Cathodic scan.

The cysteine peak is sharp; the peak current is -26 $\mu Acm^{-2}$ and the width only 15 mV. The charge transferred is 54 $\mu Ccm^{-2}$, which corresponds to $3 \times 10^{14}$ molecules·$cm^{-2}$ or close to monolayer coverage, which was measured as $4.6 \times 10^{14}$ molecules·$cm^{-2}$ [Zhang,00]. The YCC peak is broader, 63 mV and the current only -3.5 $\mu Acm^{-2}$. The charge transferred in the YCC peak is 26 $\mu Ccm^{-2}$. A YCC molecule occupying $4 \times 4$ $nm^2$ that desorbs by accepting one electron would, however, give a charge of only 1.0

[1] In one case a reductive desorption potential of –0.937 mV was observed. In the majority of cases, however, reductive desorption potentials of app. –0.74 V vs. SCE were observed

$\mu Ccm^{-2}$. A more densely packed layer where YCC occupies 3.5 × 3.5 $nm^2$, gives a charge of 1.3 $\mu Ccm^{-2}$. A closely packed monolayer of incompressible spheres with diameter 3.5 nm would contain $9.4 \times 10^{12}$ $cm^{-2}$ and give 1.5 $\mu Ccm^{-2}$ when assigning one unit charge per sphere. The charge therefore cannot be due to sulfur reduction of Cys102 alone. Unfolding of YCC upon adsorption and subsequent exposure of other sulfur atoms in YCC (altogether four other sulfurs) could account for some of the charge. Another likely cause is capacitive contributions.

Fig. 4.11 shows the capacitance of YCC adsorbed on Au(111) in 0.1 M NaOH. Two peaks are clearly seen. The main peak is located at –0.955 V with a charge of 1.97 $\mu Ccm^{-2}$, which formally corresponds to around two monolayers. Deducting this value from the value obtained by CV leaves 24 $\mu Ccm^{-2}$ or 16-24 monolayers. In the harsh alkaline environment of 0.1 M NaOH YCC is, however, completely unfolded and all five sulfur atoms exposed, thereby participating in the desorption process. It is, however, not straightforward to assign the peak to reductive desorption as the potential is shifted from the potential in Fig. 4.10. The minor capacitance peak at –0.552 V has a charge of 0.45 $\mu Ccm^{-2}$. This peak is assigned to reduction of non-native heme even though it is 0.10-0.15 V more negative than observed at neutral pH [Feinberg,98].

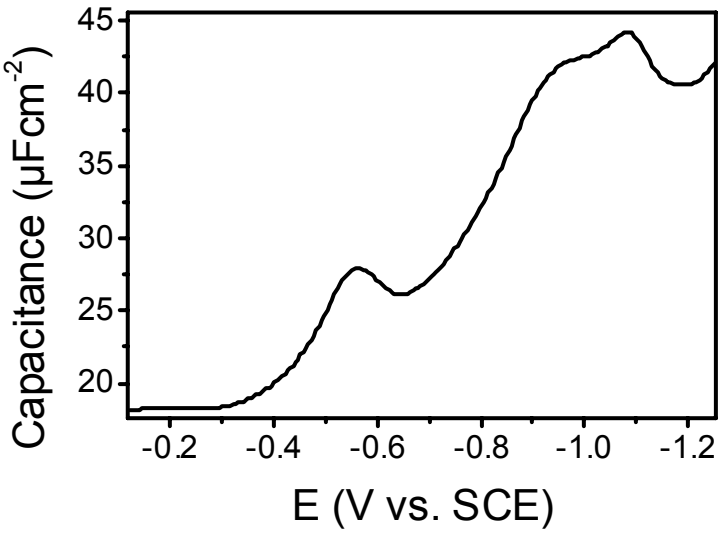


**Figure 4.11**: Capacitance of YCC adsorbed at Au(111)-electrodes in 0.1 M NaOH. Cathodic scan.

The unfolding of YCC is supposed to be less severe in a biocompatible buffer. Fig. 4.12 shows a LSV of YCC at Au(111) in 0.1 M $KH_2PO_4/K_2HPO_4$, pH 7.2. The voltammogram shows two peaks located at 0.079 V and –0.735 V vs. SCE. The insets zoom in on the individual peaks. The inset for the peak at –0.735 V is constructed by using a linear baseline. The peak clearly represents reductive desorption. The apparent charge transferred in the peak is 10 ± 2 $\mu Ccm^{-2}$ or 8-10 monolayers. A 'shoulder' is present at -0.806 V on the negative potential side of the main peak. The shoulder could represent desorption of a different sulfur species, perhaps sulfur fragments from YCC or more strongly adsorbed YCC. A lower reduction potential indicates a stronger bond. In that respect it looks like the capacitance data in Fig. 4.11, which also featured a double peak. The potential of the peak at 0.079 V is not too far from the redox potential of native cytochrome *c* at modified gold electrodes, which is 12-50 mV vs. SCE [Komar-Panucucci,94; Feinberg,98; Rosell,98]. It is also close, however, to the desorption potential of phosphate, which is 0.077 V.

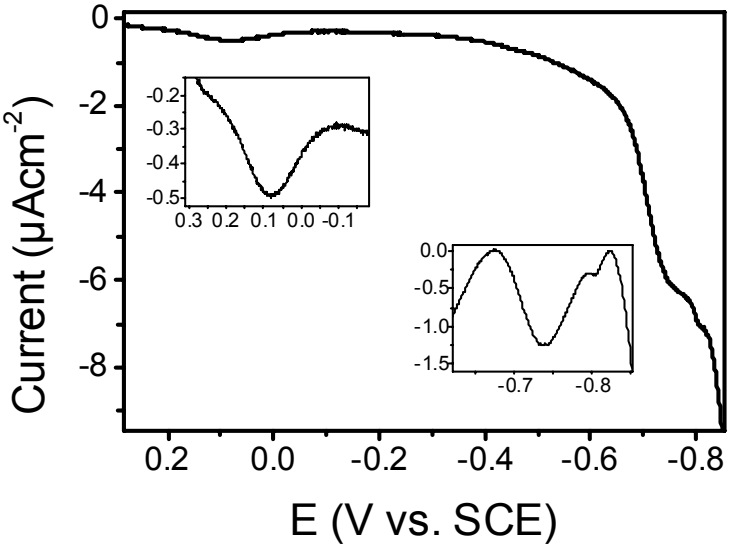


**Figure 4.12**: LSV of YCC at Au(111)-electrodes in 0.1 M $KH_2PO_4/K_2HPO_4$, pH 7.2. Scan rate 10 mV/s. Cathodic scan.

The capacitance data in Fig. 4.13 of YCC in phosphate buffer at neutral pH exhibit two peaks. A small peak is present at –0.78 V with a charge of only 0.07 ± 0.02 $\mu Ccm^{-2}$. This small charge constitutes less than one percent of the charge obtained by LSV,

hence the capacitive contribution to that peak is neglible. It should be noted that the scan rate in capacitance measurements is significantly smaller than in LSV experiments, which might influence the capacitive current. A peak at –0.460 V could correspond to heme reduction of non-native YCC. This potential is characteristic of partially unfolded cytochrome *c*, where the ligation between heme iron and Met80 is broken [Feinberg,98; Battistuzzi,02].

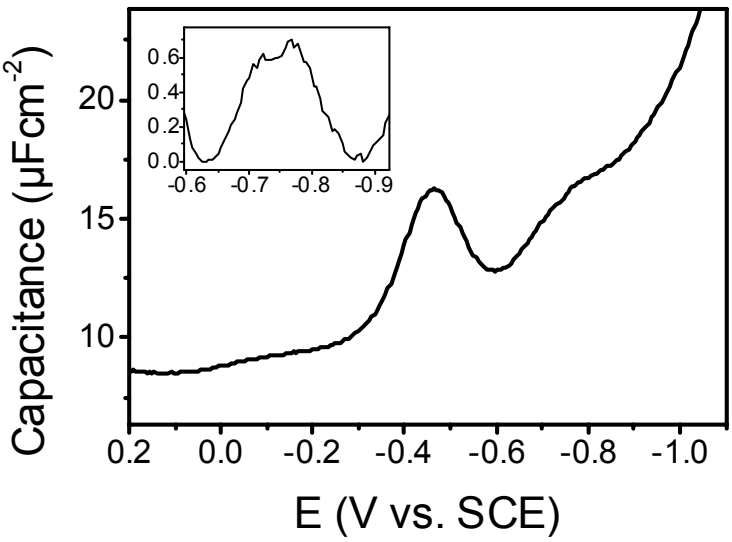


**Figure 4.13**: Capacitance data for YCC in 0.1 M $KH_2PO_4/K_2HPO_4$, pH 7.2. Cathodic scan.

The existence of a non-native state of the similar protein HHCC was also studied at Self-Assembled Monolayers of carboxylterminated alkanethiols on silver by SERR [Murgida,01]. The electric field experienced by HHCC could be varied by the length of the alkanethiols. Adsorbed HHCC were seen to exist in two conformational states: the native state B1 and a non-native state B2 that lacked the Met-80 axial ligand [Murgida,01]. The ratio of B2 to B1 was increased for short-chain alkanethiols due to the electric field experienced by HHCC. The electric field at a Au(111) electrode depends strongly on the potential. The electric field dependence of the equilibrium constant, K(EF), for the B2/B1 transition was given by

$$\frac{\partial \ln K(E_F)}{\partial E_F} = \frac{N_A \Delta \mu}{RT} \qquad (4.5)$$

where $N_A$ is Avogadro's number, $\Delta\mu$=10 D is the dipole moment difference between reactants and products, and the electric field could be approximated by

$$E_F \approx -\frac{\sigma_{IH}}{\varepsilon_0 \varepsilon_{IH}} \tag{4.6}$$

where $\sigma_{IH}$ is the charge density and $\varepsilon_{IH}$ = 5 the dielectric constant in the electrochemical double layer. Given the measured capacitance for the YCC/Au(111) interface, 9 $\mu Fcm^{-2}$, the ratio of B2 to B1 would be 100 at potentials 150 mV negative of the potential of zero charge, which is 0.23 V vs. SCE for unreconstructed Au(111) [Kolb,95]. Thus according to this crude model, the ratio of B2 to B1 would be 100-1000 around the redox potential of native HHCC. This model should be applicable for YCC also due to the strong similarity between YCC and HHCC.

### 4.3.2 Differential Pulse Voltammetry

The high background current in LSV especially at negative potentials makes it difficult to retrieve information about the peak properties. Reductive desorption signals can be more easily obtained at neutral pH by using the more sensitive technique DPV where capacitive currents are suppressed. Integration of a current peak will not, however, yield the charge transferred and thereby the coverage of adsorbed species. As seen in Fig. 4.14, a reductive desorption signal in phosphate buffer can indeed be distinguished at -0.74 V. Integration of the peak yields 5.1 ± 1.2 $\mu Acm^{-2}\times V$. By comparison with the charge obtained by LSV and using eq. (4.2) the electron transfer rate constant $k_0$ is estimated at 0.06 $s^{-1}$, which is physically reasonable. The peak current is –38 $\mu Acm^{-2}$ or approximately thirty times larger than observed in LSV. An additional structure at –0.44 V in the voltammogram would correspond to reduction of non-native YCC. The inset in Fig. 4.14 is a zoom of the peak. The integral of this peak is 0.56 ± 0.19 $\mu Acm^{-2}\times V$, which using eq. (4.2) and the charge obtained by capacitance (0.52 $\mu Ccm^{-2}$) gives an electron transfer rate constant $k_0$ of 0.14 $s^{-1}$ for reduction of non-native YCC.

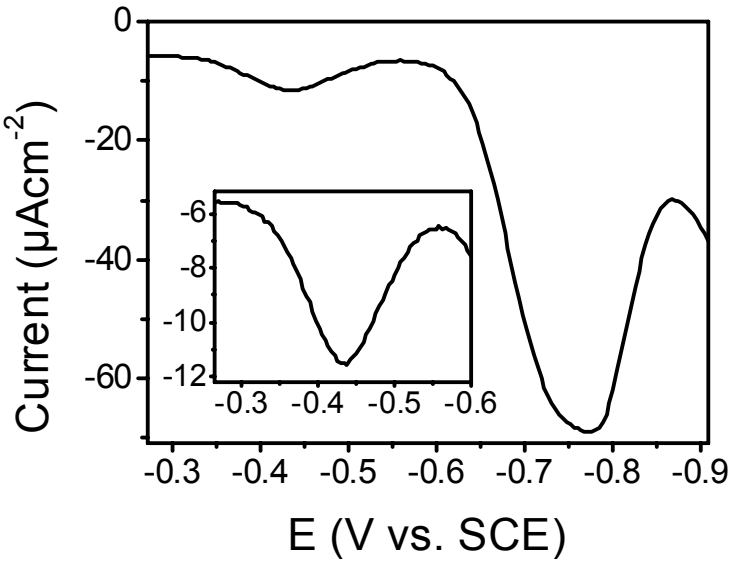


**Figure 4.14**: DPV of YCC at Au(111)-electrodes in 0.1 M $KH_2PO_4/K_2HPO_4$, pH 7.2. Low-potential region from –0.3 V to –0.9 V. Scan rate 10 mV/s. Pulse height 25 mV, pulse duration 7 ms, time between pulses 400 ms. Cathodic scan.

A small third peak is present at 0.073 mV in phosphate solution. This peak appears in the second and subsequent scans (Fig. 4.15, left), but only in cathodic scans. The peak is quite close to the reduction potential of native cyt *c* at modified surfaces (+20 mV) [Ion,01]. The bulk reduction potential of cyt *c* of 12-50 mV vs. SCE is also close to this value. Before assigning the peak to reduction of native, functional YCC it is, however, necessary to exclude that the signal originates from phosphate desorption. Perchlorate is known not to adsorb to gold [Hamelin,96]. The right panel in Fig. 4.15 shows a DPV of YCC at Au(111)-electrode in 0.1 M $NaClO_4$-electrolyte. A small peak is still visible but now at 0.007 V, that means close to the reduction potential of native cytochrome *c* and with no convolution of peaks from anion adsorption/desorption. The peak is strongly attenuated in subsequent scans and is not visible in anodic scans. The integrated current is 0.10 $\mu Acm^{-2} \times V$. As seen in Fig. 4.15 the background current in the anodic scan is also twice as high as in the cathodic scan. Before each potential scan the electrode was held for 30 seconds at the start potential. The start and end potentials for the scans were chosen to cross the reduction potential $E^o$ of YCC at modified electrodes (+20 mV). For cathodic scans the start potential was 0.3 V and the end potential –0.3 V; for anodic

scans vice versa. Electrostatic repulsion of the strongly positively charged YCC and the electrode surface could thus cause the peak to be visible only in cathodic scans. Willner et al. used this feature to control the electron transfer reaction of YCC at a modified gold electrode [Pardo-Yissar,00]. In this case it seems that pre-conditioning at positive potential facilitates YCC heme electron transfer at the modifier layer. The attenuation in the present case can be explained by deterioration of the adsorbed layer, when the potential is scanned. The attenuation can be decreased by limiting the potential excursion in the cathodic scan to less negative values.

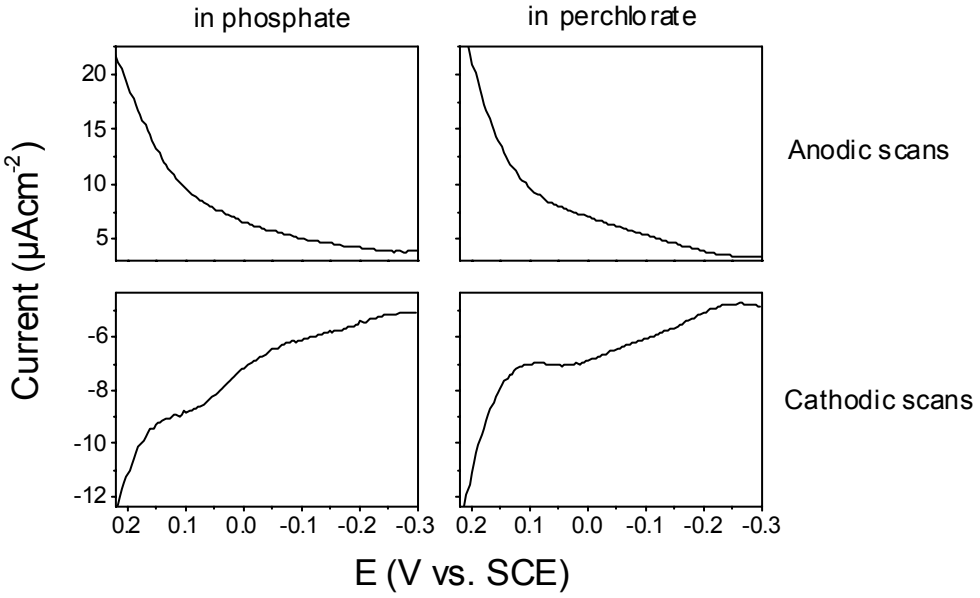


**Figure 4.15**: DPV of YCC at Au(111)-electrodes. Scan rate 10 mV/s. Pulse parameters as in Fig. 4.14. High-potential region from 0.2 to –0.3 V. **Left**: in 0.1 M $KH_2PO_4/K_2HPO_4$, pH 7.2.: **Right**: in 0.1 M $NaClO_4$, pH ≈5. Anodic scans in top row, cathodic scans in bottom row.

Table 4.1 summarizes the results obtained for YCC adsorbed on Au(111) in phosphate buffer and sodiumhydroxide.

**Table 4.1**: A) Reduction potential of signals coming from reductive desorption of YCC and reduction of non-native YCC heme (in mV vs. SCE) as function of media and method used. The reduction potential is (mostly) calculated as an average of several experiments, the number of which is shown in paranthesis. B) Charge of the peaks used in A). For DPV the integrated current is shown, which is proportional but not identical to the coverage of YCC.

| A | REDUCTION POTENTIAL (mV vs. SCE) | | | |
|---|---|---|---|---|
| Medium | LSV | DPV | Capacitance | Origin of peak |
| phosphate | -741 ± 8 (2) | -741 ± 19 (6) | -782 ± 13 (3) | Reductive desorption |
| hydroxide | -742 ± 1 (2) | -756 (1) | -955 (1) | |
| phosphate | - | -437 ± 5 (6) | -460 ± 5 (3) | Non-native YCC |
| hydroxide | -430 | -537 | -552 | |

| B | CHARGE | | | |
|---|---|---|---|---|
| Medium | LSV ($\mu Ccm^{-2}$) | DPV ($\mu Acm^{-2}V$) | Capacitance ($\mu Ccm^{-2}$) | Origin of peak |
| phosphate | 10.4 ± 2.0 (2) | 5.1 ± 1.4 (6) | 0.066 ± 0.020 (3) | Reductive desorption |
| hydroxide | 26 ± 8 (2) | 0.5 (1) | 2.0 (1) | |
| phosphate | - | 0.6 ± 0.2 (6) | 0.52 ± 0.07 (3) | Non-native YCC |
| hydroxide | 1.0 (1) | 0.01 (1) | 0.45 (1) | |

## 4.4 Conclusion

LSV, DPV and capacitance measurements have disclosed the presence of adsorbed YCC at Au(111) electrodes. A reductive desorption signal in pohsphate buffer at -0.75 V in LSV and DPV strongly indicates binding of YCC to Au(111) via sulfur. The charge transferred in this peak indicates that YCC is bound to gold with several sulfur atoms and not only Cys102. YCC is expected to unfold in alkaline solution, thereby exposing more sulfur atoms to the gold surface. Accordingly, the charge is 2-3 times larger in alkaline solution than in neutral solution.

The presence of a DPV peak at 0.079 V in phosphate buffer might originate from phosphate desorption but could also reflect the voltammetric activity of native YCC. A DPV signal at 0.007 V in perchlorate electrolyte is thought to originate from heme reduction of native YCC.

DPV and capacitance measurements of YCC shows a signal at app. –0.44 V originating from reduction of heme of non-native YCC.

# 5 XPS

## 5.1 Introduction to XPS

X-ray photoelectron spectroscopy is a technique that is extremely useful in detection of chemical elements in solid surface samples. The method is based on the photoelectric effect, discovered by Einstein in 1905 [Chorkendorff,94]. When a solid is bombarded with X-rays of sufficient energy, electrons of a certain kinetic energy are released (Fig. 5.1). The kinetic energy of these electrons is a function of the energy of the X-ray, the binding energy (ionization) of the electron, $E_B$, and the work function of the solid, $\Phi$, as shown in eq. (5.1).

$$E_{kin} = h\nu - E_B - \Phi \tag{5.1}$$

where $\nu$ is the frequency of the incoming X-ray, and h Planck's constant. The work function for Au is 5.3 eV.

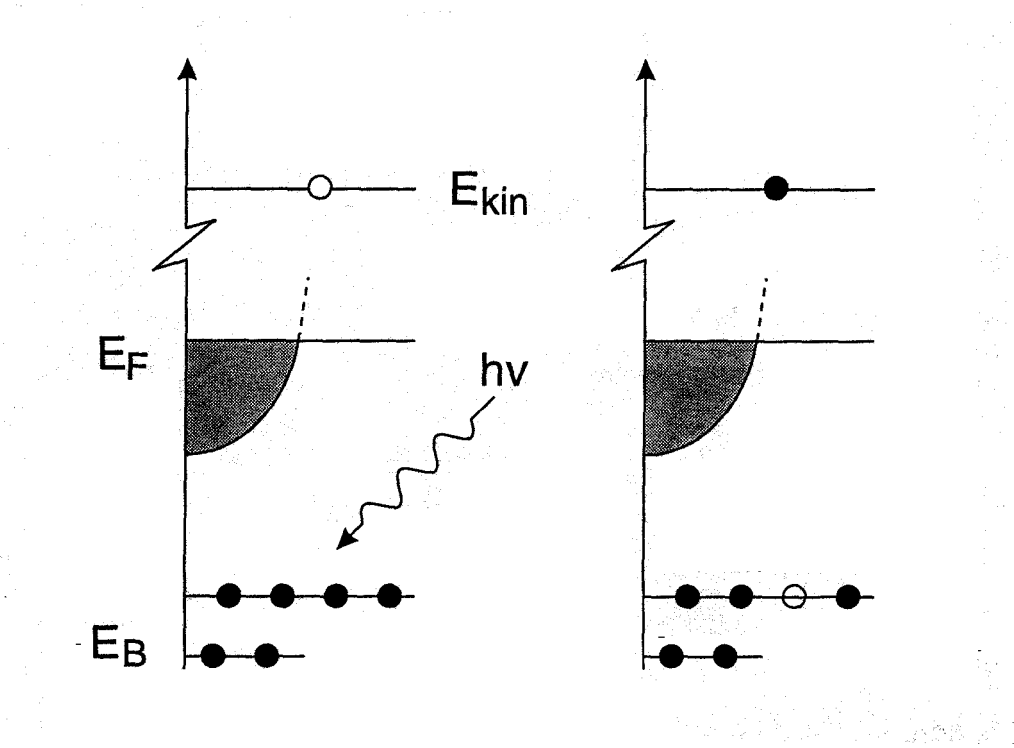


**Figure 5.1**: Schematics of the photoemission process. From [Chorkendorff,94]

A typical X-ray source is a dual anode, which consists of a core of aluminum and magnesium and surrounding tungsten filaments. High energy electrons (15 kV) bombard either the Al or Mg anode and ionize the atom by kicking out one of the inner electrons. A weakly bound electron in the excited atom will relax into the created hole. The excess energy is used to emit an X-ray. Several transitions are possible with distinct energies. The main transition for Al is 1486.6 eV. The main transition for Mg is at 1253.6 eV.

The X-rays are directed at the solid sample to be investigated and ionize atoms. The released photoelectrons from the sample have a kinetic energy that depends on their binding energy, the energy of the X-rays and the work function of the solid according to eq. 5.1.

The use of a monochromatic X-ray source means that the kinetic energy can be used to calculate the binding energy. When sampling over all kinetic energies, a spectrum of binding energies is obtained. The binding energy of electrons for different elements is very distinct, which means that elements can be identified. In addition the number of electrons emitted is proportional to the amount of the given element present. Likewise the binding energy of the element is shifted to a different extent by electron exchanging atoms. Hence, a shift in binding energy can be used to determine the chemical environment of a given element.

When the electrons are released from the sample they enter a hemi-spherical analyzer. The analyzer consists of two concentric hemi-spheres over which a potential difference is supplied. The orbit of the photoelectron is perturbed by the positively charged inner sphere (Fig 5.2). When a large potential difference is supplied, only a very narrow distribution of kinetic energies through the analyzer is allowed, hence high energy resolution is achieved. The width of this energy window is denoted the pass energy. A low pass energy means, however, that the number of electrons allowed through the analyzer is diminished. The small number of electrons results in a low signal to noise ratio, that can be partly overcome by sweeping the energy range many times.

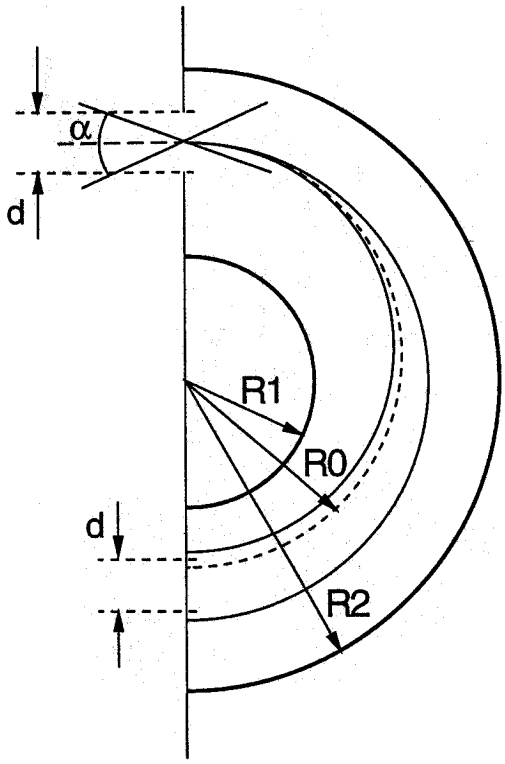


**Figure 5.2**: Schematics of a hemi-spherical analyzer. From [Chorkendorff,94].

In the past XPS has been used to investigate catalysts [Kerkhof,79], thin films [Paz,94], quantitative analysis of alloys [Adams,77], and depth profiles of surfaces [Baird,76]. Recently the method has been used for monolayer samples and biomolecules. One of the challenges in working with monolayer samples is the risk of radiation damage [Liao,02]. In order to get a good determination of the spectrum (number of counts of electrons), it is necessary to sweep the energy range many times. Unfortunately, the prolonged radiation time damages the sample. The spectrum of a fresh sample is thus different from the spectrum of a irradiated sample. It is therefore necessary to find a compromise between these two effects.

### 5.1.1 Introduction to XPS and sulfur-containing monolayers

XPS-investigations of sulfur-containing molecules have focused particularly on alkanethiols adsorbed on gold. Other molecules investigated are thiophene, cysteine,

DNA [Lenigk,01] and thiolated porphyrins. These small molecules are adressed in section 5.1.2.

XPS investigations of larger molecules such as proteins and enzymes are very few in numbers, probably due to the difficulty in analysis of a large number of atoms. Such investigations are, however, described in section 5.1.3.

### 5.1.2 Small Molecules With Functional Thiol Groups

ALKANETHIOLS

Alkanethiols give rise to a characteristic pair of peaks in the thiolate binding energy range. The two peaks at 162.2 and 163.3 eV represent the spin-orbit coupling of the S $2p_{3/2}$ and S $2p_{1/2}$ orbitals by the Au and is a fingerprint feature of sulfur-gold interaction [Yang,01]. The ratio of the intensities of the peaks have been shown to be 2:1 [Castner,96]. The peak positions are reported to vary with chain length [Bain,89A] and the preparation of the gold samples [Bain,89A; Walczak,95; Liao,02].

XPS has shown that thiols and disulfides yield the same chemical species upon adsorption with indistinguishable XPS spectra. This implies that the disulfide bond is broken on adsorption [Bain,89B].

The existence of different adsorption sites for alkanethiols at stepped gold surfaces has also been shown [Walczak,95]. Gold was evaporated onto substrates of different flatness. The two sulfur peaks of adsorbed octanethiol are clearly resolved at the highly flat Au/mica surface. Au/silicon and Au/glass surfaces are less flat and contain a larger number of steps. The sulfur peaks at these surfaces are shifted to marginally lower binding energies and are broader on the low-energy side. The shape of the peaks is explained by the existence of two different adsorption sites on the gold, i.e. on the terrace and at steps [Walczak,95].

The signal from an atom in a monolayer depends on the position in the monolayer. A fraction of the photoelectrons emitted will always be stopped or slowed down when travelling through the monolayer. Photoelectrons emitted from atoms near the surface provide a relatively higher signal because the emitted electrons have to travel a shorter distance. Hence a larger fraction of that element reaches the detector. Photoelectrons from atoms near the interface, however, must travel through more material and give a

relatively lower signal. The difference in the probability of penetrating the monolayer depending on the position in the monolayer is denoted surface sensitivity. The take-off angle is the angle between emitted electrons and the surface. Signals are thus highest with a take-off angle of 90° when the route of the photoelectrons is the shortest. The difference in surface sensitivity can be increased by using a lower take-off angle thereby increasing the difference in the length of the photoelectron routes. The longer photoelectron routes will, however, decrease the amount of photoelectrons detected thus givng a lower signal. Angle-dependent XPS has been used in this way used to confirm the orientation of methyl 10-mercaptodecanoate on gold with the sulfur closest to the interface and oxygen and ester carbons farthest away [Bain,89A].

The intensity of the photoelectrons from the material underneath a thin film depends crucially on the thickness of the thin film and the take-off angle. The intensities of the gold signals at 83.8 and 87.5 eV were used to calculate the thickness of a 1-mercaptododecane layer on Au(111) [Kondo,98]. The thickness of the monolayer was calculated as 17 Å in good agreement with a tilt angle of the molecules of 30°.

Angle-resolved XPS was used to determine the thicknesses of films of 1-decanethiol prepared from gas-phase dosing and solution immersion, respectively. The thickness of gas-phase dosed films was three times smaller than films prepared by solution immersion. The position of the C 1s signal also shifted with the (size of) gas-phase dose. The main peak is at 284.1 eV and a shoulder at 285 eV is observed at higher doses. The observations were explained by the existence of two phases: lying-down and standing-up molecules in gas-phase dosed films. The carbon atoms of lying-down molecules were proposed to be more electronically relaxed than carbon atoms of standing-up molecules due to their proximity to the gold atoms. A lower binding energy is thus expected [Yang,01].

## OTHER SMALL MOLECULES

Other small sulfur molecules to have been studied by XPS are L-cysteine [Cavalleri,01,Zhang,00], 3-mercaptopropylmethoxysilane [Brito,02], and thiolated porphyrins [Boeckl,00; Bramblett,02]. L-cysteine was found to contain signals from two sulfur species: One large doublet from thiolated cysteine with a binding energy of 162.3 eV and a small doublet at 164.0 eV, which was attributed to L-cysteine physisorbed to a

first layer of chemisorbed L-cysteine [Cavalleri,01]. The binding energy of sulfur that interacts less with metal (i.e. physisorbed L-cysteine) is likely to resemble the binding energy of bulk samples, which was determined as 163.8 eV [Gold,89].

The opposite situation was found for 3-mercaptopropylmethoxysilane, which adsorbed predominantly as a disulfide with a binding energy of 163.5 eV. A smaller fraction adsorbed as thiolate with a binding energy of 162.3 eV

The concept of bound and unbound sulfur was explored by Boeckl et al. by using a phosphor-porphyrin, that was thiolated on each side of the porphyrin plane [Boeckl,00]. The sulfur signal could indeed be fitted by two doublets of equal size located at 162 and 164 eV corresponding to bound and unbound sulfur. The coverage of the porphyrin was estimated using a model based on the density of the porphyrin and parameters for the inelastic mean free path of the elements in gold and in the organic overlayer [Bramblett,02].

### 5.1.3 Large thiol-containing molecules

The number of XPS studies of larger biomolecules focus mainly on linker molecules used to attach the biomolecules to solid surfaces [Jiang,97; Patel,97]. Jiang et al. used XPS to characterise a 3-mercaptopropylamide linker layer on gold produced in two different ways, that had been shown to give different reduction potentials for adsorbed cytochrome *c*. The iron signal from cytochrome *c* heme could be detected. The signal was too low, however, to determine any qualitative difference between the two methods. The nitrogen signal of the linker layers were different and it was proposed that the difference in reduction potential arose from a combination of different electrostatic interaction and steric hindrance during the adsorption of cyt *c* [Jiang,97].

One investigation did focus on direct attachment of a large biomolecule on a surface [Brizzolara,97]. A cysteine residue was genetically engineered into the surface of Bacteriorhodopsin (BR). Wild-type BR does not contain cysteine, but nine methionines. The ratio of the sulfur and nitrogen signals was eight times higher for wild-type BR adsorbed on gold than expected from the elemental composition. The ratio for engineered BR was only 1.4. The excess sulfur observed for wild-type BR was

explained by the adsorption of dissociated methyl mercaptan groups on gold. These methyl mercaptan groups originated from the surface methionine groups of BR. After rinsing the methyl mercaptan groups remained at the surface, while the rest of BR was washed away, thus giving a higher ratio of sulfur to nitrogen.

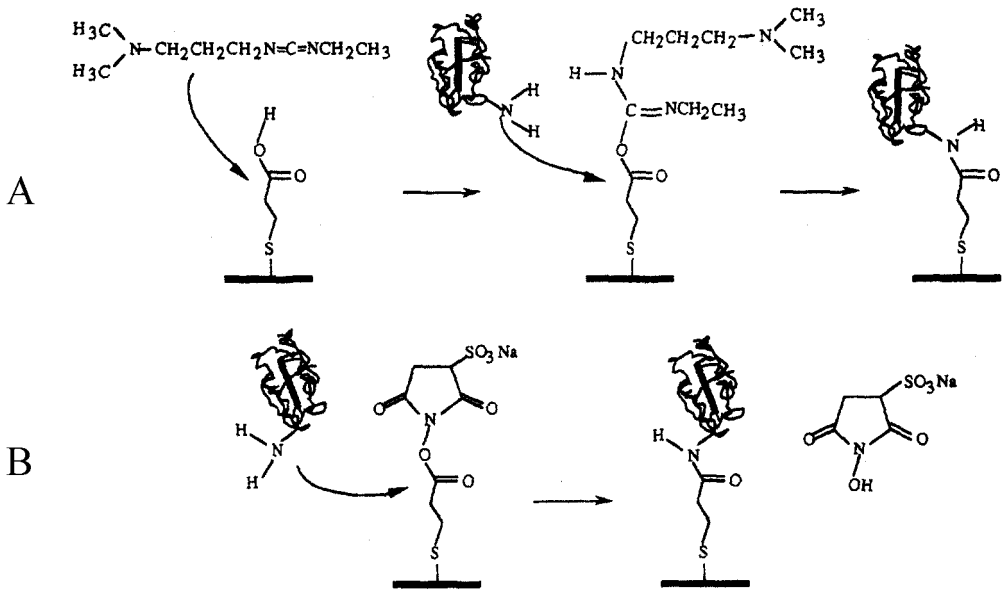


**Figure 5.3**: Immobilization scheme used by Jiang et al. to adsorb cyt *c*. From [Jiang,97].

## 5.2 Cytochrome *c* on gold

### 5.2.1 Experimental procedure

Technical information

The XPS spectra were recorded using a Perkin Elmer surface analysis system (Physical Electronic Industries, Inc., USA) equipped with a multi-channel detector. A Mg-anode operated at 200 W was used to generate X-rays. The pressure in the chamber during data acquisition was less than $1x10^{-9}$ Torr. A pass energy of either 25.0 or 50.0 eV was applied. All spectra were acquired at room temperature and are referenced to the $Au(4f_{7/2})$ line at 84.00 eV.

Sample preparation

The gold disk electrodes that were used for STM measurements were also used for XPS. The disk electrodes were cleaned and pre-treated as described in sec. 3.3. For measurements with cytochrome *c* the electrodes were soaked in a solution of 0.1 mM yeast cytochrome *c*/horse heart cytochrome *c*, 10 mM potassium phosphate, pH 7.3 for three days. Experiments with lower cyt *c* concentration (0.03 mM) did not provide a reasonable sulfur signal. Adsorption of the reference molecule L-cysteine was performed by soaking the gold electrode in a 1 mM solution overnight, i.e. >10 hours. After soaking the electrodes were washed once in buffer and twice in Millipore water. The remaining liquid on the electrodes were allowed to dry under a gentle flow of nitrogen. The electrodes were then transferred to the vacuum chamber of the XPS analyzer. The working pressure of the analyzer was $10^{-10}$–$10^{-9}$ Torr.

Data analysis

As a standard the sulfur binding energy range (168-158 eV) was investigated first, followed by carbon (293-279 eV), nitrogen (406-395 eV), oxygen (537-528 eV), iron (717-703 eV), and gold (94-80 eV). The spectra obtained for the C, N, O, and S signals were deducted a linear baseline in order to perform integration of the respective peaks and to ease comparison between YCC and HHCC spectra. The spectra obtained for the Fe signal did not exhibit a resolved peak. Instead the photoelectron intensity at 703 eV was deducted as background.

### 5.2.2 Results

YCC is proposed to bind to Au via Cys102. Hence L-cysteine is chosen as reference molecule. Reference XPS spectra of horse heart cytochrome *c* (HHCC) were also obtained.

HHCC is very similar to YCC, except that it contains a serine instead of Cys at position 102. Hence HHCC should not exhibit a Au-S signal and a difference in sulfur binding energy range should be observed. The XPS spectra obtained are divided into

two parts; one for the small reference molecule L-cysteine and one for the proteins YCC and HHCC.

Atomic composition

The areas under the peaks in the XPS spectra are proportional to the amount of the given element present in the sample. The elements have different cross sections and number of electrons, and hence different sensitivity to the XPS method. Large metal atoms such as Au thus have a high probality to catch an X-ray and emit electrons. Small atoms like C have a low probability. Empirical sensitivity factors for the elements are listed in ref. [Wagner,78]. By dividing the values of the areas with these factors the atomic surface composition of the sample is obtained.

L-CYSTEINE

Table 5.1 shows the atomic surface composition of an L-cysteine sample. The deviations from the expected composition are in the range 32-55 %. The largest absolute deviation is for carbon; 43 % is expected, 66 % is measured. XPS spectra of a cleaned gold electrode surface, however, contained 30 % carbon (data not shown). The impurities probably come from the air during the transfer to the UHV chamber.

**Table 5.1**: Measured and expected atomic composition of L-cysteine. A) All elements B) disregarding the carbon signal.

| A | L-cysteine | | |
|---|---|---|---|
| Element | Measured atomic concentration (%) | Expected atomic concentration (%) | Deviation (%) |
| Sulfur | 7.82 | 14.29 | -45 |
| Nitrogen | 6.46 | 14.29 | -55 |
| Carbon | 66.34 | 42.86 | +55 |
| Oxygen | 19.38 | 28.57 | -32 |

| B | L-cysteine disregarding carbon | | |
|---|---|---|---|
| Element | Measured atomic concentration (%) | Expected atomic concentration (%) | Deviation (%) |
| Sulfur | 23.23% | 25.00% | -7 |
| Nitrogen | 19.19% | 25.00% | -23 |
| Oxygen | 57.58% | 50.00% | +15 |

Figure 5.4 shows the sulfur signal from L-cysteine. Gold-thiolate peaks at 162.2 and 163.4 are present as expected in the ratio 2:1.

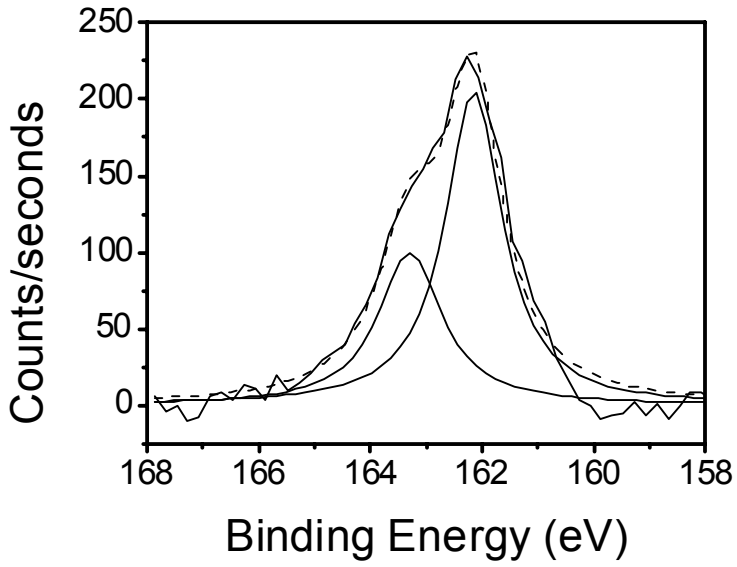


**Figure 5.4**: XPS spectra of L-cysteine. Sulfur 2p binding energy range. Acquired at 25.00 eV pass energy. 405 sweeps, 25 seconds pr. sweep. Fit (dashed) is composed of Lorentzian curves.

YEAST CYTOCHROME *C* AND HORSE HEART CYTOCHROME *C*

Table 5.2 shows the measured and known composition of cytochromes *c*. The table shows that XPS estimates the atomic composition of both cytochromes quite well. The measured values generally deviate from the expected values by up to 10 %. The sulfur signal is consistently overestimated by a factor of 2-3. In native cytochrome *c* (yeast and

horse heart) the atomic concentration of sulfur is 0.5 %. Hence the sulfur signal will be small and the integration of the sulfur will be flawed with uncertainties. The deviation could be explained by an inaccurate sensitivity factor or exogenous sulfur, but the more probable explanations are the inherent uncertainty of the method or incorrect positioning of the baseline used for integration of the sulfur signal. The latter would only contribute marginally.

In each case the amount of carbon is overestimated compared to the composition of cyt *c*. The reason could be due to the uncertainty of the method. It could also be due to exogenous carbon. Measurements of a sample without adsorbate disclose around 30 % carbon, 10 % oxygen and 60 % gold, i.e. one carbon atom is detected for every two gold atoms. The X-rays penetrate the sample by a few atomic layers, hence photoelectrons are emitted from all these layers. That means atoms from beneath the top layer of gold are also detected. Consequently the ratio of carbon atoms and top layer gold atoms is higher than 1:2.

**Table 5.2**: Measured and known atomic composition of yeast and horse heart cytochrome *c* [Louie,90].

| YCC | | | |
|---|---|---|---|
| Element | Measured atomic concentration | Expected atomic concentration | Deviation (%) |
| Sulfur | 1.45 % | 0.56 % | +159 |
| Nitrogen | 16.61 % | 17.45 % | -5 |
| Carbon | 65.77 % | 63.96 % | +3 |
| Oxygen | 16.18 % | 18.02 % | -10 |
| HHCC | | | |
| Sulfur | 1.01% | 0.46% | +120 |
| Nitrogen | 13.30% | 17.15% | -22 |
| Carbon | 67.04% | 64.56% | +4 |
| Oxygen | 18.65% | 17.84% | -5 |

### 5.2.3 The individual element signals

Fig. 5.5-5.10 show XPS spectra obtained for yeast and horse heart cytochrome *c*, respectively.

The sulfur signal

The main peaks in Fig. 5.5A for both YCC and HHCC are located at 163.4 and 162.2 eV. These energies are consistent with those of cysteine (Fig. 5.4) and alkanethiols adsorbed on gold [Chi,00]. The ratio of the peaks at 163.4 and 162.2 eV is different for YCC and HHCC; the peak at 162.2 eV is higher than the peak at 163.4 eV for HHCC suggesting a higher degree of gold-thiolate bonding. The peak at 163.4 eV is higher than the peak at 162.2 eV for YCC. The YCC sulfur peak is significantly broader than the HHCC sulfur peak. The broadness and shape of the peak are quantified by fitting the peaks to Lorentzian curves (Fig. 5.5B). These fits disclose several peaks. For YCC a small shoulder is present at 161.2 eV and a larger shoulder at 164.6 eV in addition to the main peaks. The HHCC peak is adequately fitted by the main peaks and a shoulder at 164.8 eV. The sulfur binding energies are usually shifted to higher values in compounds where sulfur is bonded to oxygen. Hence the shoulder at 164.6-164.8 eV could be due to oxidized sulfur. Sulfur peaks at 164-165 eV have also been linked to non-bound sulfur [Boeckl,00,Chi,00]. The higher intensity of the 164.6 eV peak for YCC indicates a higher degree of unfolding.

YCC contains five sulfur atoms, HHCC contains four. The presence of more sulfur species could also give a broader peak. Putting the protein into vacuum will most likely unfold the protein [Clemmer,95]. YCC is known to unfold more easily than HHCC in aqueous solution, that means at lower temperatures [Andersen,02; Nall,96] or lower concentrations of guanidinium chloride [Komar-Panucci,94; Andersen,02]. YCC is therefore also expected to unfold to a higher degree in UHV.

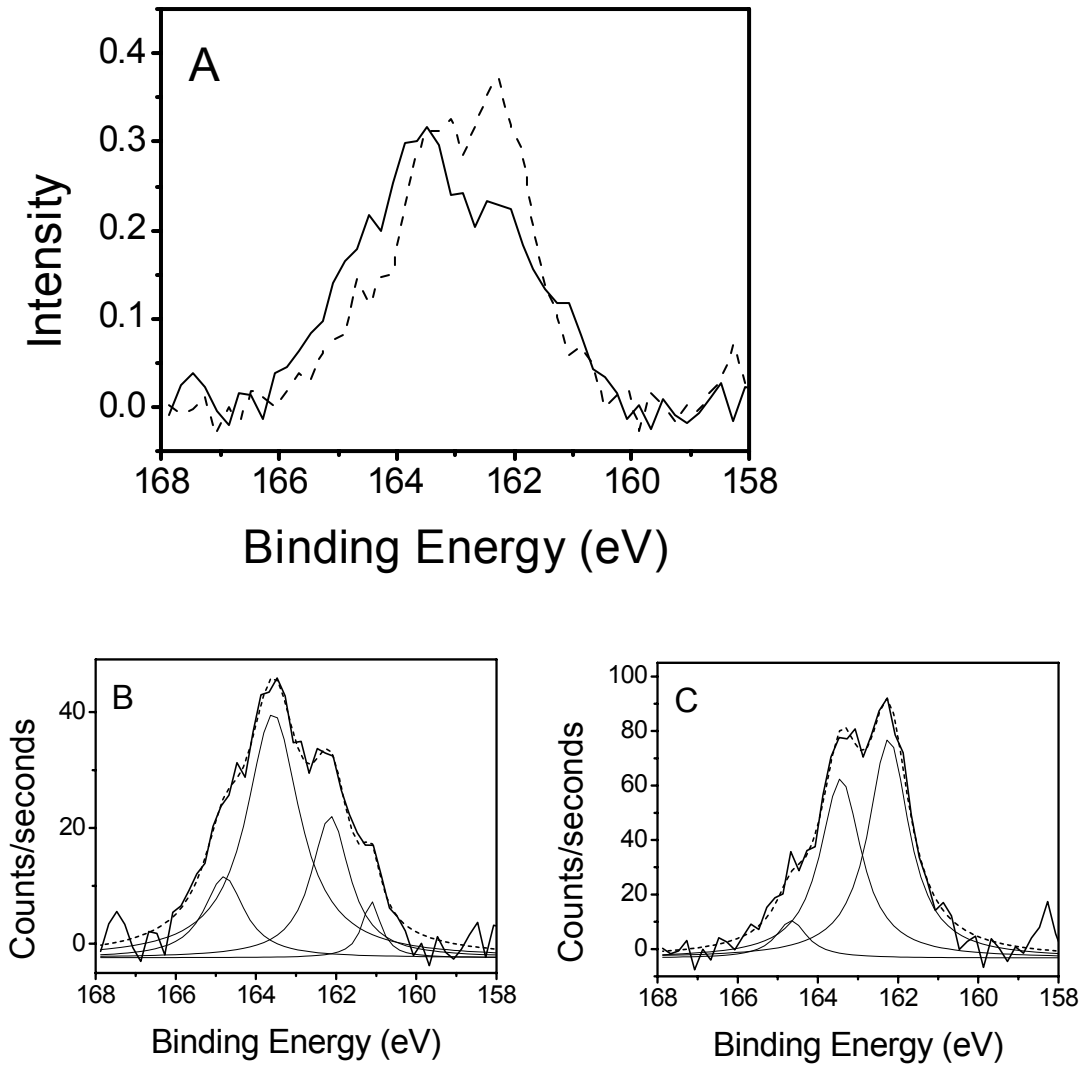


**Figure 5.5**: A) XPS spectrum of YCC (fully drawn) and HHCC (dashed). Sulfur 2p binding energy range. Acquired at 25.00 eV pass energy. 370 (YCC) and 350 (HHCC) sweeps, 25 seconds pr. sweep. The spectra are normalized by area to ease comparison. B) Fits of YCC and C) HHCC spectrum by Lorentzian curves. The XPS spectra are fully drawn, while the fitted curves are dashed. The individual Lorentzian curves are fully drawn.

The carbon signal

The carbon signal contains a peak at 286 eV, which is attributed to $sp^3$-hybridised carbon (Fig. 5.6). The shoulder at 288.5 eV stems from carbonyl. From the measurements it seems that YCC contains a larger amount of carbonyl due to its

resemblance to the carbon spectra of L-cysteine (not shown). The carbonyl peak is more pronounced. However, a measurement of YCC for prolonged time shows, that the carbonyl peak is attenuated in time, most likely due to radiation damage. Overall the carbon peak is broader for HHCC than for YCC.

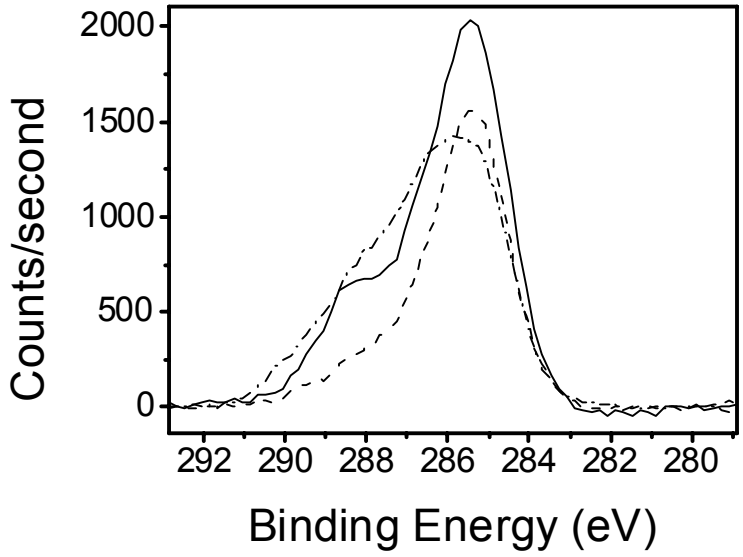


**Figure 5.6**: XPS spectra of YCC (fully drawn), YCC after prolonged radiation time (dashed) and HHCC (dot-dashed). Carbon 1s binding energy range. Acquired at 25.00 eV pass energy. 50 (YCC) and 60 (HHCC) sweeps, 35 seconds pr. sweep.

The nitrogen signal

The nitrogen signals for YCC and HHCC both contain a main peak at 400 eV (Fig. 5.7). In addition the HHCC signal contains a shoulder at 401 eV. As peptide nitrogen composes 2/3 of the total nitrogen in cyt *c* the signal at 400 eV must come from peptide nitrogen.The nitrogen signal is generally shifted positively by up to 6 eV by the presence of bound oxygen [Wagner,78]. Two amino acids, glutamine and asparagine, contain nitrogen bound to carbonyl carbon, which would shift the signal by a smaller amount. YCC contains nine and HHCC contains eight of these amino acids, which amounts to 5.4 % and 5.8 % of the total amount of nitrogen in the proteins, respectively. Two peaks separated by 1 eV, where one peak constitutes 5 % in area of the other will hardly be distinguishable from one single peak. A fit of the curve in Fig. 5.7 shows that

it is fitted best by two Lorentzian curves centered at 401.1 and 400.0 eV. The Lorentzian at 401.1 eV constitutes 40 % of the total area. Hence the higher resolution of the nitrogen peak must be due to different degrees of unfolding of the two cyt *c*'s.

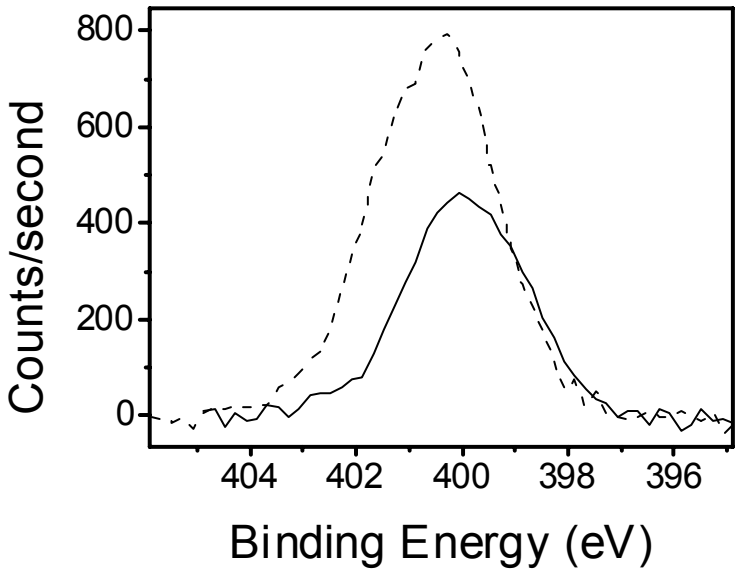


**Figure 5.7**: XPS spectra of YCC (fully drawn) and HHCC (dashed). Nitrogen 1s binding energy range. Acquired at 25.00 eV pass energy. 50 (YCC) and 61 (HHCC) sweeps, 27.5 seconds pr. sweep.

The oxygen signal

The oxygen signal is a single peak at 532 eV for YCC and at 533 eV for HHCC (Fig. 5.8). The difference could reflect a different degree of unfolding of YCC and HHCC. The deviation is not due to lack of calibration as all signals have been calibrated against the Au 4f line at 84 eV. The HHCC peak is 2.6 eV wide; the YCC peak slightly broader 3.6 eV. The width of the peaks indicates, that several oxygen species are present in both YCC and HHCC. The individual peaks can, however, not be resolved.

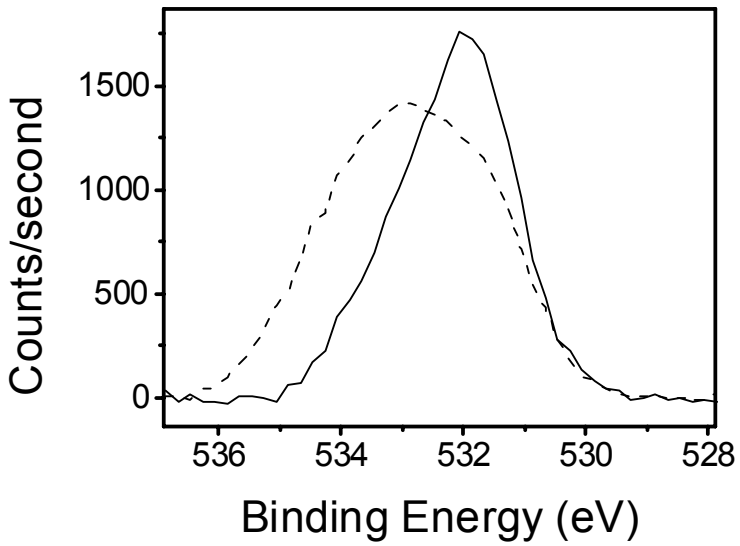


**Figure 5.8**: XPS spectra of YCC (fully drawn) and HHCC (dashed). Oxygen 1s binding energy range. Acquired at 25.00 eV pass energy. 58 (YCC) and 60 (HHCC) sweeps, 22.5 seconds pr. sweep.

The gold signal

Two intense peaks at 84.0 and 87.7 eV originate from the Au $4f_{5/2}$ and $4f_{7/2}$ orbitals (Fig. 5.9). The size of the gold signal clearly depends on the amount of material adsorbed on the gold. The gold signal is highest for cleaned gold with no adsorbed material, slightly lower when the small molecule L-cysteine is adsorbed, and lowest when large molecules such as YCC and HHCC are adsorbed. Interestingly, the gold signal is lower for adsorbed YCC than for HHCC, which would indicate a higher coverage.

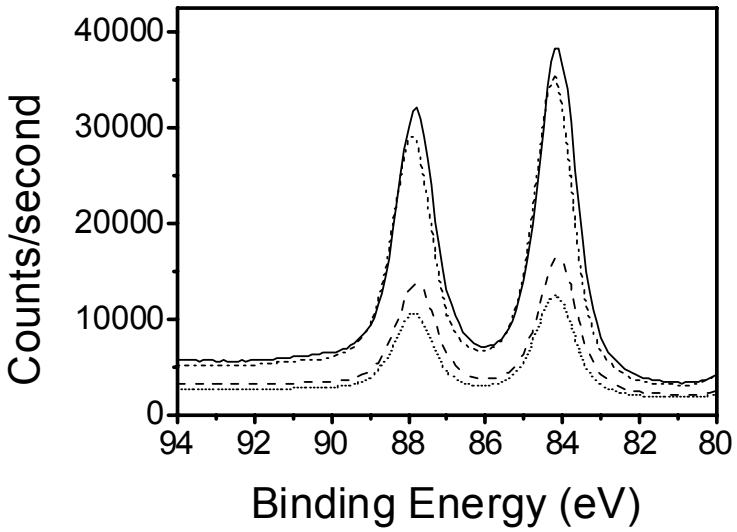


**Figure 5.9**: XPS spectra of YCC (dotted) and HHCC (dashed) and L-cysteine (short-dashed) and cleaned gold (full). Gold 4f binding energy range. Acquired at 25.00 eV pass energy. 13 (YCC), 17 (HHCC), and 13 (L-cysteine) sweeps, 35 seconds pr. sweep.

The iron signal

A peak in the YCC spectrum was visible at 710 eV (Fig. 5.10), but it could not be resolved due to the low atomic concentration. This is not surprising since YCC and HHCC contain only one iron atom. The HHCC spectrum did not contain a regular peak but the presence of a step in the spectra at 710 eV indicates, however, that the sample contains iron in the oxidized form [Boeckl,00]. In addition to the photoelectrons released at the characteristic kinetic energy of a given element, a 'tail' of photoelectrons, which have been slowed down in the passage of the monolayer, is detected. The kinetic energy of these photoelectrons is not quantized as the unperturbed photoelectrons, but equally distributed on all lower kinetic energies. The lower kinetic energy is interpreted as a higher binding energy according to eq. (5.1) and thus appears as a step in the XPS spectra. A step is hence characteristic of a new element.

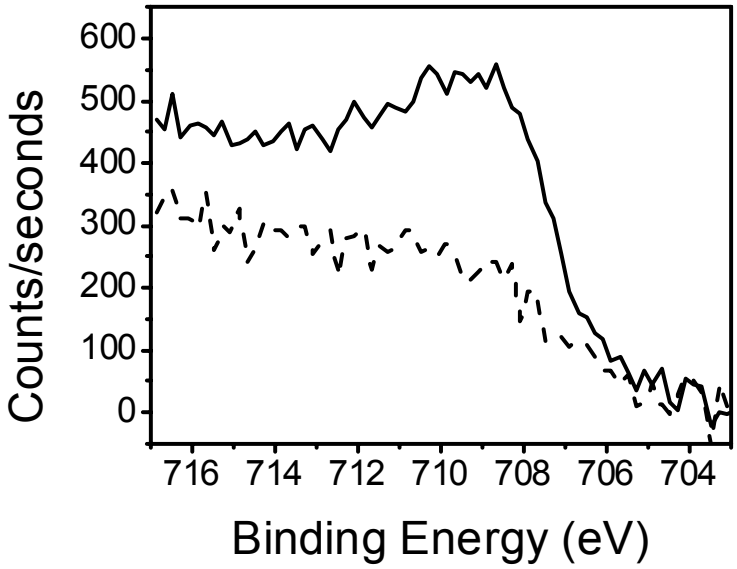


**Figure 5.10**: XPS spectra of YCC (fully drawn) and HHCC (dashed). Iron $2p_{3/2}$ binding energy range. Acquired at 50.00 eV pass energy. 200 (YCC) and 70 (HHCC) sweeps, 35 seconds pr. sweep.

### 5.2.4 Conclusion

The XPS measurements confirmed that YCC, HHCC and L-cysteine all form gold-thiolate bonds. Surprisingly, the percentage of sulfur forming gold-thiolate bond was higher in HHCC (90±7%) than in YCC (63±22%). L-cysteine formed exclusively gold-thiolate bonds. Thus it could not be confirmed that YCC binds to Au(111) exclusively via Cys102, but rather via several sulfurs. It was revealed that adsorbed YCC contains more sulfur species, which could be interpreted as a higher degree of unfolding. Likewise the coverage of YCC was found to be higher than for HHCC.

# 6 Appendix A: Bibliography


Adams JM, Evans S, Reid PI, Thomas JM, Walters MJ, *Quantitative-Analysis Of Aluminosilicates And Other Solids By X-Ray Photoelectron-Spectroscopy*, Anal. Chem. 49 (13) (1977) 2001-2008.

Andersen JET, Møller P, Pedersen MV, Ulstrup J, *Cytochrome c dynamics at gold and glassy carbon surfaces monitored by in situ scanning tunnel microscopy*, Surf. Sci. 325 (1995) 193-205.

Andersen JET, Olesen KG, Danilov AI, Foverskov CE, Møller P, Ulstrup J, *Covalently immobilised cytochrome c imaged by in situ scanning microscopy*, Bioelec. Bioenerg. 44 (1997) 57-63.

Andersen NH, Nørgaard A, Jensen TJ, Ulstrup J, *Sequential unfolding of the two-domain protein Pseudomonas stutzeri cytochrome $c_4$*, J. Inorg. Biochem. 88 (2002) 316-327.

Anderson LJ, Richardson DJ, Butt JN, *Catalytic protein film voltammetry from a respiratory nitrate reductase provides evidence for complex electrochemical modulation of enzyme activity*, Biochemistry 40 (38) (2001) 11294-11307.

Aoki K, Tokuda K, Matsuda H, *Theory of Differential Pulse Voltammetry at Stationary Planar Electrodes*, J. Electroanal. Chem. 175 (1-2) (1984) 1-13.

Armstrong FA, Hill HAO, Walton NJ, *Direct Electrochemistry Of Redox Proteins*, Accounts Chem Res 21 (11) (1988) 407-413.

Armstrong FA, Heering HA, Hirst J, *Reactions of complex metalloproteins studied by protein-film voltammetry*, Chem. Soc. Rev. 26 (3) (1997) 169-179.

Armstrong FA, Wilson GS, *Recent developments in faradaic bioelectrochemistry*, Electrochim. Acta. 45 (15-16) (2000) 2623-2645.

Avila A, Gregory BW, Niki K, Cotton TM, *An electrochemical approach to investigate gated electron transfer using a physiological model system: Cytochrome c immobilized on carboxylic acid-terminated alkanethiol self-assembled monolayers on gold electrodes*, J. Phys. Chem. B 104 (12) (2000) 2759-2766.

Bain CD, Troughton EB, Tao Y-T, Evall J, Whitesides GM, Nuzzo RG, *Formation of Monolayer Films by the Spontaneous Assembly of Organic Thiols from Solution onto Gold*, J. Am. Chem. Soc. 111 (1989A) 321-335.

Bain CD, Biebuyck HA, Whitesides GM, *Comparison of Self-Assembled Monolayers on Gold: Coadsorption of Thiols and Disulfides*, Langmuir 5 (1989B) 723-727.

Baird RJ, Fadley CS, Kawamoto SK, Mehta M, Alvarez R, Silva JA, *Concentration Profiles For Irregular Surfaces From X-Ray Photoelectron Angular-Distributions*, Anal. Chem. 48 (6) (1976) 843-846 .

Balashev K, Nielsen LK, Callisen TH, Svendsen A, Bjørnholm T, *In Situ Studies of Single Enzymes and Enzyme Kinetics by Atomic Force Microscopy (AFM)*, Probe Micros. 2 (2) (2001) 177-185.

Baller MK, Lang HP, Fritz J, Gerber C, Gimzewski JK, Drechsler U, Rothuizen H, Despont M, Vettiger P, Battiston FM, Ramseyer JP, Fornaro P, Meyer E, Güntherodt H-J, *A cantilever array-based artificial nose*, Ultramicroscopy 82 (2000) 1-9.

Bard AJ, Faulkner LR. *Electrochemical Methods*. Publish. John Wiley & Sons, Inc., New York, N.Y., USA (1980).

Bashir R, *DNA-mediated artificial nanobiostructures: state of the art and future directions*, Superlattice Microst. 29 (1) (2001) 1-16.

Battistuzzi G, Borsari M, Cowan JA, Ranieri A, Sola M, *Control of Cytochrome c Redox Potential: Axial Ligation and Protein Environment Effects*, J. Am. Chem. Soc. 124 (2002) 5315-5324.

Berger R, Gerber C, Gimzewski JK, Meyer E, Güntherodt HJ, *Thermal analysis using a micromechanical calorimeter*, Appl. Phys. Lett. 69 (1) (1996) 40-42.

Berger R, Gerber C, Lang HP, Gimzewski JK, *Micromechanics: A Toolbox for Femtoscale Science: 'Towards a Laboratory on a Tip'*, Microelectron. Eng. 35 (1997A) 373-379.

Berger R, Delamarche E, Lang HP, Gerber C, Gimzewski JK, Meyer E, Güntherodt HJ, *Surface stress in the self-assembly of alkanethiols on gold*, Science 276 (1997B) 2021-2024.

Berger R, Lang HP, Gerber C, Gimzewski JK, Fabian JH, Scandella L, Meyer E, Güntherodt H-J, *Micromechanical thermogravimetry*, Chem. Phys. Lett 294 (1998A) 363-369.

Berger R, Delamarche E, Lang HP, Gerber C, Gimzewski JK, Meyer E, Güntherodt HJ, *Surface stress in the self-assembly of alkanethiols on gold probed by a force microscopy technique*, Appl. Phys. A 66 (1998B) 55-59.

Berman HM, Westbrook J, Feng Z, Gilliland G, Bhat TN, Weissig H, Shindyalov IN, Bourne PE, *The Protein Data Bank*, Nucleic Acids Res., 28 (2000) 235-242.

Binnig G, Rohrer H, Gerber C, Weibel E, *Surface Studies By Scanning Tunneling Microscopy*, Phys. Rev. Lett. 49 (1) (1982) 57-61.

Binnig G, Quate CF, Gerber C, *Atomic Force Microscope*, Phys. Rev. Lett. 56 (9) (1986) 930-933.

Bockris JO, Reddy AKN, *Modern Electrochemistry*, vol. 2, Plenum Publishing Corporation. New York, N.Y., USA (1970).

Boeckl MS, Bramblett AL, Hauch KD, Sasaki T, Ratner BD, Rogers JW, *Self-Assembly of Tetraphenylporphyrin Monolayers on Gold Substrates*, Langmuir 16 (2000) 5644-5653.

Boisen A, *Passive & Active AFM Probes: design, fabrication & characterization*, Ph.D. thesis, Mikroelektronik Centret, Technical University of Denmark (1997).

Boisen A, Thaysen J, Jensenius H, Hansen O, *Environmental sensors based on micromachined cantilevers with integrated read-out*, Ultramicroscopy 82 (2000) 11-16.

Bousse LJ, Mostarshed S, Hafeman D, *Combined measurement of surface potential and zeta potential at insulator/electrolyte interfaces*, Sensor. Actuat. B 10 (1992) 67-71.

Bramblett AL, Boeckl MS, Hauch KD, Ratner BD, Sasaki T, Rogers JW, *Determination of surface coverage for tetraphenylporphyrin monolayers using ultraviolet visible absorption and x-ray photoelectron spectroscopies*, Surf. Int. Anal. 33 (2002) 506-515.

Brash JL, Horbett TA, *Proteins at Interfaces II. Fundamentals and Applications*, American Chemical Society Symposium Series 602, American Chemical Society, Washington DC (1995).

Brask J, Wackerbarth H, Jensen KJ, Zhang JD, Nielsen JU, Andersen JET, Ulstrup J, *Monolayers of a de novo designed 4-alpha-helix bundle carboprotein and partial structures on Au(111)-surfaces*, Bioelectrochemistry 56 (1-2) (2002) 27-32.

Brito R, Rodríguez, Figueroa J, Cabrera CR, *Adsorption of 3-mercaptopropyltrimethoxysilane and 3-aminopropyltrimethoxysilane at platinum electrodes*, J. Electroanal. Chem. 520 (2002) 47-52.

Brizzolara RA, Boyd JL, Tate AE, *Evidence for covalent attachment of purple membrane to a gold surface via genetic modification of bacteriorhodopsin*, J. Vac. Sci. Technol. A 15 (3) (1997) 773-778.

Burestedt E, Narvaez A, Ruzgas T, Gorton L, Emnéus J, Dominguez E, MarkoVarga G, *Rate-limiting steps of tyrosinase-modified electrodes for the detection of catechol*, Anal. Chem. 68 (9) (1996) 1605-1611.

Castner DG, Hinds K, Grainger DW, *X-ray Photoelectron Spectroscopy Sulfur 2p Study of Organic Thiol and Disulfide Binding Interactions with Gold Surfaces*, Langmuir 12 (1996) 5083-5086.

Cavalleri O, Oliveri L, Daccà A, Parodi R, Rolandi R, *XPS measurements on L-cysteine and 1-octadecanethiol self-assembled films: a comparative study*, Appl. Surf. Sci. 176-176 (2001) 357-362.

Chen CJ, *Introduction to Scanning Tunneling Microscopy*, Oxford University Press, New York, USA (1993).

Chen LW, Haushalter KA, Lieber CM, Verdine GL, *Direct visualization of a DNA glycosylase searching for damage*, Chem. Biol. 9 (3) (2002) 345-350.

Chi QJ, Zhang JD, Friis EP, Andersen JET, Ulstrup J, *Electrochemistry of self-assembled monolayers of the blue copper protein Pseudomonas aeruginosa azurin on Au(111)*, Electrochem. Commun. 1 (3-4) (1999) 91-96.

Chi QJ, Zhang JD, Nielsen JU, Friis EP, Chorkendorff I, Canters GW, Andersen JET, Ulstrup J, *Molecular monolayers and interfacial electron transfer of Pseudomonas aeruginosa azurin on Au(111)*, J. Am. Chem. Soc. 122 (17) (2000) 4047-4055.

Chi QJ, Zhang JD, Andersen JET, Ulstrup J, *Ordered assembly and controlled electron transfer of the blue copper protein azurin at gold (111) single-crystal* substrates, J. Phys. Chem B 105 (20) (2001) 4669-4679.

Chorkendorff I, *The XPS and AES methods for surface analysis in material science*, Physics Department, Technical University of Denmark, Lyngby, Denmark (1994).

Clemmer DE, Hudgins RR, Jarrold MF, *Naked Protein Conformations: Cytochrome c in the Gas Phase*, J. Am. Chem. Soc. 117 (1995) 10141-10142.

Clot O, Wolf MO, *Spontaneous Adsorption of 4-Ferrocenylphenyl Isocyanide and 11-Mercaptoundecanoyl Ferrocene on Chromium*, Langmuir 15 (1999) 8549-8551.

Dakkouri AS, Kolb DM, Edelstein-Shima R, Mandler D, *Scanning Tunneling Microscopy Study of L-Cysteine on Au(111)*, Langmuir 12 (1996) 2849-2852.

Danilov AI, *Scanning tunnelling and atomic force microscopy in the electrochemical of surfaces*, Russ. Chem. Rev., 64 (8) (1995) 767-781.

Dannenberger O, Buck M, Grunze M, *Self-Assembly of n-Alkanethiols: A Kinetic Study by Second Harmonic Generation*, J. Phys. Chem. B 103 (1999) 2202-2213.

Davis JJ, Hill HAO, Bond AM, *The application of electrochemical scanning probe microscopy to the interpretation of metalloprotein voltammetry*, Coordin. Chem. Rev. 200 (2000A) 411-442.

Davis JJ, Djuricic D, Lo KKW, Wallace ENK, Wong LL, Hill HAO, *A scanning tunnelling study of immobilised cytochrome P450(cam)*, Faraday Discuss. 116 (2000B) 15-22.

Davis JJ, Hill HAO, *The scanning probe microscopy of metalloproteins and metalloenzymes*, Chem. Commun. 5 (2002) 393-401.

Delamarche E, Michel B, *Structure and stability of self-assembled monolayers*, Thin Solid Films 273 (1996) 54-60.

Diao P, Jiang D, Cui X, Gu D, Tong R, Zhong B, *Studies of structural disorder of self-assembled thiol monlayers on gold by cyclic voltammetry and ac impedance*, J. Electroanal. Chem. 464 (1999) 61-67.

Djuricic D, Hill HAO, Lo KK-W, Wong L-L, *A scanning tunneling microscopy (STM) investigation of complex formation between cytochrome $P450_{cam}$ and putidaredoxin*, J. Inorg. Biochem.88 (2002) 362-367.

Dong SJ, Niu JJ, Cotton TM, *Ultraviolet-Visible Spectroelectrochemistry Of Redox Proteins*, Method. Enzymol. 246 (1995) 701-732.

Eberhardt A, Fenter P, Eisenberger P, *Growth kinetics in self-assembling monolayers: a unique adsorption mechanism*, Surf. Sci. 397 (1998) L285-L290.

Eddowes MJ, Hill HAO, *Electrochemistry Of Horse Heart Cytochrome-C*, J. Am. Chem. Soc. 101 (16) (1979) 4461-4464.

Eggins BR, *Chemical Sensors and Biosensors*, Wiley, Chichester (2002).

Enderlein J, *A theoretical investigation of single-molecule fluorescence detection on thin metallic layers*, Biophys. J. 78 (4) (2000) 2151-2158.

Evans SD, Ulman A, *Surface potential studies of alkyl-thiol monolayers adsorbed on gold*, Chem. Phys. Lett. 170 (1990) 462-466.

Regisser F, Lavoie M-A, Champagne GY, Bélanger D, *Randomly oriented graphite electrode. Part 1. Effect of electrochemical pretreatment on the electrochemical behaviorvand chemical composition of the electrode*, J. Electroanal. Chem. 415 (1996) 47-54.

Facci P, Alliata D, Andolfi L, Schnyder B, Kotz R, *Formation and characterization of protein monolayers on oxygen-exposing surfaces by multiple-step self-chemisorption*, Surf. Sci. 504 (1-3) (2002) 282-292.

Farver O, Zhang JD, Chi QJ, Pecht I, Ulstrup J, *Deuterium isotope effect on the intramolecular electron transfer in Pseudomonas aeruginosa azurin*, P. Natl. Acad. Sci. USA 98 (8) 82001) 4426-4430.

Feinberg BA, Liu X, Ryan MD, Schejter A, Zhang C, Margoliash E, *Direct Voltammetric Observation of Redox Driven Changes in Axial Coordination and Intramolecular Rearrangement of the Phenylalanine-82-Histidine Variant of Yeast Iso-1-cytochrome c*, Biochemistry 37 (1998) 13091-13101.

Finklea HO, *Electrochemistry of organized monolayers of thiols and related molecules on electrodes*, Electroanal. Chem. 19 (1996) 109-335.

Friis EP, Andersen JET, Madsen LL, Møller P, Ulstrup J, *In situ STM and AFM of the copper protein Pseudomonas aeruginosa azurin*, J. Electroanal. Chem. 431 (1) (1997) 35-38.

Friis EP, Andersen JET, Kharkats YI, Kuznetsov AM, Nichols RJ, Zhang JD, Ulstrup J, *An approach to long-range electron transfer mechanisms in metalloproteins: In situ scanning tunneling microscopy with submolecular resolution*, P. Natl. Acad. Sci. USA 96 (4) (1999A) 1379-1384.

Friis E, *Scanning Probe Investigations of Adsorbed Proteins on Metal Surfaces*, PhD thesis, Department of Chemistry, Technical University of Denmark (1999B).

Fristrup P, Grubb M, Zhang J, Christensen HEM, Hansen AM, Ulstrup J, *Voltammetry of native and recombinant Pseudomonas aeruginosa azurin on polycrystalline Au- and single-crystal Au(111)-surfaces modified by decanethiol monolayers*, J. Electroanal Chem 511 (1-2) (2001) 128-133.

Fritz J, Baller MK, Lang HP, Rothuizen H, Vettiger P, Meyer E, Güntherodt H-J, Gerber C, Gimzewski JK, *Translating Biomolecular Recognition into Nanomechanics*, Science 288 (2000) 316-318.

Fujihira M, Okabe Y, Tani Y, Furugori M, Akiba U, *A novel cleaning method of gold-coated atomic force microscope tips for their chemical modification*, Ultramicroscopy 82 (2000) 181-191.

Gaigalas AK, Niaura G, *Measurement of electron transfer rates between adsorbed azurin and a gold electrode modified with a hexanethiol layer*, J. Colloid. Interf. Sci. 193 (1) (1997) 60-70.

Gilardi G, Fantuzzi A, *Manipulating redox systems: application to nanotechnology*, Trends Biotechnol. 19 (11) (2001) 468-476.

Gimzewski JK, Gerber C, Meyer E, Schlittler RR, *Observation Of A Chemical-Reaction Using A Micromechanical Sensor*, Chem. Phys. Lett. 217 (5-6) (1994) 589-594.

Giz MJ, Duong B, Tao NJ, *In situ STM study of self-assembled mercaptopropionic acid monolayers for electrochemical detection of dopamine*, J. Electroanal. Chem. 465 (1999) 72-79.

Gold JM, Schmidt M, Steinemann SG, *XPS Study of Amino Acid Adsorption to Titanium Surfaces*, Helv. Phys. Acta 62 (1989) 246-249.

Green RJ, Frazier RA, Shakesheff KM, Davies MC, Roberts CJ, Tendler SJB, *Surface plasmon resonance analysis of dynamic biological interactions with biomaterials*,

Biomaterials 21 (18) (2000) 1823-1835.

Hagenström H, Schneeweiss MA, Kolb DM, *Modification of a Au(111) Electrode with Ethanethiol. 1. Adlayer Structure and Electrochemistry*, Langmuir 15 (1999) 2435-2443.

Hagleitner C, Hierlemann A, Lange D, Kummer A, Kerness N, Brand O, Baltes H, *Smart single-chip gas sensor microsystem*, Nature 414 (2001) 293-296.

Hamelin A, *Cyclic Voltammetry at gold single-crystal surfaces*, J. Electroanal. Chem. 407 (1996) 1-11.

Hansen KM, Ji H-F, Wu G, Datar R, Cote R, Majumdar A, Thundat T, *Cantilever-Based Optical Deflection Assay for Discrimination of DNA Single-Nucleotide Mismatches*, Anal. Chem. 73 (2001) 1567-1571.

Heering HA, Weiner JH, Armstrong FA, *Direct detection and measurement of electron relays in a multicentered enzyme: Voltammetry of electrode-surface films of E-coli fumarate reductase, an iron-sulfur flavoprotein*, J. Am. Chem. Soc. 119 (48) (1997)11628-11638.

Heffron K, Leger C, Rothery RA, Weiner JH, Armstrong FA, *Determination of an optimal potential window for catalysis by E-coli dimethyl sulfoxide reductase and hypothesis on the role of Mo(V) in the reaction pathway*, Biochemistry 40 (10) (2001)3117-3126.

Hianik T (ed.), *Proc. XVIth Int. Symp. on Bioelectrochemistry and Bioenergetics*, Bioelectrochemistry 55 (1-2) (2002) 1-181, Bioelectrochemistry 56 (1-2) (2002) 1-236.

Hirst J, Duff JLC, Jameson GNL, Kemper MA, Burgess BK, Armstrong FA, *Kinetics and mechanism of redox-coupled, long-range proton transfer in an iron-sulfur protein. Investigation by fast-scan protein-film voltammetry*, J. Am. Chem. Soc. 120 (28) (1998) 7085-7094.

Hobara D, Imabayashi S, Kakiuchi T, *Preferential Adsorption of Horse Heart Cytochrome c on Nanometer-Scale Domains of a Phase-Separated Binary Self-Assembled Monolayer of 3-Mercaptopropionic Acid and 1-Hexadecanethiol on Au(111)*, Nano Lett. 2 (9) (2002) 1021-1025.

Hösler W, Behm RJ, Ritter E, *Defects On The Pt(100) Surface And Their Influence On Surface-Reactions - A Scanning Tunneling Microscopy Study*, IBM J. Res. Dev. 30 (4) (1986) 403-410.

Hubbard AT, Anson FC, *The Theory and Practice of Electrochemistry with Thin Layer Cells* in Electroanalytical Chemistry, Volume 4, ed. Bard AJ 129-214, Marcel Dekker, Inc. New York (1970).

Imabayashi S, Iida M, Hobara D, Feng ZQ, Niki K, Kakiuchi T, *Reductive desorption of carboxylic-acid-terminated alkanethiol monolayers from Au(111) surfaces*, J. Electroanal. Chem. 428 (1997) 33-38.

Ion A, Banica FG, *Direct electrochemistry of bovine heart cytochrome c facilitated by cysteine derivatives and analogues. Some effects of facilitator structure*, J. Solid State Electrochem. 5 (2001) 431-436.

Jensenius H, Thaysen J, Rasmussen AA, Veje LH, Hansen O, Boisen A, *A microcantilever-based alcohol vapor sensor-application and response model*, Appl. Phys. Lett. 76 (2000) 2615-2617.

Jeuken LJC, Jones AK, Chapman SK, Cecchini G, Armstrong FA, *Electron-transfer mechanisms through biological redox chains in multicenter enzymes*, J. Am. Chem. Soc. 124 (20) (2002) 5702-5713.

Jiang L, Glidle A, Griffith A, McNeil CJ, Cooper JM, *Characterising the formation of a bioelectrochemical interface at a self-assembled monolayer using X-ray photoelectron spectroscopy*, Bioelec. Bioenerg. 42 (1997) 15-23.

Kasemo B, *Biological surface science*, Surf. Sci. 500 (1-3) (2002) 656-677.

Kerkhof FPJM, Moulijn JA, *Quantitative-Analysis Of XPS Intensities For Supported Catalysts*, J. Phys. Chem. 83 (12) (1979) 1612-1619.

Khomutov GB, Belovolova LV, Khanin VV, Soldatov ES, Trifonov AS, *STM investigation of electron transport features in cytochrome c Langmuir-Blodgett films*, Colloid. Surface. A 198-200 (2002) 745-752.

Kim BH, Prins FE, Kern DP, Raible S, Weimar U, *Multicomponent analysis and prediction with a cantilever array based gas sensor*, Sensor. Actuat. B 78 (2001) 12-18.

Kolb DM, Dakkouri AS, Batina N, *Nanoscale Probes of the Solid/Liquid Interface*, p. 263-284, eds. Gewirth AA, Siegenthaler H, Kluwer Academic Press, Dordrecht (1995).

Komar-Panicucci S, Weis D, Bakker G, Qiao T, Sherman F, McLendon G, *Thermodynamics of the Equilibrium Unfolding of Oxidized and Reduced Saccharomyces cerevisiae Iso-1-cytochromes c*, Biochemistry 33 (1994) 10556-10560.

Kondo T, Yanagida M, Shimazu K, Uosaki K, *Determination of Thickness of a Self-Assembled Monolayer of Dodecanethiol on Au(111) by Angle-Resolved X-ray Photoelectron Spectroscopy*, Langmuir 14 (1998) 5656-5658.

Kraulis PJ, *Molscript - A Program To Produce Both Detailed And Schematic Plots Of Protein Structures*, J. Appl. Crystallogr. 24 (1991) 946-950.

Kuznetsov AM, Sommer-Larsen P, Ulstrup J, *Resonance And Environmental Fluctuation Effects In STM Currents Through Large Adsorbed Molecules*, Surf. Sci. 275 (1-2) (1992) 52-64.

Kuznetsov AM, Ulstrup J, *Mechanisms of in situ scanning tunnelling microscopy of organized redox molecular assemblies*, J. Phys. Chem. A 104 (49) (2000) 11531-11540.

Kuznetsov AM, Ulstrup J, *Theory of Interfacial Electron Transfer and in situ Scanning Tunnelling Microscopy of Redox Molecules*, Probe Micros. 2 (2) (2001) 187-202.

Kuznetsov AM, Ulstrup J, *Mechanisms of molecular electronic rectification through electronic levels with strong vibrational coupling*, J. Chem. Phys. 116 (5) (2002) 2149-2165.

Lang HP, Baller MK, Berger R, Gerber C, Gimzewski JK, Battiston FM, Fornaro P, Ramseyer JP, Meyer E, Güntherodt HJ, *An artificial nose based on a micromechanical cantilever array*, Anal. Chim. Acta 393 (1999A) 59-65.

Lang HP, Baller MK, Battiston FM, Fritz J, Berger R, Ramseyer JP, Fornaro P, Meyer E, Güntherodt HJ, Brugger J, Dreschler U, Rothuizen H, Despont M, Vettiger P, Gerber C, Gimzewski JK,. *The Nanomechanical NOSE*. Proceedings of the IEEE Micro Electro Mechanical Systems (MEMS) (1999B) 9-13.

Lasic DD, *Liposomes: From Physics to Applications*, 2nd ed., Elsevier, Amsterdam (1995).

Lavrik NV, Tipple CA, Sepaniak MJ, Datskos PG, *Enhanced chemi-mechanical transduction at nanostructured interfaces*, Chem. Phys. Lett. 336 (2001) 371-376.

Leger C, Heffron K, Pershad HR, Maklashina E, Luna-Chavez C, Cecchini G, Ackrell BAC, Armstrong FA, *Enzyme electrokinetics: Energetics of succinate oxidation by fumarate reductase and succinate dehydrogenase*, Biochemistry 40 (37) (2001) 11234-11245.

Liao J-D, Wang MC, Weng CC, Klauser R, Frey S, Zharnikov M, Grunze M, *Modification of Alkanethiolate Self-Assembled Monolayers by Free Radical-Dominant Plasma*, J. Phys. Chem. B 106 (2002) 77-84.

Lenigk R, Carles M, Ip NY, Sucher NJ, *Surface characterization of a silicon-chip-based DNA microarray*, Langmuir 17 (8) (2001) 2497-2501.

Louie GV, Brayer GD, *High-resolution refinement of yeast iso-1-cytochrome c and comparisons with other eukaryotic cytochromes c*, J. Mol. Biol. 214 (2) (1990) 527-555.

Maret W, Heffron G, Hill HAO, Djuricic D, Jiang LJ, Vallee BL, *The ATP/metallothionein interaction: NMR and STM*, Biochemistry 41 (5) (2002)1689-1694.

Margoliash E, Frohwirt N, *Spectrum of Horse-Heart Cytochrome c*, Biochem. J. 71 (1959) 570-578.

Marie R, Jensenius H, Thaysen J, Christensen CB, Boisen A, *Adsorption kinetics and mechanical properties of thiol-modified DNA-oligos on gold investigated by microcantilever sensors*, Ultramicroscopy 91 (2002) 29-36.

McCabe WL, Smith JC, Harriott P, *Unit Operations of Chemical Engineering*, 4th ed., p. 93, McGraw-Hill Book Company (1985).

McKendry R, Zhang J, Arntz Y, Strunz T, Hegner M, Lang HP, Baller MK, Certa U, Meyer E, Güntherodt H-J, Gerber C, *Multiple label-free biodetection and quantitative DNA-binding assays on a nanomechanical cantilever array*, P. Natl. Acad. Sci. USA 99 (15) (2002) 9783-9788.

Melville JL, Compton RG, *The simulation of Differential Pulse Voltammetry*, Electroanal. 13 (2) (2001) 123-130.

Mondal MS, Goodin DB, Armstrong FA, *Simultaneous voltammetric comparisons of reduction potentials, reactivities, and stabilities of the high-potential catalytic states of wild-type and distal-pocket mutant (W51F) yeast cytochrome c peroxidase*, J. Am. Chem. Soc. 120 (25) (1998) 6270-6276.

Moulin AM, *Development of Microcantilever Based Sensors*, Ph.D. thesis, The Department of Engineering, University of Cambridge (1998).

Moulin AM, O'Shea SJ, Welland ME, *Microcantilever-based biosensors*, Ultramicroscopy 82 (2000) 23-31.

Mukhopadhyay R, Davis JJ, Kyritsis P, Hill HAO, Meyer J, *A scanning tunnelling microscopy study of Clostridium pasteurianum rubredoxin*, J. Inorg. Biochem. 78 (3) (2000) 251-254

Murgida DH, Hildebrandt P, *Heterogeneous electron transfer of cytochrome c on coated silver electrodes. Electric field effects on structure and redox potential*, J. Phys. Chem. B 105 (8) (2001) 1578-1586.

Nall BT, *Cytochrome c Folding and Stability* in *Cytochrome c – a multidisciplinary approach*, eds. Scott RA, Mauk AG, University Science Books, Sausalito, California, USA (1996).

Nagayama K, *Protein arrays: Concepts and subjects*, Adv. Biophys. 34 (1996) 3-23.

Oellerich S, Wackerbarth H, Hildebrandt P, *Spectroscopic characterization of nonnative conformational states of cytochrome c*, J. Phys. Chem. B 106 (25) (2002) 6566-6580.

Osborn AG, Douslin DR, *Vapor Pressure Relations of 36 Sulfur Compounds Present in Petroleum*, J. Chem. Eng. Data 11 (1966) 502-509.

Pardo-Yissar V, Katz E, Willner I, Kotlyar AB, Sanders C, Lill H, *Biomaterial engineered electrodes for bioelectronics*, Faraday Discuss. 116 (2000) 119-134.

Patel N, Davies MC, Hartshorne M, Heaton RJ, Roberts CJ, Tendler SJB, Williams PM, *Immobilization of* protein *molecules onto homogeneous and mixed carboxylate-terminated self-assembled monolayers*, Langmuir 13 (24) (1997) 6485-6490.

Paz Y, Trakhtenberg S, Naaman R, *Reaction Between O(P-3) And Organized Organic Thin-Films*, J. Phys. Chem. 98 (51) (1994) 13517-13523.

Perez-Luna VH, Yang SP, Rabinovich EM, Buranda T, Sklar LA, Hampton PD, Lopez GP, *Fluorescence biosensing strategy based on energy transfer between fluorescently labeled receptors and a metallic surface*, Biosens. Bioelectron. 17 (1-2) (2002) 71-78.

Pershad HR, Duff JLC, Heering HA, Duin EC, Albracht SPJ, Armstrong FA, *Catalytic electron transport in Chromatium vinosum [NiFe]-hydrogenase: Application of voltammetry in detecting redox-active centers and establishing that hydrogen oxidation is very fast even at potentials close to the reversible H+/H-2 value*, Biochemistry 38 (28) (1999) 8992-8999.

Peterlinz KA, Georgiadis R, *In Situ Kinetics of Self-Assembly by Surface Plasmon Resonance Spectroscopy*, Langmuir 12 (1996) 4731-4740.

Radmacher M, Fritz M, Hansma HG, Hansma PK, *Direct Observation Of Enzyme-Activity With The Atomic-Force Microscope*, Science 265 (5178) (1994) 1577-1579.

Raiteri R, Grattarola M, Butt HJ, Skládal P, *Micromechanical cantilever-based biosensors*, Sensor. Actuat. B-Chem. 79 (2-3) (2001) 115-126.

Rief M, Oesterhelt F, Heymann B, Gaub HE, *Single molecule force spectroscopy on polysaccharides by atomic force microscopy*, Science 275 (5304) (1997)1295-1297.

Rosell FI, Ferrer JC, Mauk AG, *Proton-linked protein conformational switching: Definition of the alkaline conformational transition of yeast iso-1-ferricytochrome c*, J. Am. Chem. Soc. 120 (44) (1998) 11234-11245.

Sakurai T, Ikeda O, Suzuki S, *Direct Electrochemistry Of The Blue Copper Proteins Pseudoazurin, Plantacyanin, And Stellacyanin*, Inorg. Chem. 29 (23) (1990) 4715-4718.

Saterlay AJ, Foord JS, Compton RG, *Sono-cathodic stripping voltammetry of manganese at a polished boron-doped diamond electrode: application to the determination of manganese in instant tea*, Analyst 124 (12) (1999) 1791-1796.

Sautet P, *Images of Adsorbates with the Scanning Tunneling Microscope: Theoretical Approaches to the Contrast Mechanism*, Chem. Rev. 97 (1997) 1097-1116.

Sawaguchi T, Mizutani F, Yoshimoto S, Taniguchi I, *Voltammetric and in Situ STM studies on self-assembled monolayers of 4-mercaptopyridine, 2-mercaptopyridine and thiophenol on Au(111) electrodes*, Electrochim. Acta 45 (2000) 2861-2867.

Sawaguchi T, Sato Y, Mizutani F, *In situ scanning tunneling microscopy observation of self-assembled monolayers of 3-mercaptopropionic acid on Au(111) in perchloric acid solution*, J. Electroanal. Chem. 507 (1-2) (2001) 256-262.

Service RF, *Microchip arrays put DNA on the spot*, Science 282 (5388) (1998) 396-399.

Sherman F, Taber H, Campbell W, *Genetic Determination of Iso-cytochromes c in Yeast*, J. Mol. Biol. 13 (1965) 21-39.

Shipway AN, Willner I, *Electronically transduced molecular mechanical and information functions on surfaces*, Accounts Chem. Res. 34 (6) (2001) 421-432.

Sonnenfeld R, Hansma PK, *Atomic-Resolution Microscopy In Water*, Science 232 (4747) (1986) 211-213.

Storm G, Crommelin DJA, *Liposomes: quo vadis?*, Pharm. Sci. Technol. To. 1 (1) 1998 19-31.

Sucheta A, Cammack R, Weiner J, Armstrong FA, *Reversible Electrochemistry Of Fumarate Reductase Immobilized On An Electrode Surface - Direct Voltammetric Observations Of Redox Centers And Their Participation In Rapid Catalytic Electron-Transport*, Biochemistry 32 (20) (1993) 5455-5465.

Tamayo J, Humphris ADL, Malloy AM, Miles MJ, *Chemical sensors and biosensors in liquid environment based on microcantilevers with amplified quality factor*, Ultramicroscopy 86 (2000) 167-173.

Telegdi J, Shaban A, Beczner J, Keresztes ZS, Kalman E, *Novel Techniques for Corrosion Research - Biofilm Formation Controlled by Quartz Crystal Nanobalance*, Mater. Sci. Forum 289-292 (1) (1998A) 77-82.

Telegdi J, Keresztes Z, Palinkas G, Kalman E, Sand W, *Microbially influenced corrosion visualized by atomic force microscopy*, Appl. Phys. A-Mater. 66 (1998B) S639-S642.

Thaysen J, *Cantilever for Bio-Chemical Sensing Integrated in a Microliquid Handling System*, Ph.D. thesis, Mikroelektronik Centret, Technical University of Denmark (2001).

Thundat T, Chen GY, Warmack RJ, Allison DP, Wachter EA, *Vapor Detection Using Resonating Microcantilevers*, Anal. Chem. 67 (3) (1995) 519-521.

Thundat T, Maya L, *Monitoring chemical and physical changes on sub-nanogram quantities of platinum dioxide*, Surf. Sci. 430 (1999) L546-L552.

Tirrell M, Kokkoli E, Biesalski M, *The role of surface science in bioengineered materials*, Surf. Sci. 500 (1-3) (2002) 61-83.

Tromp RM, Hamers RJ, Demuth JE, *Si(001) Dimer Structure Observed With Scanning Tunneling Microscopy*, Phys. Rev. Lett. 55 (12) (1985) 1303-1306.

Tüdos AJ, Vandeberg PJ, Johnson DC, *Evaluation Of EQCM Data From A Study Of Cysteine Adsorption On Cold Electrodes In Acidic Media*, Anal. Chem. 67 (3) (1995) 552-556.

*UV-ozone photoreactor PR-100 Operating Instruction Manual*, Ultra-Violet Products, Upland, California, USA.

Wackerbarth H, Klar U, Gunther W, Hildebrandt P, *Novel time-resolved surface-enhanced (resonance) Raman spectroscopic technique for studying the dynamics of interfacial processes: Application to the electron transfer reaction of cytochrome c at a silver electrode*, Appl. Spectrosc. 53 (3) (1999) 283-291.

Wagner CD, Riggs WM, Davis LE, Moulder JF, GE Muilenberg (editor). *Handbook of X-ray photoelectron spectroscopy*. Publish. Perkin-Elmer Corporation, Physical Electronics Division. Eden Prairie, Minnesota, USA (1978).

Wälivaara B, Askendal A, Lundström I, Tengvall P, *Blood protein interactions with chromium surfaces*, J. Biomat. Sci.-Polym. E. 8 (1) (1996) 41-48.

Walczak MM, Alves CA, Lamp BD, Porter MD, *Electrochemical and X-ray photoelectron spectroscopic evidence for differences in the binding sites of alkanethiolate monolayers chemisorbed at gold*, J. Electroanal. Chem. 396 (1995) 103-114.

Weast RC, Grasselli JG, *CRC Handbook of Data on Organic Compounds*, 2nd Edition, CRC Press, Inc., Boca Raton, FL, (1989), 1.

Wei J, Liu H, Dick AR, Yamamoto H, He Y, Waldeck DH, *Direct Wiring of Cytochrome c's Heme Unit to an Electrode: Electrochemical Studies*, J. Am. Chem. Soc. 124 (2002) 9591-9599.

Widrig CA, Chung C, Porter MD, *The Electrochemical Desorption Of n-Alkanethiol Monolayers From Polycrystalline Au And Ag Electrodes*, J. Electroanal. Chem. 310 (1-2) (1991) 335-359.

Willner I, Katz E, *Integration of layered redox proteins and conductive supports for bioelectronic applications*, Angew. Chem. Int. Edit. 39 (7) (2000) 1180-1218.

Wu G, Datar RH, Hansen KM, Thundat T, Cote RJ, Majumdar A, *Bioassay of prostate-specific antigen (PSA) using microcantilevers*, Nat. Biotechnol. 19 (2001) 856-860.

Xu S, Cruchon-Dupeyrat SJN, Garno JC, Liu G-Y, Jennings GK, Yong T-H, Laibinis PE, *In situ studies of thiol self-assembly on gold from solution using atomic force microscopy*, J. Chem. Phys. 108 (1998) 5002-5012.

Yang D-F, Wilde CP, Morin M, *Electrochemical Desorption and Adsorption of Nonyl Mercaptan at Gold Single Crystal Electrode Surfaces*, Langmuir 12 (1996) 6570-6577.

Yang YW, Fan LJ, *High-Resolution XPS Study of Decanethiol on Au(111): Single Sulfur-Gold Bonding Interaction*, Langmuir 18(4) (2002) 1157-1164.

Yaropolov AI, Skorobogat'ko OV, Vartanov SS, Varfolomeyev SD, *Laccase: Properties, Catalytic Mechanism, and Applicability*, Appl. Biochem. Biotechnol. 49 (1994) 257-280.

Yeh P, Kuwana T, *Reversible Electrode-Reaction Of Cytochrome-C*, Chem. Lett. 10 (1977) 1145-1148.

Zhang JD, Chi QJ, Dong SJ, Wang EK, *In situ electrochemical scanning tunnelling microscopy investigation of structure for horseradish peroxidase and its electrocatalytic property*, Bioelectroch. Bioener. 39 (2) (1996A) 267-274.

Zhang B, Wang E, *STM Study of Cytochrome c Molecules Adsorbed on HOPG with Variable Adsorbing Conditions*, Nanobiology 04 (1996B) 85-91.

Zhang J, Chi Q, Nielsen JU, Friis EP, Andersen JET, Ulstrup J, *Two-Dimensional Cysteine and Cystine Cluster Networks on Au(111) Disclosed by Voltammetry and in Situ Scanning Tunneling Microscopy*, Langmuir 16 (2000) 7229-7237.

Zhang J, Chi Q, Kuznetsov AM, Hansen AG, Wackerbarth H, Christensen HEM, Andersen JET, Ulstrup J, *Electronic properties of functional biomolecules at metal/aqueous solution interfaces*, J. Phys. Chem. B 106 (6) (2002) 1131-1152.

Zhang J, Christensen HEM, Ulstrup J, in preparation, (2003).

Zheng JW, Zhou Q, Zhou YG, Lu TH, Cotton TM, Chumanov G, *Surface-enhanced resonance Raman spectroscopic study of yeast iso-1-cytochrome c and its mutant*, J. Electroanal. Chem. 530 (1-2) (2002) 75-81.

Zhong Q, Inniss D, Kjoller K, Elings VB, *Fractured polymer silica fiber surface studied by tapping mode atomic-force microscopy*, Surf. Sci. 290 (1-2) (1993) L688-L692.

# 7 Appendix B: Calibration

Calibration is essential for STM measurements. Piezocrystals exhibit hysterisis and need to be calibrated on a regular basis. X and Y directions should be accurate, while the z direction does not need to be as accurate since this direction is influenced by the conductivity in the tunnel gap. The STM scanner is sensitive on x, y at the nanometer or Ångström range. Normally it is recommended to calibrate the scanner by scanning Highly Oriented Pyrolytic Graphite (HOPG) in air. It is easy to achieve atomic resolution in STM images of this substrate. The closest distance between the atoms is 2.46 Å. The atoms align along three directions. The angle between these lines is ideally 120°. When images fit this criterion, the scanner is calibrated. In fact, such perfect images are difficult to obtain since even a small drift in real measurements distorts the image when the scan area is about 2-5 nm. Secondly, tip length, temperature, and environment also influence the STM images. In order to obtain the best calibration and thereby real and accurate STM data, calibration should be conducted in the same environment using the same tip length and even the same kind of sample.

Au (111) is used as substrate in the present work throughout. The theoretical Au (111) pattern is shown in Fig. B.1. Each gold atom is closely surrounded by six atoms with a 60º angle. The distance between neighbouring atoms is 2.885 Å [Kolb,95]. In the case of face centre cubic (fcc) crystals to which gold belongs, all atoms are closely packed in space in the crystal lattice. The second top layer (red, Fig. B.2) of the (111) face is the same as the first top layer (blue), but each of the atoms is sitting on the three-fold hollow site of the first top layer, as shown in Fig. B.2. Likewise each of the atoms in the third top layer (green) is sitting on the three-fold hollow site of the second top layer.

Clean Au (111) is easily reconstructed into a (22×√3) structure (herringbone) both in vacuum and in solution under potential control. This is extensively documented in the literature though the origin of this phenomenon is not totally understood. The gold atoms on the first top layer shrink 4% along the [110] direction, while the atoms on the second top layer are not changed. In this case, 23 atoms on the first top layer occupy 22 atoms space on the second top layer. A model (Fig. B.3, right) describes this reconstruction showing a pair of lines along √3 direction. A corresponding STM image

is shown below (Fig. B.3, left). This unique structure contains a periodic distance of 6.35 nm, which is close to the dimensions of proteins. By using this structure as a standard, the STM scanner is therefore easily calibrated in the same experimental condition on bare Au(111). In addition the calibration is performed on a much larger area, thereby reducing the influence of drift.

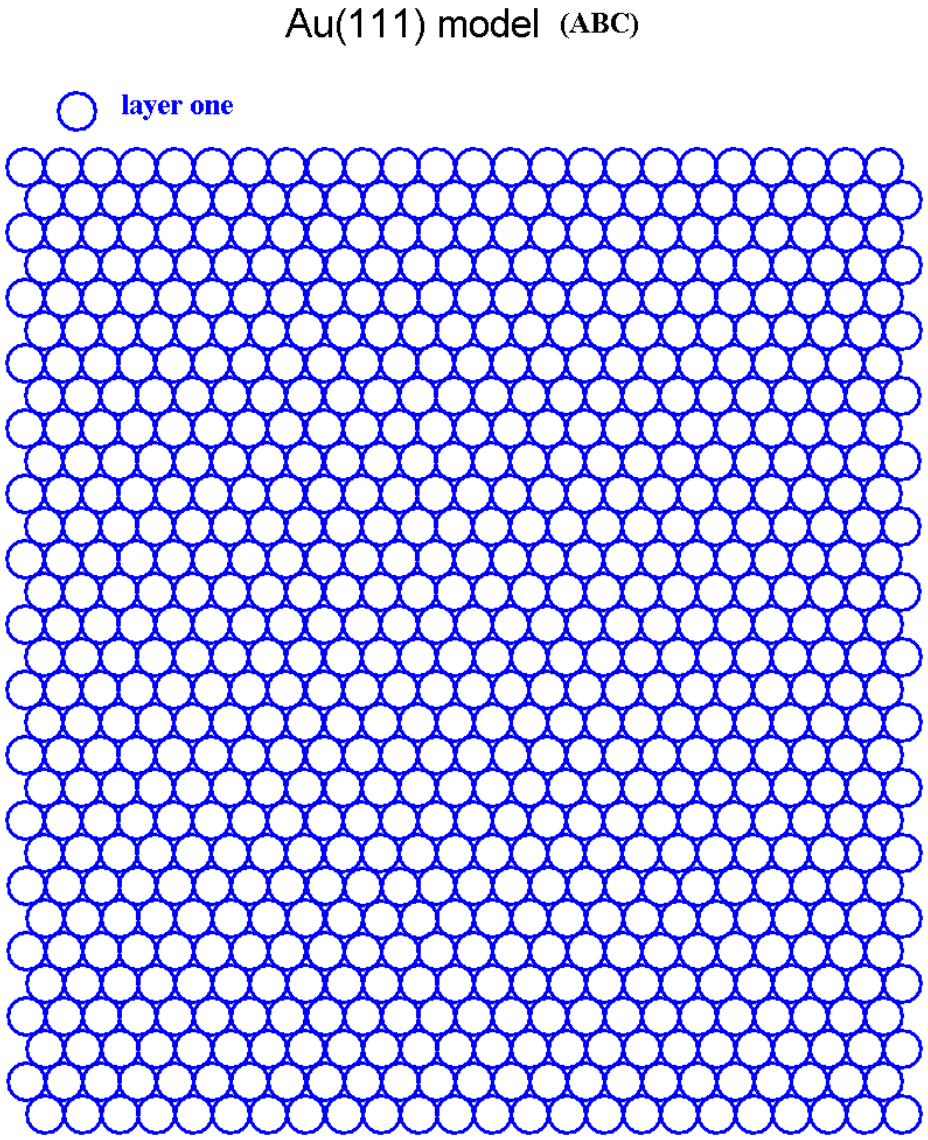


**Figure B.1**: Atomic arrangement of the top layer of an unreconstructed Au(111)-crystal. Each gold atom is closely surrounded by six atoms with a 60º angle. The distance between neighbouring atoms is 2.885 Å

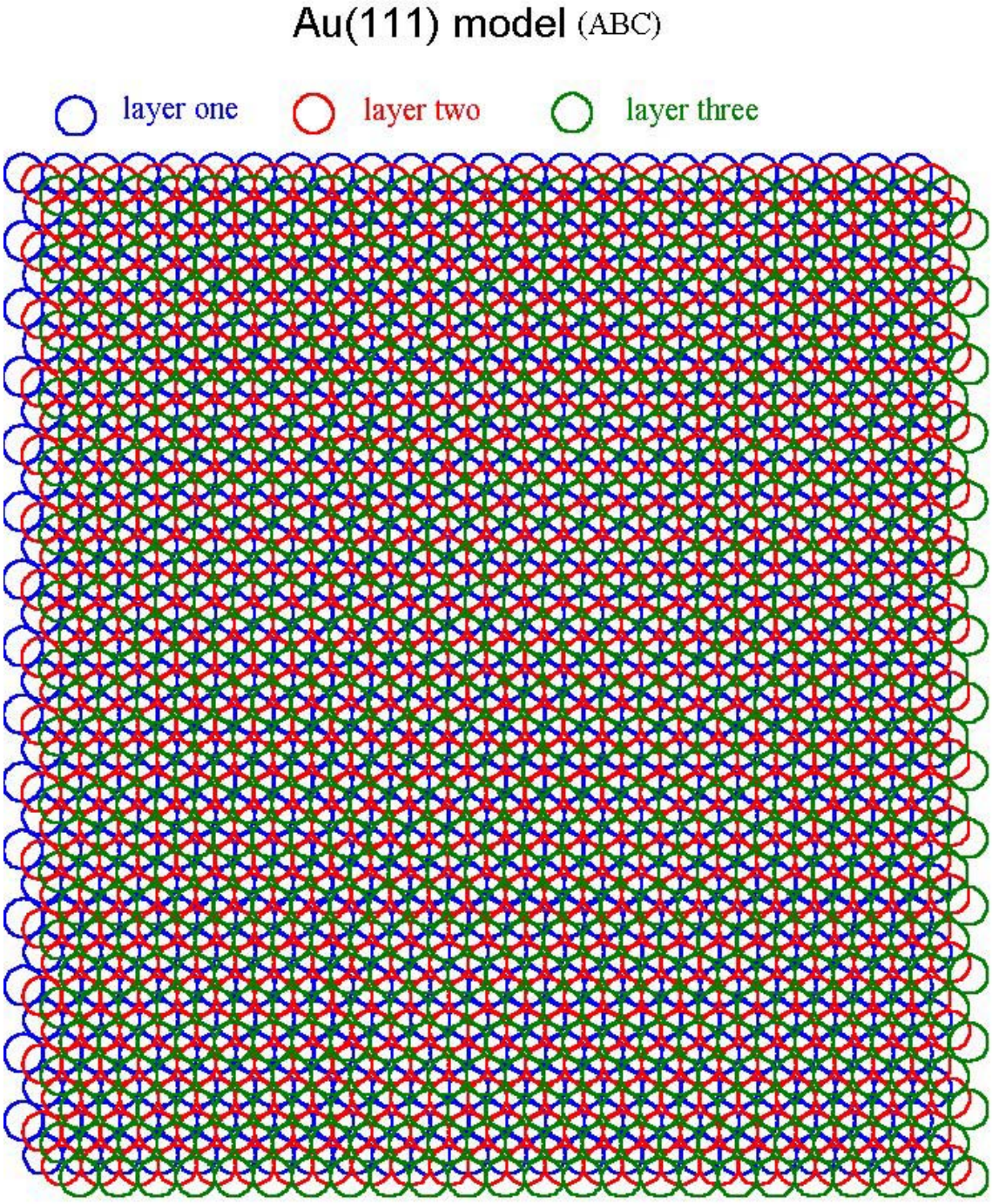


**Figure B.2**: Atomic arrangement of the three top layers of an unreconstructed Au(111)-crystal.

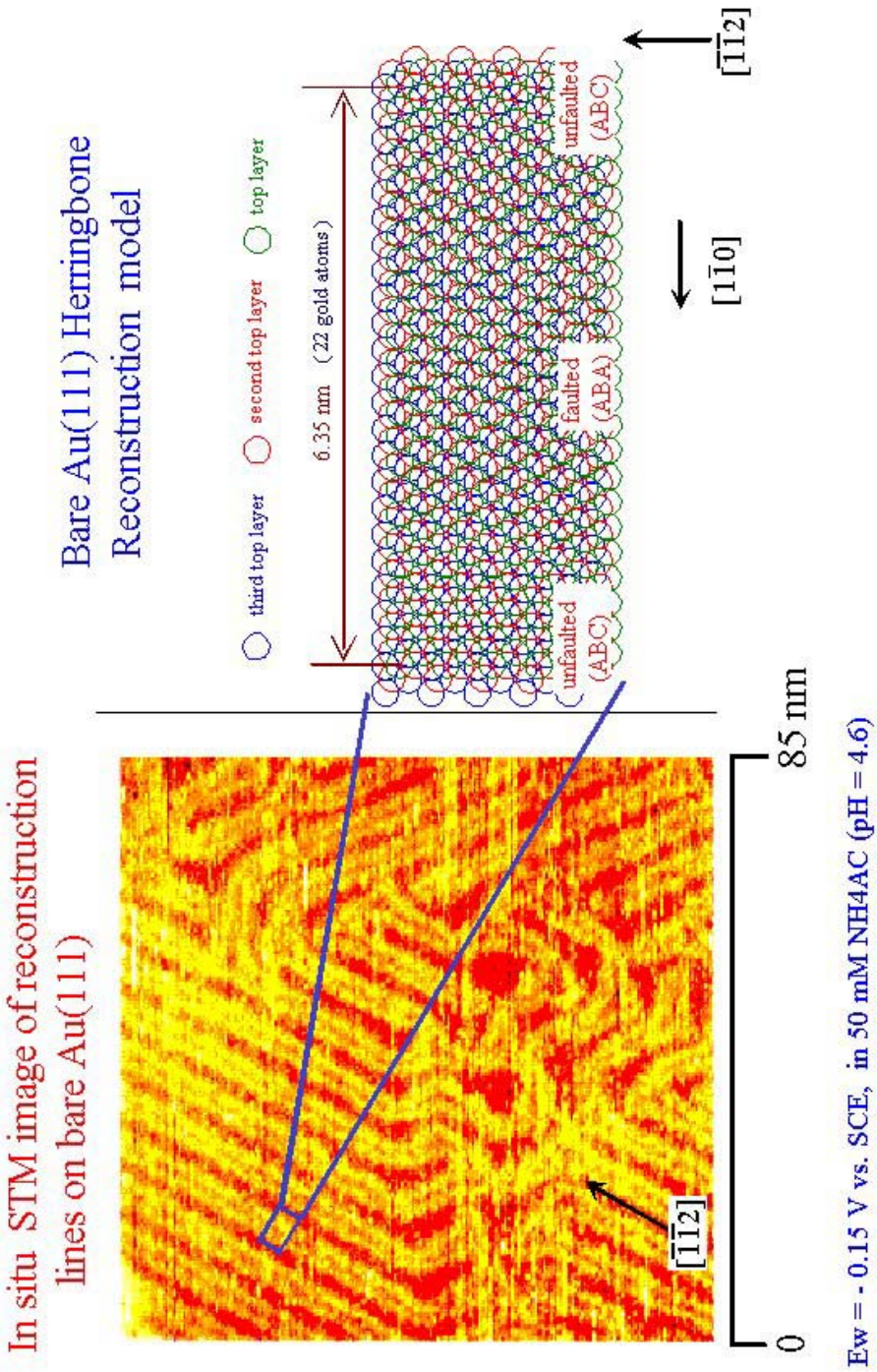


**Figure B.3**: Left) *In situ* STM image of reconstruction lines on Au(111) Right) Model of the atomic arrangement of a reconstructed Au(111)-surface.

# 8 Appendix C: Theoretical notions on Monolayer Differential Pulse Voltammetry

DPV has mainly been used for analytical purposes, i.e. determination of concentration of analytes. A number of papers have dealt with theory of diffusion mode DPV [Aoki,84; Melville,01]. None have, however, treated the special case of monolayer DPV. A simple model with some assumptions is presented in this appendix. The current i(E) in reversible monolayer voltammetry can be expressed as [Hubbard,70]:

$$i(E) = e\sigma l[P]_0 \frac{\exp[F\frac{E(t) - E_0}{RT}]}{\{1 + \exp[F\frac{E(t) - E_0}{RT}]\}^2} \tag{8.1}$$

where e is the electron charge, $\sigma$ is vF/RT, l is the thickness of the adsorbed layer, $[P]_0$ is the concentration of adsorbed species in that layer, v is scan rate, F is Faraday's constant, R is the gas constant, T is the temperature, E(t) is the electrode potential at time t, and $E_0$ is the standard reduction potential of the adsorbed species. We wish to calculate the charge

$$Q = \int_{-\infty}^{\infty} i(t)dt = \frac{1}{v}\int_{-\infty}^{\infty} i(E)dE \tag{8.2}$$

Introducing the substitution

$$x = \exp[F\frac{E - E_0}{RT}]$$

gives

$$dx = \exp[F\frac{E - E_0}{RT}] \cdot \frac{F}{RT} dE$$

and

$$dE = \frac{1}{x} dx \cdot \frac{RT}{F} \tag{8.3}$$

The charge is then given by

$$Q = \frac{1}{v} \cdot e\sigma l[P]_0 \int_0^\infty \frac{x}{(1+x)^2} \cdot \frac{1}{x} dx \cdot \frac{RT}{F} = \frac{RT}{vF} e \frac{vF}{RT} l[P]_0 \int_0^\infty \frac{dx}{(1+x)^2} = el[P]_0 \int_0^\infty \frac{dx}{(1+x)^2} \quad (8.4)$$

$$Q = -el[P]_0 \left[ \frac{1}{1+x} \right]_0^\infty = el[P]_0 \quad (8.5)$$

The potential versus time profile for monolayer Differential Pulse voltammetry is shown below.

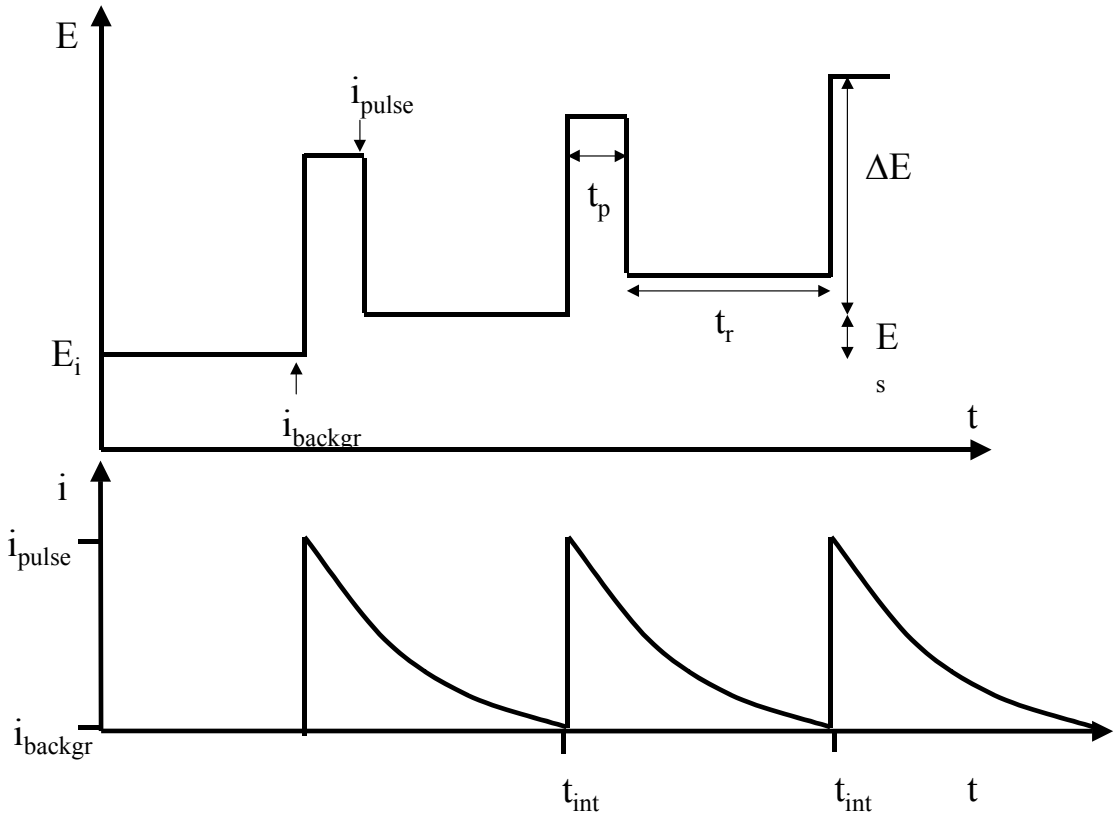


It is assumed that the current at the end of each interval in the E-steps has dropped to zero. We call this current $i_{backgr}$. Then

$$i_{backgr}(t) = f[C_{ox}(t), C_{red}(t)] \rightarrow 0 \quad \text{for} \quad t \rightarrow t_{int}$$

When the pulse is invoked there is no longer equilibrium since $C_{ox}(t)$ and $C_{red}(t)$ remain at the values immediately prior to the pulse. The current after the pulse is

$$i_{pulse} = eC_{red}(t)k_0 \exp\left(\frac{\alpha[E(t)+\Delta E]}{RT}\right) - eC_{ox}(t)k_0 \exp\left(\frac{\beta[E(t)+\Delta E]}{RT}\right) \quad (8.6)$$

where t is the time immediately prior to the pulse, and α and β are the electron transfer coefficients. Further

$$\alpha + \beta = 1 \quad (8.7)$$

Moreover, the ratio of oxidized and reduced species is

$$\frac{C_{ox}(t)}{C_{red}(t)} = \exp\left[F\frac{E(t)-E_0}{RT}\right] \quad (8.8)$$

$$C_{red} = C - C_{ox} = C - C_{red}(t)\exp\left[F\frac{E(t)-E_0}{RT}\right]$$

$$C_{red}(t) = C\frac{1}{1+\exp\left[F\frac{E(t)-E_0}{RT}\right]} \quad (8.9)$$

$$C_{ox}(t) = C\frac{\exp\left[F\frac{E(t)-E_0}{RT}\right]}{1+\exp\left[F\frac{E(t)-E_0}{RT}\right]}$$

The pulse current is then

$$\begin{aligned} i_{pulse} &= eC_{red}(t)k_0 \exp\left[\frac{\alpha E(t)}{RT}\right]\exp\left[\frac{\alpha\Delta E}{RT}\right] - eC_{ox}(t)k_0 \exp\left[\frac{-\beta E(t)}{RT}\right]\exp\left[\frac{-\beta\Delta E}{RT}\right] \\ &= eC_{red}(t)k_0 \exp\left[\frac{\alpha E(t)}{RT}\right]\cdot\left[\exp\left[\frac{\alpha\Delta E}{RT}\right] - \frac{C_{ox}(t)}{C_{red}(t)}\exp\left[\frac{-(\alpha+\beta)E(t)}{RT}\right]\exp\left[\frac{-\beta\Delta E}{RT}\right]\right] \end{aligned} \quad (8.10)$$

From eqs. (8.7)-(8.9) we get

$$i_{pulse} = eCk_0 \frac{\exp\left[\frac{\alpha E(t)}{RT}\right]}{1+\exp\left[F\frac{E(t)-E_0}{RT}\right]}\left[\exp\left[\frac{\alpha\Delta E}{RT}\right]-\exp\left[\frac{-\beta\Delta E}{RT}\right]\right] \tag{8.11}$$

If $\Delta E$ is small then

$$i_{pulse} \approx eCk_0 \frac{\Delta E}{RT}\frac{\exp\left[\frac{\alpha E(t)}{RT}\right]}{1+\exp\left[F\frac{E(t)-E_0}{RT}\right]} \tag{8.12}$$

The integral I under the DPV curve is

$$I = \frac{1}{v}\int eCk_0 \frac{F\Delta E}{RT}\frac{\exp\left[F\frac{\alpha E(t)}{RT}\right]}{1+\exp\left[F\frac{E(t)-E_0}{RT}\right]}dE = eCk_0 \frac{F\Delta E}{RT}\frac{1}{v}\int \frac{\exp\left[F\frac{\alpha E}{RT}\right]}{1+\exp\left[F\frac{E-E_0}{RT}\right]}dE \tag{8.13}$$

Now, C is set to $l[P]_0$, cf. (8.1). From the substitution

$$x = \exp\left[F\frac{E-E_0}{RT}\right]$$

$$dx = \exp\left[F\frac{E-E_0}{RT}\right]\cdot\frac{F}{RT}dE \tag{8.14}$$

$$dE = \frac{1}{x}\frac{RT}{F}dx$$

the integral I is expressed as

$$I = e\cdot l[P]_0\cdot k_o\cdot\frac{F\Delta E}{vRT}\cdot\frac{RT}{F}\int\frac{\exp\left[\frac{\alpha E_0}{RT}\right]\cdot x^{\alpha}}{1+x}\frac{dx}{x} =$$
$$\frac{1}{v}el[P]_0\exp\left[\frac{\alpha E_0}{RT}\right]k_0\Delta E\int_0^{\infty}\frac{1}{x}\frac{x^{\alpha}}{1+x}dx \tag{8.15}$$

$$I = el[P]_0\left(\frac{k_0\Delta E}{v}\right)\int_0^{\infty}\frac{x^{\alpha-1}}{1+x}dx \tag{8.16}$$

For $\alpha$=½ the integral in eq. (8.16) is

$$y = \int_0^\infty \frac{1}{\sqrt{x}} \frac{1}{1+x} dx ;$$

The substitution

$$y = \sqrt{x};$$

$$dy = \frac{1}{2\sqrt{x}} dx = \frac{1}{2y} dx \tag{8.17}$$

$$dx = 2ydy$$

gives

$$I = \int_0^\infty \frac{1}{y} \cdot \frac{1}{1+y^2} 2ydy = 2\int_0^\infty \frac{1}{1+y^2} dy = 2arctg\Big|_0^\infty \tag{8.18}$$

$$I = e \cdot 1 \cdot [P]_0 \left( \frac{k_0 \Delta E}{v} \right) \cdot \pi$$

$$\boxed{I = e \cdot 1 \cdot [P]_0 \left( \frac{k_0 \Delta E}{v} \right) \cdot \pi = Q \cdot \pi \cdot \frac{k_0 \Delta E}{v}} \tag{8.19}$$

To be noted: The maximum of the integral in (8.13) is given by the maximum of

$$\frac{x^\alpha}{1+x}$$

the differential of which is

$$\frac{(1+x)\alpha \cdot x^{\alpha-1} - x^\alpha \cdot 1}{(1+x)^2} = 0$$

$$(1+x) \cdot \alpha \cdot \frac{1}{x} - 1 = 0 \qquad x \neq 0$$

$$\alpha(1+x) - x = 0$$

$$x(\alpha - 1) + \alpha = 0$$

$$x = -\frac{\alpha}{\alpha - 1} = \frac{\alpha}{1-\alpha} \tag{8.20}$$

giving

$$\exp\left[ F \frac{E - E_0}{RT} \right] = \frac{\alpha}{1-\alpha}$$

which means that the peak potential observed in DPV is shifted from the equilibrium potential for $\alpha \neq ½$.

$$E - E_0 = \frac{RT}{F} \ln \frac{\alpha}{1 - \alpha} \tag{8.21}$$

For instance $\alpha = 0.25$ yields

$$E\text{-}E_0 = -28 \text{ mV}$$

# 9 Appendix D: List of publications

## Articles

Andersen JET, Zhang JD, Chi Q, Hansen AG, Nielsen JU, Friis EP, Ulstrup J, Boisen A, Jensenius H, *In situ scanning probe microscopy and new perspectives in analytical chemistry*, Trend. Anal. Chem. 18 (11) (1999) 665-674.

Hansen AG, Mortensen MW, Andersen JET, Ulstrup J, Kühle A, Garnæs J, Boisen A, *Stress Formation During Self-Assembly of Alkanethiols on Differently Pre-Treated Gold Surfaces*, Probe Micros. 2 (2) (2001) 139-149.

Zhang J, Chi Q, Andersen JET, Hansen AG, Nielsen JU, Ulstrup J, *Organization and Control of Nanoscale Structures on Au(111)*, Probe Micros. 2 (2) (2001) 151-167.

Zhang J, Chi Q, Nielsen JU, Hansen AG, Andersen JET, Wackerbarth H, Ulstrup J, *Organized monolayers of biological macromolecules on Au(111) surfaces*, Russ. J. Electrochem. 38 (1) (2002) 68-76.

Zhang J, Chi Q, Kuznetsov AM, Hansen AG, Wackerbarth H, Christensen HEM, Andersen JET, Ulstrup J, *Electronic properties of functional biomolecules at metal/aqueous solution interfaces*, J. Phys. Chem. B 106 (6) (2002) 1131-1152.

Hansen AG, Wackerbarth H, Zhang J, Kuznetsov AM, Ulstrup J, *Nanoscale and single-molecule interfacial electron transfer*, acc. for publ. in Russ. J. Electrochem.

Hansen AG, Boisen A, Nielsen JU, Wackerbarth H, Chorkendorff I, Andersen JET, Zhang J, Ulstrup J, *Adsorption and Interfacial Electron Transfer of Saccharomyces Cerevisiae Yeast Cytochrome c Monolayers on Au(111)-Electrodes*, acc. for publ. in Langmuir.

## Talks at international conferences

Hansen AG, Boisen A, Ulstrup J, *Adsorption of biomolecules on microcantilevers*, Scanning Probe Microscopy, Sensors and Nanostructures, Tokyo, may 2001.

## Poster Presentations

Hansen AG, Andersen JET, Ulstrup J, Boisen A, *Kinetics of the self-assembly of alkanethiols on a gold coated microcantilever*, *In situ* Nanoscale Biochemistry by SPM-Based technologies, København, March 2000.

Hansen AG, Andersen JET, Ulstrup J, Boisen A, *Kinetics of the self-assembly of alkanethiols on a gold coated microcantilever*, Annual Meeting of the Danish Physical Society, Nyborg, June 2000.

Hansen AG, Andersen JET, Ulstrup J, Boisen A, *Kinetics of the self-assembly of alkanethiols on a gold coated microcantilever*, Faraday Discussions (116) on Bioelectrochemistry, Southampton, July 2000. Received Skinner prize for best poster.

Hansen AG, Boisen A, Zhang J, Wackerbarth H, Andersen JET, Ulstrup J, *In Situ STM And Nanoscale Function Of Redox Metalloprotein Monolayers On Single-Crystal Au(111)-Surfaces*, nano-7 and ecoss-21, Malmö, june 2002.

Hansen AG, Boisen A, Zhang J, Wackerbarth H, Andersen JET, Ulstrup J, *In Situ STM And Nanoscale Function Of Redox Metalloprotein Monolayers On Single-Crystal Au(111)-Surfaces*, eurobic-6, Lund/København, july-august 2002.